The Projected Halo Model

by

Anbo Chen

A dissertation submitted in partial fulfillment
of the requirements for the degree of
Doctor of Philosophy
(Physics)
in the University of Michigan
2013

Doctoral Committee:

Professor August E. Evrard, Chair
Professor Robert W. Keener
Professor Timothy A. McKay
Assistant Professor Jeffrey McMahon

You are random.

- Thomas Lam & SeungJin Lee

2013

To my parents and the seven years of my life

ACKNOWLEDGMENTS

My life as a Physics Ph.D. student at the University of Michigan has been an exciting endeavor. In hindsight, much could have been different, without the help and support of my advisor, colleagues, friends, and family.

First of all, I would like to thank my advisor, Gus Evrard, without whom this dissertation would not have been possible. Through these years working with him on research and teaching, I have learned knowledge on galaxy clusters, as well as professionalism in academia. His influence on various aspects shaped me into whom I am now, for which I am deeply grateful.

To me, Tim McKay is both extremely intelligent and humorous, attributes that rarely exist on the same person. I thank him for his guidance and comments to this dissertation. I would also like to thank Jeff McMahon for his insights which made this process of obtaining my degree much easier, and also Bob Keener, for providing help when it was desperately needed.

Outside of my committee, I enjoyed the numerous discussions on a wide range of topics with Greg Tarlè, whom I view as a dear friend, besides a professor. Dragan Huterer gave me my best class in Michigan. I also had a wonderful experience working as his grader. I am fortunate to sit in an office close to Fred Adams, who is a brilliant astrophysicist and an interesting person beyond that. I had the fortune to work with Dave Gerdes, who is one of the best lecturers in my opinion, when I first arrived in Michigan. I deeply appreciate his recognition of my teaching and intellectual abilities. I have also had the fortune to

work with Dan Amidei, Chris Miller, Jon Miller, Shannon Murphy, and Brenda Gunderson in teaching various classes. I would like to sincerely thank them for making me a better instructor through these years.

Nothing would have been possible without the help and support from my colleagues. I am lucky to have Brandon Erickson in my research group, who has helped me extensively in writing this dissertation. I very much admire his pursue of excellency in every aspect of life, which I have learned through our numerous interesting conversations. Carlos Cunha is the person I turn to whenever an honest opinion is needed. He has shared with me from his knowledge in Markov Chain Monte Carlo, to piano, football, and life in Brazil. Hao Jiangang[1] is a precious friend of mine, who has provided me guidance towards my degree, besides his knowledge on optical galaxy clusters. I must also thank Tomasz Biesiadzinski, for his generous help on this dissertation, as well as the conversations with latte. This work may remain unfinished by now without my amazing friend, Brian Nord, whose passion always inspires me. I was fortunate to have shared the office with Lynn Endicott during my first year in Michigan, who has taught me English and the American life. In addition, I would like to thank Ryo Saotome, Li Xuefei, Liu Hao, Zhang Bo, Shen Chao, Navid Dianati, Adam Becker, Devin Harper, Jake Ketchum, Eva Proszkow, Zhang Lei, and many others in the Physics department for the love and support over the years.

My life as a graduate student was made much easier, by my friends Chrissy Zigulis, Chris Bolang, Judy McDonald, and formerly Kimberly Smith, Elizabeth Branch in the student service office. I deeply appreciate them for accommodating my personal situations and making this process so smooth. The computational part of my research would not have been possible without the support of our Linux expert, Marlin Whitaker, and Tim Rolston.

Furthermore, I would like to thank Thomas Lam and SeungJin Lee for food, bragging and Go and also Michael Zhang, Wang Yizao, Yang Zifan, Troy Zhao, John Starkweather and Michael Anuzis in the University of Michigan Go Club. I also appreciate the sup-

[1] Chinese and Japanese names will appear in the correct order in this segment.

port from everyone in the Japanese department, especially Watarai Shoko, for helping me achieve the current level of proficiency, and Oka Mayumi, for training me to win the 2013 Michigan Japanese Speech Contest. I must also thank Lynelle James for introducing me the music of Brahms, and JInHwa Lee, for assisting me to excel in the Chopin valse.

Lawrence Austen has been a mentor to my career besides an excellent boss, for which I am forever thankful. I am also deeply grateful to Michael Pettis, for his faith in my capabilities and his help in my most desperate time. I sincerely appreciate the various assistances from Wang Jian, Ma Xiaotao, Wang Chenyu, Li Wei, Wu Xiaomu, Luo Jieying, Hou Yang, and others during my job-hunt, without any of whom my future will be uncertain. And I would like to thank all those friends who supported me during my hardest time, especially Qi Dalv and Wang Yunjia, and my friends in East Lansing when I first arrived, particularly Wang Jianling and Ni Haicong.

Lastly, I would like to thank my uncle, Peter Chen, for his guidance on my life; my aunt Jia Chaoying and uncle Peter Ma, for their hospitality and hints to navigate in academia; my ex-girlfriend Zhang Liyun, who has the greatest influence on me, for walking with me through the difficult time in a foreign country, and my girlfriend Hong, for making my final time in Ann Arbor so sweat.

And finally, to my father and mother, whose unconditional love and support are the only reasons I move forward without worries in my life, thank you.

TABLE OF CONTENTS

LIST OF FIGURES

LIST OF TABLES

LIST OF APPENDICES

LIST OF ABBREVIATIONS

AGN Active Galactic Nuclei

BAO Baryonic Acoustic Oscillation

BCG Brightest Central Galaxy

COBE Cosmic Background Explorer

CDM Cold Dark Matter

CMB Cosmic Microwave Background

CPU Central Processing Unit

DES Dark Energy Survey

ESO European Southern Observatory

FOF Friends-of-friends

HOD Halo Occupation Distribution

ICM Intra-Cluster Medium

ΛCDM Λ Cold Dark Matter

MaxBCG Maximum likelihood Brightest Central Galaxy

MCMC Markov Chain Monte Carlo

NFW Navarro-Frenk-White

PCA Principal Component Analysis

PDF Probability Density Function

SDSS Sloan Digital Sky Survey

SDSS-DR7 Sloan Digital Sky Survey 7th Data Release

SO Spherical Overdensity

SPT South Pole Telescope

SZ Sunyaev-Zel'dovich

VISTA Visible and Infrared Survey Telescope for Astronomy

WMAP Wilkinson Microwave Anisotropy Probe

WMAP7 Wilkinson Microwave Anisotropy Probe 7-Year Results

XMM-Newton X-ray Multi-Mirror Mission

XCS XMM Cluster Survey

Bg-sub Background Subtracted

HP Heavily Projected

ABSTRACT

The Projected Halo Model

by

Anbo Chen

Chair: August E. Evrard

I present a semi-analytical halo model to study line-of-sight projection effects in the galaxy cluster population. The model produces realizations of sight-lines using halo space densities and two-halo correlations, and employs a log-normal covariance model to relate halo mass to multivariate observables. The model sums idealized red-sequence galaxy counts (optical richness), thermal Sunyaev-Zel'dovich (SZ) effect, and X-ray flux within an angular annulus set by a given target halo of size R_{200} at redshift z_t after convolution with top-hat, matched, and background-subtracted filters.

The observed signal bias, variance, and covariance for a fiducial target of mass $5\times10^{14}h^{-1}M_\odot$ at $z_t = 0.3$ in a WMAP7 cosmology have been measured. Optical richness is most susceptible to projection, with a top-hat filtered signal bias of 16%, compared to 6% and 4% in SZ and X-ray, respectively, for the fiducial target. Projection in the optical is also more localized in redshift and therefore more dependent on nearby, correlated haloes. Background subtraction removes the bias but increases the variance in observed signals. I examine the sensitivity of these effects to target mass and redshift, finding at $z_t = 0.3$ that the top-hat projected SZ signal bias exceeds that in the optical at halo masses below $\sim10^{13.9}h^{-1}M_\odot$. The underlying mass distribution at fixed observed signal is shown to be non-Gaussian with its scatter increased by projection and a skewed towards lower mass.

Covariance in observed signals is studied via extending the model to include intrinsic correlations. The projected contributions are found to be positively correlated, whose approximate scatter of 7% mostly come from cosmic variance, uncertainties in the spatial distributions of projected haloes. A -20% intrinsic correlation between the optical and SZ / X-ray signals will be reduced to -3% and -10%, respectively, when observed, due to projections for the fiducial target. The degree of such distortions to the intrinsic correlations are

reduced at $z_t = 0.7$ as fractional projection amplitude decreases.

An attempt to model the velocity dispersion in optical galaxy clusters using the projected halo model is made, which involves modeling the Halo Occupation Distribution (HOD) and colors of the galaxy population via Markov Chain Monte Carlo (MCMC). The correlated contribution to velocity dispersion measurements is found to be less than 5%.

In general, line-of-sight projections introduce bias to observed signals of galaxy clusters at the $\sim 10\%$ level, while the precise value is model-dependent. The projected halo model provides a platform, via which projection-induced statistical biases in both signals and signal covariance of galaxy clusters can be assessed, in an era where precision in cluster cosmology reaches $\sim 1\%$.

CHAPTER 1

Introduction

In 1929, Edwin Hubble discovered that galaxies beyond the Milky Way are receding at speeds proportional to their distances [Hubble, 1929],

$$v = Hr, \tag{1.1}$$

in which v is the radial velocity, r is the distance, and H is the Hubble constant. The isotropic recession of distant galaxies points to one rational conclusion, the expansion of the Universe.

In less than a decade, Zwicky [1937] showed that the velocity dispersion in the Coma Cluster cannot be explained using even the most extreme mass-to-light ratio possible in galaxy clusters. This discovery led to the concept of Dark Matter, massive particles that do not exhibit electromagnetic interactions.

Following the accidental discovery of the Cosmic Microwave Background (CMB) by Penzias and Wilson [1965], cosmologists began to favor the Big Bang theory, which describes the Universe as starting from a hot dense state that expanded over cosmic time. However, whether the Universe will eventually contract and collapse due to gravity remained a controversy until the discovery of the accelerating expansion of the Universe around the Millennium. The initial observational evidence was seen in Type-Ia supernovae in distant galaxies [Perlmutter et al., 1999, Riess et al., 1998], followed by subsequent confirmations from studies of the CMB [Spergel et al., 2003] and the Baryonic Acoustic

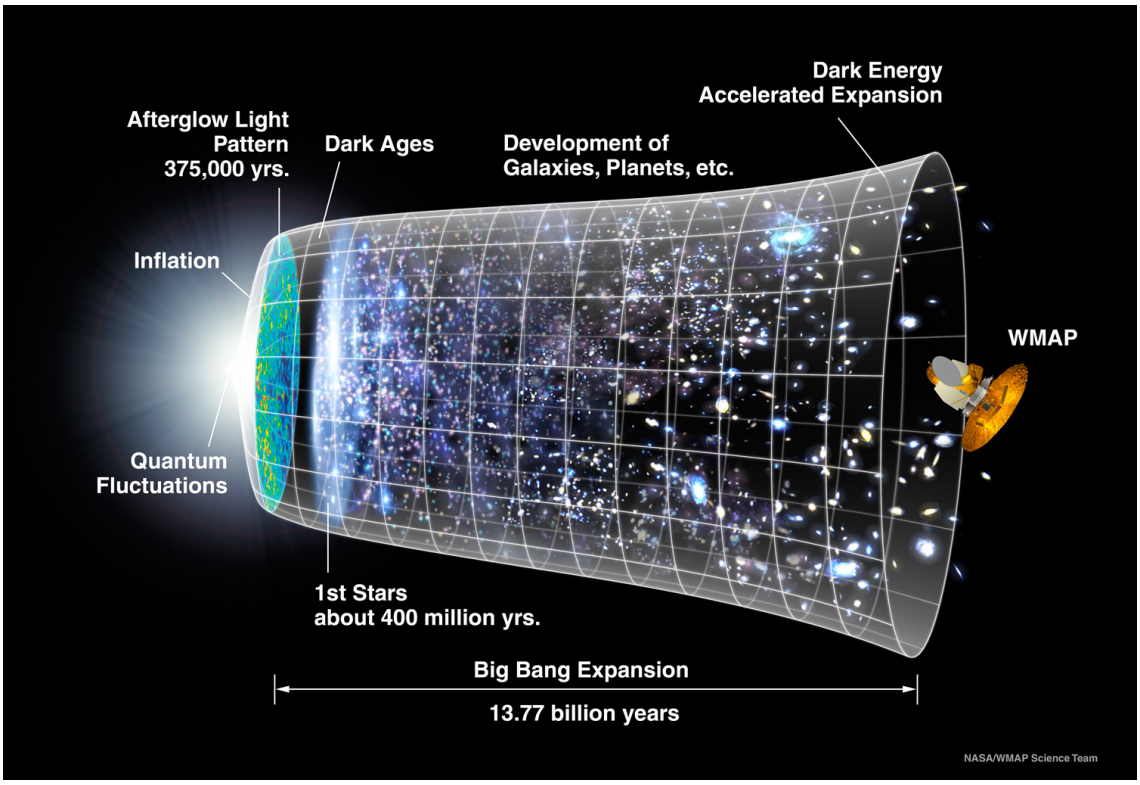

Figure 1.1: An illustrative history of the Universe from the Big Bang, Inflation, to Nucleosynthesis, star formations, and the accelerated expansion. This figure is taken from the NASA website.

Oscillation (BAO) [Eisenstein et al., 2005]. The acceleration pointed to the existence of vacuum energy, a possible form of Dark Energy, thus completing the main ingredients of the modern Λ Cold Dark Matter (ΛCDM) cosmology.

Figure 1, made by NASA, provides an excellent illustration of the time-line of our Universe. From the initial Big Bang, photons were coupled with matter until arriving at the "surface of last scattering", at which point they decoupled and formed the CMB. In the mean time, quarks began to form baryons and subsequently hydrogen, deuterium, helium, and lithium, in the process of Nucleosynthesis. These light elements later formed the first generation of stars and galaxies.

1.1 The ΛCDM Cosmology

In the modern ΛCDM cosmology, Hubble's Law in Eq. 1.1 can be re-written as

$$H \equiv \frac{\dot{a}}{a}, \tag{1.2}$$

in which $a(t)$ is the scale factor of the Universe, which is defined to be 1 at the present time and 0 at the beginning of space-time. The dimensionless Hubble parameter, h, is often used, which is defined as $H_0 = 100h\,\mathrm{km\,s^{-1}\,Mpc^{-1}}$, where H_0 is the Hubble constant at present time ($a = 1$).

The Friedmann Equation describes the expansion as

$$H^2 = \frac{8\pi G}{3}\rho - \frac{kc^2}{a^2}, \tag{1.3}$$

in which G is the gravitational constant, k is the spatial curvature, and c is the speed of light. The Wilkinson Microwave Anisotropy Probe (WMAP) experiment results supported a spatially flat universe, i.e., $k = 0$, which then leads to the definition of the critical density,

$$\rho_c = \frac{3H^2}{8\pi G}. \tag{1.4}$$

It is common to use the dimensionless density parameters, Ω, defined as

$$\Omega = \frac{\rho}{\rho_c} = \Omega_r + \Omega_m + \Omega_\Lambda, \tag{1.5}$$

in which Ω_r, Ω_m, and Ω_Λ are the radiation, matter, and vacuum energy contributions. The matter composition can be further broken into its baryonic and Cold Dark Matter (CDM) components,

$$\Omega_m = \Omega_b + \Omega_{\mathrm{CDM}}, \tag{1.6}$$

In a spatially flat universe, $\Omega = 1$, however, its relative composition is not constant. In

fact, the Friedmann equation can also be written as

$$\frac{H^2}{H_0^2} = \Omega_r a^{-4} + \Omega_m a^{-3} + \Omega_\Lambda. \tag{1.7}$$

From the different scalings with expansion parameter in Eq. 1.7, it can be easily seen that our Universe went from being radiation dominated (when $a \to 0$), to matter dominated, and then the present Dark Energy dominated era.

To relate to observations, it is often convenient to use redshift z, as opposed to the scale factor, a. Although initially interpreted as the Doppler shift in wavelength / frequency, redshift can be formally introduced via

$$z = \frac{1}{a} - 1 \tag{1.8}$$

in the scope of the ΛCDM cosmology.

Values of these cosmological parameters derived from the Wilkinson Microwave Anisotropy Probe 7-Year Results (WMAP7) are $h = 0.71$, $\Omega_b = 0.0449$, $\Omega_{\rm CDM} = 0.222$, $\Omega_\Lambda = 0.733$, and $\sigma_8 = 0.801$[1].

1.2 CMB and the Primordial Power Spectra

The CMB is an almost uniform full sky black body radiation with a temperature $\sim 2.7\,\mathrm{K}$, thus peaking in the microwave range of radio frequency. It is the oldest remnant of the initial Big Bang, whose tiny fluctuation $\sim \pm 200\,\mu\mathrm{K}$ beyond absolute homogeneity marks the early quantum fluctuations, which later evolved gravitationally to form stars, galaxies, and large scale structures in our Universe. Figure 1.2 shows this temperature fluctuation on the full sky obtained by the WMAP, a spacecraft launched in 2001 to measure the CMB, succeeding the Cosmic Background Explorer (COBE) mission.

[1] In this dissertation, I shall use the WMAP7 values except in Appendix A when comparing to the Hubble Volume simulation. The definition of σ_8 will come later after Eq. 1.12 in §1.2.

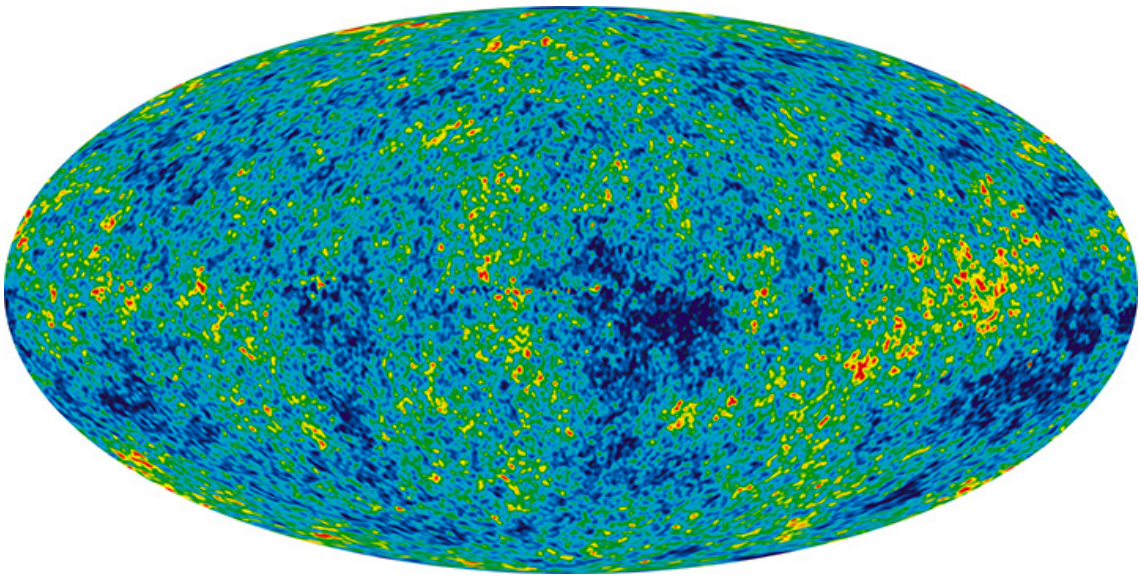

Figure 1.2: The detailed, all-sky picture of the infant Universe created from nine years of WMAP data. The image reveals 13.77 billion year old temperature fluctuations at the level of $\pm 200\mu$K, which correspond to seeds that later grew into galaxies. Signals from the Milky Way were removed using the multi-frequency data. This figure is made by the NASA / WMAP Science Team.

The observation of a homogeneous and isotropic CMB poses a conundrum to the Big Bang cosmology, how did different parts of the Universe establish causal relationship so as to appear homogeneous and isotropic? This problem was reconciled by the theory of inflation [Guth, 1981], which adds a period of rapid expansion following the Big Bang. In the inflationary cosmology paradigm, the inhomogeneity we see in the CMB is the relic of the initial quantum fluctuations "frozen" as photons decoupled from matter.

If we use $\delta(\boldsymbol{r})$ to describe the density perturbation and use δ_k to denote its Fourier transform

$$\delta(\boldsymbol{r}) \equiv \frac{\rho(\boldsymbol{r})}{\bar{\rho}} - 1 = \int \mathrm{d}k\, \delta_k\, e^{i\boldsymbol{k}\cdot\boldsymbol{r}}, \tag{1.9}$$

the power spectrum $P(k)$ can be introduced via

$$< \delta_k \delta_{k'} >= \frac{2\pi^2}{k^3} \delta_D(k - k') P(k), \tag{1.10}$$

in which δ_D is the Dirac delta function. The Fourier transform of the power spectrum is the

two-point correlation function,

$$\xi(r) = \int \frac{\mathrm{d}^3\boldsymbol{k}}{(2\pi)^3} P(k) \exp(i\boldsymbol{k}\cdot\boldsymbol{r}). \tag{1.11}$$

The initial perturbations due to Inflation are expected to be Gaussian [Bardeen et al., 1983, Guth and Pi, 1982, Hawking, 1982, Starobinsky, 1982], such that higher order correlations / powers (bispectrum, trispectrum, *etc.*) are zero.

The variance of the linearly evolved fluctuations at scale R

$$\sigma^2(R) = \int \frac{k^3 P(k)}{2\pi} |\, W(kR) \,|\, \mathrm{d}\ln k, \tag{1.12}$$

in which the window function $W(kR)$ takes the Fourier form of $[3/(kR)^3](\sin kR - kR\cos kR)$ when it has a top-hat shape in real space. The quantity in Eq. 1.12 calculated at $R = 8\,h^{-1}$Mpc and $z = 0$, σ_8, is often used as the normalization parameter of the matter power spectrum.

The evolution of large scale structure is governed by the continuity and Euler equations,

$$\frac{\partial\delta}{\partial t} + \frac{1}{a}\boldsymbol{\nabla}\cdot(1+\delta)\boldsymbol{u} = 0\,, \tag{1.13}$$

$$\frac{\partial\boldsymbol{u}}{\partial t} + H\boldsymbol{u} + \frac{1}{a}[(\boldsymbol{u}\cdot\boldsymbol{\nabla})\boldsymbol{u} + \nabla\phi] = 0\,, \tag{1.14}$$

in which $\boldsymbol{u}$ is the peculiar velocity and the potential ϕ relates to the density perturbations via the Poisson equation:

$$\nabla^2\phi = 4\pi G\bar{\rho}\, a^2\delta. \tag{1.15}$$

In the linear regime ($\delta << 1$), the two equations may be combined to yield [Peebles and Yu, 1970]

$$\frac{\partial^2\delta}{\partial t^2} + 2H\frac{\partial\delta}{\partial t} - 4\pi G\bar{\rho}\delta = 0. \tag{1.16}$$

The growing mode solution to Eq. 1.16 takes the form

$$\delta(k, a) = G(a)\delta(k, 1), \tag{1.17}$$

in which the growth function

$$G(a) \propto \frac{H(a)}{H_0} \int_{z(a)}^{\infty} \mathrm{d}z'(1+z') \left[\frac{H_0}{H(z')}\right]^3. \tag{1.18}$$

In linear perturbation theory, the initial density fluctuation field power spectrum can be written as [Cooray and Sheth, 2002]

$$\frac{k^3}{2\pi^2} P^{\mathrm{lin}}(k) = \delta_H^2 \left(\frac{k}{H_0}\right)^{n+3} T^2(k), \tag{1.19}$$

in which $n \sim 1$ [Harrison, 1970, Peebles and Yu, 1970, Zeldovich, 1972] is the slope of the scale-invariant initial spectrum; and $T^2(k)$ is the transfer function that marks the deviation from the initial scale-free form.

Causes of departures from the primordial power spectrum include the transition from the radiation-dominated era to the matter-dominated era. Differences in growth rate of density perturbations during the two epochs create a turnover in the shape of the power spectrum [Blumenthal et al., 1984, Bond and Efstathiou, 1984]. In addition, baryons, massive neutrinos, *etc.* leave other important features in the transfer function. In this dissertation, I adopt the fitting form of $T^2(k)$ in Eq .1.19 provided by Eisenstein and Hu [1999].

1.3 Dark Matter Haloes and N-body Simulations

The linear and higher order perturbation theory can only describe gravitational clustering when $\delta << 1$. As the density fluctuation approaches unity, we enter the non-linear regime, in which the formation and clustering of non-linear objects have been studied via N-body

simulations.

In the spherical collapse model, dark matter haloes form from the collapse of a region with initial overdensity

$$\frac{\delta_{\rm sc}(z)}{1+z} = \frac{3}{5}\left(\frac{3\pi}{2}\right)^{2/3} \approx 1.6865. \tag{1.20}$$

Linear theory predicts that the virialized halo should have a density $\Delta_{\rm vir} = 18\pi^2 \approx 178$ times the background density, which leads to the definition of halo mass

$$M_{200c} = 200 \times \frac{4}{3}\pi {\rm R}_{200}{}^3 \rho_c \tag{1.21}$$

defined as the mass enclosed by radius $\rm R_{200}$, at which the average density enclosed is 200 times the critical density. In some literatures, the other convention, M_{200m} defined as $\Delta = 200$ times the background matter density, may be used.

In this dissertation, I shall adopt the $M_{200} \equiv M_{200c}$ convention in Eq. 1.21. For details on conversions between M_{200c} and M_{200m}, refer to Appendix D.

To study the formation and clustering of matter haloes, N-body simulations employing collision-less dark matter particles have been run, [*e.g.*, Evrard et al., 2002, Sheth and Tormen, 1999, Warren et al., 2006]. Figure 1.3 shows the $z = 0$ output in the Millennium Simulation by the Virgo Consortium [Springel et al., 2005]. It was the largest N-body simulation of its time, using 10 billion particles and taking almost one month to complete on a 512-processor cluster at the Max Planck Institute for Astrophysics in Garching, Germany. In the figure, one can see visualizations of dark matter haloes at the scale of $\sim$ Mpc.

In N-body simulations, haloes are found via Spherical Overdensity (SO) or Friends-of-friends (FOF) algorithms. Their population density in the co-moving space, $n(M, z)$, is commonly referred to as the mass function, which can be formulated by

$$f(\sigma, z) \equiv \frac{M}{\overline{\rho}_m}\frac{{\rm d}n(M,z)}{{\rm d}\ln\sigma^{-1}} \tag{1.22}$$

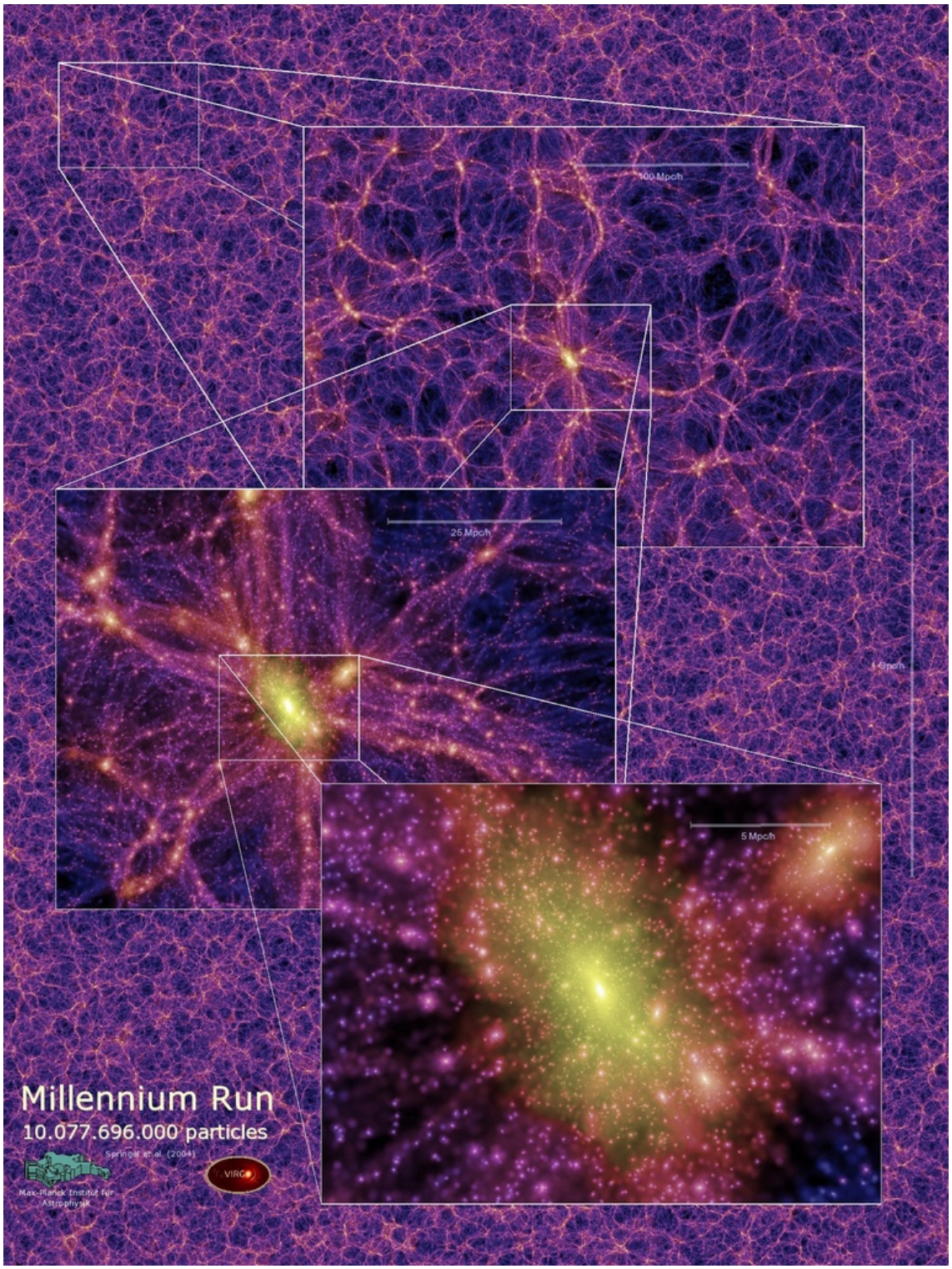

Figure 1.3: A snapshot of the $z = 0$ output in the Millennium Simulation, taken from The Virgo Consortium website.

in which σ is defined in Equation 1.12, and $f(\sigma, z)$ is a model dependent function of the filtered perturbation spectrum. Such a formalism using $\sigma^{-1}(M)$ as oppose to M as the variable was initially proposed by Press and Schechter [1974]. It was later confirmed by Jenkins et al. [2001] that when expressed as a function of σ^{-1}, $f(\sigma)$ has the same universal curve independent of the output time in simulations (the redshift dependency is added for more accurate fit to the mass function).

Various simulations have produced empirical fitting forms of $f(\sigma, z)$ [Evrard et al., 2002, Jenkins et al., 2001, Tinker et al., 2008]. In this work, I shall in use the result by Tinker et al. [2008] in most places, except for Appendix A, where I use the Evrard et al. [2002] mass function in consistency with the Hubble Volume simulation.

1.4 Observations of Galaxy Clusters

Much of our knowledge about the Universe and the ΛCDM cosmology comes from studying the CMB, Supernovae, BAO, and galaxy clusters. These different studies complement each other via untangling degeneracies in various cosmological parameters, as seen in Fig. 1.4, where values of Ω_m and Ω_Λ are constrained using results from the CMB, Supernovae, and galaxy clusters.

Clusters of galaxies were first observed as local enhancements in galaxy number [Abell, 1958, Zwicky et al., 1961] in the optical wavelength, then as extended sources of X-ray emission from the hot intra-cluster plasma [Forman et al., 1972], and as extended regions where the CMB spectrum has been distorted due to the inverse Compton scattering from thermal electrons in the plasma [Sunyaev and Zeldovich, 1972]. In addition, the curvature in space-time created by halo mass bends the light from distant galaxies, which may result in weakly or strongly lensed images. Projected mass distribution between the source and us can be reconstructed from the lensed images [*e.g.*, Leauthaud et al., 2007].

An illustration combining these different observations / measurements can be seen in

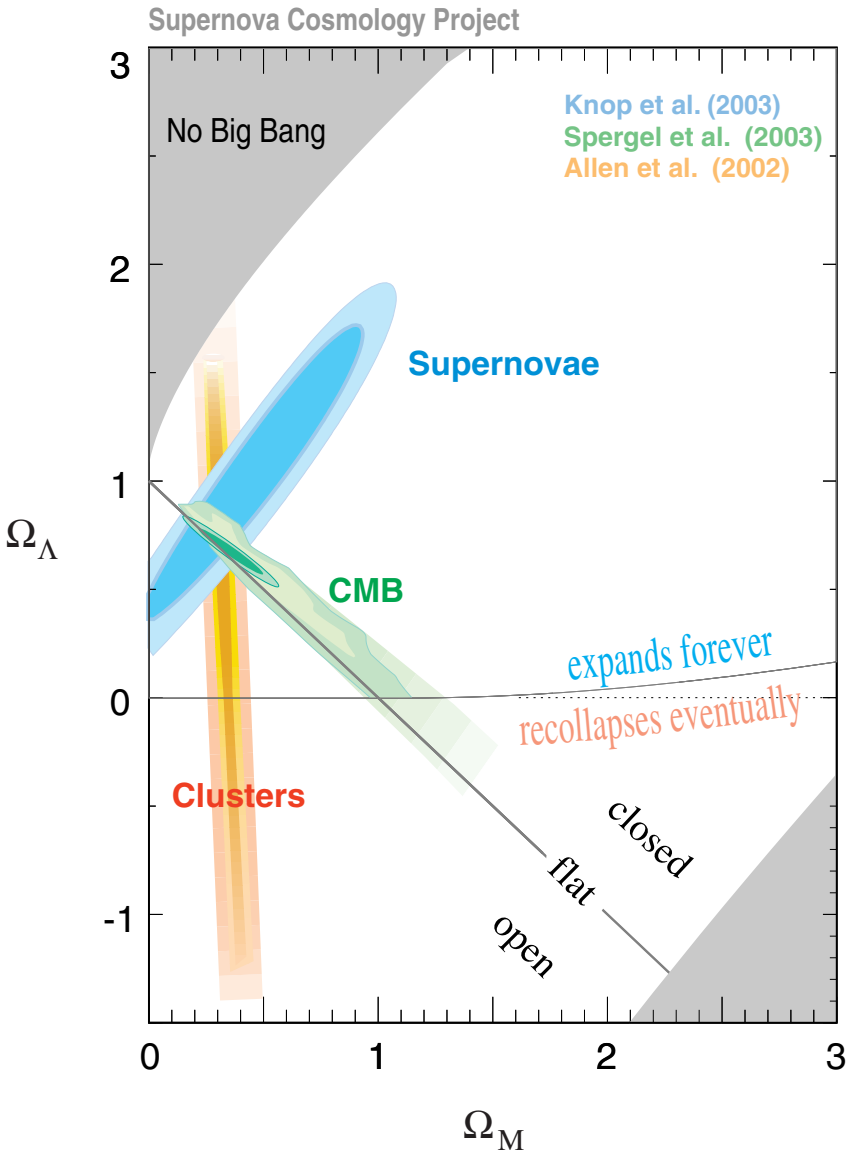

Figure 1.4: An illustration of constraining Ω_m and Ω_Λ through the results of CMB, Supernovae, and galaxy clusters. This figure is made by the Supernovae Cosmology Project.

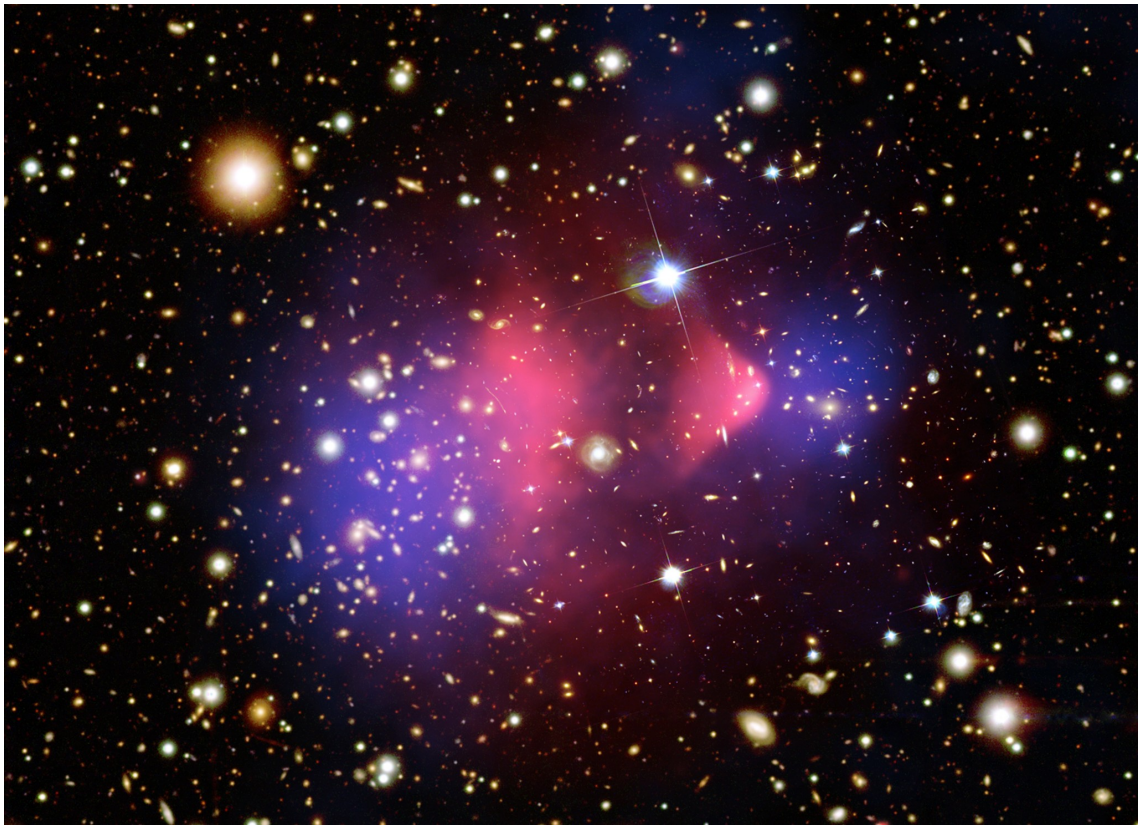

Figure 1.5: Galaxy cluster 1E 0657-56, commonly known as the "bullet cluster", is shown in this composite image. Its individual galaxies are seen in the optical image data. Overlaying on top of the optical image in red color is the X-ray emission, which shows traces of the hot intra-cluster medium gas. The dark matter halo mass is mapped by gravitational lensing of the background galaxies and is shown in blue color. One can easily see the the shock front in shape of the gas cloud created by the collision between the two clusters. This clear separation of dark matter and gas clouds is considered to be direct evidence to the existence of dark matter. This composite figure is taken from the NASA website.

the composite image (Figure 1.5) of galaxy cluster 1E 0657-67, more commonly known as the "bullet cluster". The figure overlays the X-ray emission as well as the lensing mass on top of the optical image of galaxies. The "bullet cluster" is a merging two-cluster system, as one can see from the inferred lensing mass in blue color which shows the positions of the two dark matter haloes. The striking feature of this observation is that one can easily see from the X-ray emission, shown in red color, that the gas clouds have been stripped away from the centers of the two haloes post collision. This separation of dark matter and gas clouds is considered direct evidence to the existence of dark matter.

1.4.1 Optical Galaxy Clusters

The matter composition of the Universe includes CDM and baryonic gas. Their distributions are not the same due to thermal pressure, radiative processes, *etc.* in the latter substance. White and Rees [1978] showed that the baryonic gas can cool and form stars in the potential well of a virialized halo. Thus in this framework, galaxies exist in the centres of haloes or sub-haloes, the latter of which are local sub-clumps in dark matter haloes. These two populations are commonly referred to as central and satellite galaxies. In the dark matter halo framework, the luminosity and spatial distribution of galaxies are characterized by the Halo Occupation Distribution (HOD).

The process of galaxy formation involves radiative cooling, hydrodynamic and magnetohydrodynamic processes, feedback from Active Galactic Nuclei (AGN), and the evolution of the comic web in the background. Its complexity and non-linear nature confine the study to primarily numerical simulations.

During the halo formation process, baryonic matter is thermalized by the release of gravitational potential energy via shocks. The thermal pressure supports intra-cluster plasma against gravitational collapse until the gas is sufficiently cooled. In fact, feedback from compact sources such as AGN limit the cooling process very effectively, reducing the amount of gas in galaxies relative to the Intra-Cluster Medium (ICM) [Allen et al., 2008, Giodini et al., 2009, Lin and Mohr, 2004].

In optical surveys, it is common to focus on red-sequence galaxies, ones that lie on the redder end of the color-magnitude diagram. Morphologically speaking, the red-sequence galaxies are usually elliptical [Coleman et al., 1980], which tend to have relatively low star formation rates. In addition to red-sequence galaxies are blue galaxies, ones that lie near the bluer end of the color-magnitude diagram. Blue galaxies are often spiral and have a higher star formation rate, as reflected in their color. The minority of galaxies residing in between these two groups on the color-magnitude diagram form the “green valley”.

In Chapter 5 of this dissertation, I shall fit an empirical HOD model to the Sloan Digital

Sky Survey (SDSS) optical galaxies and subsequently model the color evolution of the red and blue populations separately.

1.4.2 SZ and X-ray

A majority of the baryonic matter in clusters lives in the form of hot gas in the ICM. Gravitational heating can push up the ICM gas temperature to around $10^7 \sim 10^8$ K, thus making it emit brightly in the X-ray wavelength. The primary mechanisms in the X-ray emissions of clusters include free-free (Bremsstrahlung), free-bound, and bound-bound emissions. The bolometric X-ray luminosity of a cluster is given by

$$L_{\rm X} = \int {\rm d}^3\boldsymbol{r}\rho^2_{gas}(\boldsymbol{r})\Lambda(T(\boldsymbol{r})), \tag{1.23}$$

in which ρ_{gas} is the thermal gas density and $\Lambda(T(\boldsymbol{r}))$ is a normalized emissivity dependent only on temperature [Arnaud and Evrard, 1999].

Besides X-ray observations, inverse Compton scattering of CMB photons by electrons in the ICM plasma creates distortions in the CMB map at small scales, known as the thermal SZ effect. Observation of SZ clusters are usually characterized by the integrated flux $Y_{\rm SZ}$, which is proportional the integrated electron density along the line-of-sight,

$$Y_{\rm SZ} = \frac{k_B\sigma_T}{m_e c^2}\int {\rm d}^3\boldsymbol{r}\, n_e(\boldsymbol{r})\, T_e(\boldsymbol{r}), \tag{1.24}$$

in which k_B is the Boltzmann constant, σ_T denotes the Thomson cross section, m_e, n_e, and T_e are the mass, number density, and temperature of electron, respectively [da Silva et al., 2000, Sunyaev and Zeldovich, 1972].

A model of cluster populations observed in optical, SZ, and X-ray wavelengths forms the primary object of interest in this dissertation.

1.5 Motivations of the Projected Halo Model

The extended nature of clusters makes them susceptible to contamination from sources projected along the line-of-sight. By themselves, the massive haloes that host clusters are partially responsible for projected contamination, as the virial regions of haloes above $10^{14}h^{-1}\mathrm{M}_{\odot}$ cover $\sim 10\%$ of the sky [Voit et al., 2001].

Early N-body simulations were used to study the degree to which optical studies of clusters based on single-band photometry were subject to projected confusion. Frenk et al. [1990] and van Haarlem et al. [1997] showed that large errors in membership and inferred velocity dispersion result when clusters are defined as local overdensities in single-band photometry, as in the original prescription of Abell [1958]. Such errors are dramatically reduced when cluster finding is performed using spectroscopic redshifts for member galaxies [Biviano et al., 2006, Eke et al., 2004, Padilla and Lambas, 2003, Wojtak et al., 2007, Yan et al., 2004]. Multi-band photometric surveys enable cluster finding via methods that rely on red-sequence galaxies with evolved stellar populations [*e.g.*, Gladders and Yee, 2005, Koester et al., 2007a] or on redshifts derived from photometry [Adami et al., 2010, Eisenhardt et al., 2008, Wilson et al., 2009]. Preliminary tests of these methods with cosmological simulations [*e.g.*, Adami et al., 2010, Cohn et al., 2007, Johnston et al., 2007] have produced estimates of the blending and mis-centering that occurs when haloes lie near enough in sky - color or sky - photo-z space.

Since the thermal SZ effect is largely redshift independent, the SZ signal from a given sky location will contain contributions from the electron pressure of all haloes along the line-of-sight [Bartlett and Silk, 1994]. Simulated sky maps based on explicit gas dynamic [Cohn and White, 2009, Hallman et al., 2007, 2009, Kay et al., 2012, Vale and White, 2006, White et al., 2002] or post-processed N-body methods [Bode et al., 2009, Sehgal et al., 2010] have been used to investigate the effect on individual cluster measurements and on the angular power spectrum of the summed map. For individual clusters, projection boosts the signal in a stochastic manner, producing skewness in the statistical likelihood of

the aperture-integrated signal at a given mass and redshift.

The density-squared dependence of the thermal emissivity of the ICM makes X-ray surface brightness less susceptible to projection relative to galaxy counts and SZ distortions. Point sources, particularly AGN, both internal and external to the host halo, are the dominant contaminant to intrinsic thermal emissions [*e.g.*, Atlee et al., 2011, Hart et al., 2011, Ma et al., 2012, Martini et al., 2009]. I ignore such contamination here, partly because bright point sources are typically excised in cluster images and partly because of uncertainties in describing X-ray point source populations in the halo model.

Deep and wide sky surveys will soon allow for large, overlapping samples of clusters with measured optical richness, X-ray luminosity, and thermal SZ amplitude. Analysis of the combined data provides the means to measure covariance of these properties in the massive halo population. Several recent simulation studies have begun to tease out the covariance of observed optical, millimeter, and X-ray signals [Angulo et al., 2012, Meneghetti et al., 2010, Noh and Cohn, 2011, 2012]. The recent study of Noh and Cohn [2012] employs $\sim 10^4$ partial sight-lines centered on massive haloes found at $z = 0.1$ in a $250h^{-1}$Mpc N-body simulation to study the correlation among observed cluster properties. Their Principal Component Analysis (PCA) analysis identified cluster orientation as a major contribution to property covariance, providing arguments for positive correlations in intrinsic signals.

The modeling cited above is based on cluster sight-lines derived from N-body and other dynamical simulations. A drawback to such studies is the limited statistical sampling inherent in finite-volume simulations, particularly of the massive haloes, which happen to be the most interesting objects in most studies, in the mean time.

In this dissertation, I present a semi-analytical halo model, which employs the halo mass function, bias, and two-point spatial correlation function to generate halo sight-lines using a Monte Carlo approach. Observable optical, SZ, and X-ray signals with intrinsic covariance are then introduced via scaling relations to each of the haloes in those sight-lines to create sky images.

The principle aim of this approach is to provide a low-cost method for estimating the effects of projection on measured cluster signals. Results from this approach can help guide simulation studies targeted to support analysis of specific observational samples.

1.6 Dissertation Layout

The projected halo model will be presented in Chapter 2, followed by its direct application, the study of line-of-sight projections in optical, SZ, and X-ray clusters, in Chapter 3. Contents of these two chapters will also appear in *Chen & Evrard, 2013 A* (to be submitted to MNRAS).

In Chapter 4, the model is extended to include covariances, and a subsequent study of projection effects on observed signal covariance is presented. The work in this chapter will appear in *Chen & Evrard, 2013 B*, which is currently in preparation.

Finally in Chapter 5, I present an attempt at applying the projected halo model to explain the stacked ensemble of velocity dispersions in optical clusters [Becker et al., 2007]. An empirical HOD model as well as a two-population color model are fitted using Markov Chain Monte Carlo (MCMC). The model explains the galaxy cluster velocity dispersion to a certain extend, but accurate fitting of the stacked distributions requires detail modeling of faint galaxies, whose observational data is scarce.

CHAPTER 2

The Halo Projection Model

2.1 The Analytical Framework

I use the generic term *signal* to represent a measurable property of a cluster, and also the source property of the halos producing the observable. Consider a halo massive enough to host a galaxy cluster lying at some redshift along the sightline to an observer. In general, the observed signal, $S^{\rm obs}$, of the cluster is a sum of $S^{\rm int}$, the chosen, or "target", halo's intrinsic signal, and a contribution from halos projected along the line-of-sight, $S^{\rm proj}$. The latter can be modeled as a discrete sum of contributions from halos along the line of sight,

$$\begin{aligned} S^{\rm obs}(M_{\rm t}, z_{\rm t}) &= S^{\rm int}(M_{\rm t}, z_{\rm t}) + S^{\rm proj}(M_{\rm t}, z_{\rm t}) \\ &= S^{\rm int}(M_{\rm t}, z_{\rm t}) + \sum_i \Delta S\,(M_{\rm i}, z_{\rm i}, \Delta\theta_{\rm i}\,|\,M_{\rm t}, z_{\rm t}). \end{aligned} \tag{2.1}$$

Here, $M_{\rm t}$ and $z_{\rm t}$ are the mass and redshift of the target halo, and $\Delta S\,(M_{\rm i}, z_{\rm i}, \Delta\theta_i\,|\,M_{\rm t}, z_{\rm t})$ is the projected partial signal function contributed by a halo of mass $M_{\rm i}$ located at redshift $z_{\rm i}$ and displaced by an angle $\Delta\theta_{\rm i}$ from the target halo. This function characterizes how much a projected halo will contribute to the observed signal of the target.

The summation in Eq. 2.1 covers a local angular patch in the direction of the target cluster. The probability of observing a projected halo of $M_{\rm i}$, $z_{\rm i}$ and $\Delta\theta_{\rm i}$ in the sightline of the target cluster is larger than one would expect along a random direction due to the

amplification caused by halo-halo correlations,

$$p^{\rm proj}(M, z, \Delta\theta\,|\,M_{\rm t}, z_{\rm t}) = p^{\rm ran}(M, z) + p^{\rm cor}(M, z, \Delta\theta\,|\,M_{\rm t}, z_{\rm t})$$
$$\propto n(M, z) + n(M, z)\xi_{hh}(M, z, \Delta\theta, M_{\rm t}, z_{\rm t}), \tag{2.2}$$

where $n(M, z)$ is the halo mass function. The first term represents the random chance of intercepting a projected halo of M and z and $p^{\rm cor}$ is the increased probability due to halo-halo spatial correlation (ξ_{hh}) with the target halo. I shall refer to signals due to the first term as "random" and those due to the second one as "correlated".

I model the halo-halo correlation by [*e.g.*, Sheth and Tormen, 1999]

$$\xi_{hh}(M, z, \Delta\theta, M_{\rm t}, z_{\rm t}) = b(M, z)b(M_{\rm t}, z_{\rm t})\xi(r_{hh}), \tag{2.3}$$

in which $b(M, z)$ is the halo bias function and $\xi(r_{hh})$ is the two-point matter correlation function and r_{hh} is the co-moving distance between the projected and target halos.

To enforce distinct halos, I impose a hard sphere exclusion near the target halo in the calculation, *i.e.*, no projected halo would have its center fall within the ${\rm R_{200}}^{\rm tar} + {\rm R_{200}}^{\rm proj}$ volume centered on the target one.

While the two-halo correlation with the target halo is included, I ignore spatial clustering of the random and correlated haloes. The variance in the projected signal component $S^{\rm proj}$ calculated by this model will therefore be a lower limit to the true value, since higher-order correlations describing clustering amongst the projected haloes will only increase the variance in $S^{\rm proj}$.

I employ both the mass function and the halo bias of [Tinker et al., 2008]. Haloes are assumed to be spherical objects with radial signal profiles explained below.

2.2 Fast Halo Sight-lines

I use the model above, Eq. 2.2, to generate Monte Carlo realizations of ensembles of small patches of synthetic sky surrounding a target dark matter halo. Each realization contains a different set of random and correlated projected halos, each of which is dressed with multivariate signals that are summed and filtered in ways discussed below. Ensembles of many thousands of individual targets allows us to investigate statistical properties of the observables in detail.

In each simulated sight-line, I first establish the target halo with mass $M_{\rm t}$ and redshift $z_{\rm t}$, then use a Monte Carlo method to populate the sight-line with projected haloes, including both random and correlated ones, using Eq. 2.2, the probability of observing a halo of mass M, redshift z, and angular separation $\Delta\theta$ from the target. To avoid extremely large angular sized halos, I apply a low redshift cutoff at $z = 0.01$. The sums extend to a maximum redshift, $z_{\rm max} = 2$, beyond which the number density of massive halos is strongly suppressed. The results are not strongly sensitive to these choices.

Numerically, using an inverse transform sampling of the cumulative probability function on the grid of M, z, and $\Delta\theta$ in the case of correlated haloes, with linear interpolation between grid points, I obtain a sky patch of 25 arcmin in radius, $z_{\rm max} = 2$ in depth and featuring all haloes above $M_{\rm min} = 2\times10^{11}h^{-1}{\rm M}_\odot$ in about 4 seconds on a single core.

2.3 From Halos to Observables

Regardless of one's choice of the analytical form or the simulated halo sight-lines, it is necessary to translate the dark matter halo representation into actual observables to make meaningful assessments of cluster projections. The reason is that, ultimately, we do not make direct observations of dark matter haloes, but their cluster counterparts at various wavelengths.

Given a simulated halo sight-line, I then translate the dark matter halo representation

into observables in order to assess the projection effects. I shall mainly focus on three wave-bands: optical, sub-millimeter, and X-ray. For signals at each wavelength, I first assign each halo in the sight-line a set of intrinsic signals, Π, comprised of $N^{\rm gal}$ for optical, $Y_{\rm SZ}$ for SZ, and $L_{\rm X}$ for X-ray, and then convert them into observed quantities S, comprised of a color-selected $N^{\rm gal}$, SZ flux, $f_{\rm SZ}$, and X-ray flux, $f_{\rm X}$.

2.3.1 Intrinsic Signals

I employ an HOD approach to model optical richness and use curved power-law scalings between SZ and X-ray signals and halo mass.

HOD models often use separate terms to describe central and satellite galaxies in massive haloes. The satellite component scales nearly linearly with halo mass in the general galaxy population [Zehavi et al., 2011] as well as for red-sequence galaxies [Coupon et al., 2012].

In this work, I adopt the red galaxy HOD model described in Coupon et al. [2012] for galaxies brighter than $\mathrm{M}_g - 5\log h = -19.8$. This magnitude limit roughly corresponds to the magnitude cut of $0.4L_\star$ used in the MaxBCG catalogue [Koester et al., 2007b]. The expected intrinsic optical signal will take the following form,

$$< \Pi_{\rm opt}(M', z) >= \frac{1}{2}(1 + {\rm erf}(\frac{\ln M' - \ln M'_{\rm min}}{\sigma_{\ln M'}}))(1 + (\frac{M' - M'_0}{M'_1})^\alpha), \tag{2.4}$$

comprised of a central galaxy part, determined by $M'_{\rm min}$ and $\sigma_{\ln M'}$, and a satellite galaxy part with two mass parameters M'_0 and M'_1, and a slope, α. A primed halo mass, M', is used here because Coupon et al. [2012] uses a halo mass defined with respect to 200 times the background matter density ρ_m, as oppose to $\rho_{\rm crit}$. I convert between the two conventions using an abundance matching approach described in Appendix D.

Values of the red galaxy HOD parameters in the three redshift regions separated by $z = 0.4$ and $z = 0.6$ are listed in Table. 2.1. The intrinsic optical richness of a given halo

Table 2.1: HOD Parameters

Redshift	$\log_{10} M'_{\rm min}$	$\sigma_{\ln M'}$	$\log_{10} M'_0$	$\log_{10} M'_1$	α
z <0.4	12.15	0.36	10.58	13.25	1.19
0.4 <z <0.6	12.10	0.26	8.37	13.19	1.22
z >0.6	12.14	0.25	11.65	13.21	1.22

From Coupon et al. [2012] Masses here are defined at a contrast of $\Delta = 200$ with respect to the background matter density, in units of $h^{-1}\mathrm{M}_\odot$.

follows a Poisson distribution with mean value given by employing these values in Eq. 2.4.

In sub-millimeter wavelengths, clusters are observed via the imprint of their SZ effect on the CMB. At low frequencies, the thermal SZ effect of clusters lowers the local CMB temperature by an amount determined by the integrated electron thermal pressure, $Y_{\rm SZ}$. The scaling of $Y_{\rm SZ}$ with mass is a subject under active investigation but a power law of slope close to the self-similar expectation of $5/3$ is generally supported by observations [*e.g.*, Planck Collaboration et al., 2011d].

At X-ray wavelengths, clusters are observed in the form of peaks in the X-ray flux map. For simplicity, I choose to use bolometric luminosity as the X-ray mass equivalent. A number of previous works have been done on $\ln L_{\rm X} - \ln M$ relations [Rykoff et al., 2008, Stanek et al., 2010]. The hot gas fraction in halos falls strongly below the group mass scale [*e.g.*, Dai et al., 2010]. To accommodate this aspect into the model, I use a curved power-law model for both SZ and X-ray signals,

$$< \ln \Pi(M, z) >= A + B \ln M + C(\ln M)^2 + D \ln(1+z) + E(\ln(1+z))^2, \qquad (2.5)$$

which includes second order terms in both mass and redshift. I employ values for these parameters taken from the preheated simulations of Stanek et al. [2010], reproduced in Table 2.2. The curvature terms are modest, and are mainly important for decreasing the SZ signal on galactic-halo mass scales.

Table 2.2: Observable-mass scaling relation parameters

Parameter	A	B	C	D	E	$\sigma_{\ln\Pi}$
SZ	-8.8102	1.5941	-0.0586	0.3080	-0.0141	0.12
X-ray	2.5285	1.7304	-0.0351	0.786	0.477	0.4

Unit of the intrinsic SZ signal, $Y_{\rm SZ}$, is $\rm h^{-2}Mpc^2$ and that of X-ray signal, $L_{\rm X}$, is $10^{44}\rm ergs^{-1}cm^{-2}$. Halo mass in Eq. 2.5 is a critical M_{200} in units of $10^{15}h^{-1}\rm M_\odot$.

2.3.2 Observable Signals

Given the intrinsic signals of the target, the next step is to convert them into observable signals received by a telescope.

For optical richness, red-sequence or photometric redshift selection will tend to filter galaxies in a manner peaked around the target halo redshift with some width σ_z [*e.g.*, Hao et al., 2010, Koester et al., 2007b, Rykoff et al., 2013].

I model this selection as a Gaussian filter in redshift space,

$$S_{\rm opt}(M, z|z_{\rm t}) = \Pi_{\rm opt}(M, z)\exp(-\frac{(z-z_{\rm t})^2}{\sigma_z(z_{\rm t})^2}) \tag{2.6}$$

with the filter width σ_z taken to be a function of redshift,

$$\sigma_z(z) = 0.03(1+z) + 0.2z^2 \tag{2.7}$$

This form roughly fits the redshift uncertainty seen in SDSS data out to $z \simeq 1$ [Oyaizu et al., 2008].

For SZ and X-ray, I convert the integrated $Y_{\rm SZ}$ and $L_{\rm X}$ in Eq. 2.5 into their proper fluxes with

$$S_{\rm SZ}(M, z) = \frac{\Pi_{\rm SZ}(M, z)}{d_A(z)^2} = \Pi_{\rm SZ}(M, z)\frac{(1+z)^2}{r(z)^2} \tag{2.8}$$

$$S_{\rm X}(M, z) = \frac{\Pi_{\rm X}(M, z)}{d_L(z)^2} = \Pi_{\rm X}(M, z)\frac{1}{(1+z)^2 r(z)^2}, \tag{2.9}$$

in which $r(z)$ is the co-moving metric distance to a source at redshift z.

2.3.3 Creating Sky Maps

In the final step of turning the halo sight-lines into observable sky patches, one needs to assign the observed signals to each halo with a proper profile. I generalize the projected signal profiles λ as seen in the sky into the following form,

$$\lambda(\theta) \propto g(\frac{\theta}{\theta_c}), \tag{2.10}$$

which contains θ_c, the angular size of the core radius (θ here is the angular distance to the center of the halo). The core radius relates to R_{200} via the following relationship,

$$R_c(M, z) = \frac{\mathrm{R}_{200}(M, z)}{c(M, z)}, \tag{2.11}$$

in which $c(M, z)$ is the concentration parameter.

I use the dark matter halo concentration given by Bhattacharya et al. [2013],

$$\begin{aligned} \bar{c} &= D(z)^{0.53} 6.6 \nu^{-0.41}\,, \\ \sigma_{\ln c} &= 0.37\,, \end{aligned} \tag{2.12}$$

where $\nu \equiv \frac{\delta_{sc}(z)}{\sigma(m)}$. The scatter in concentration is taken to be $\sigma_{\ln c} = 0.37$, independent of mass and redshift. For simplicity, I use the scale radius of the dark matter to set the scale radius of galaxies as well as the core radius of the ICM hot gas. We interpret the halo model literally in the sense that profiles are truncated at θ_{200}, with amplitudes re-normalized to yield the assumed scaling relations.

Because galaxies trace their underlying dark matter distribution, I use a projected Navarro-Frenk-White (NFW) profile [Bartelmann, 1996] for the the angular distribution

of optical galaxies,

$$g(x) = \begin{cases} (x^2-1)^{-1}(1 - \frac{2}{\sqrt{x^2-1}} \tan^{-1} \sqrt{\frac{x-1}{x+1}}) & x > 1 \\ (x^2-1)^{-1}(1 - \frac{2}{\sqrt{x^2-1}} \tanh^{-1} \sqrt{\frac{1-x}{x+1}}) & x < 1 \end{cases} \tag{2.13}$$

As for SZ and X-ray, assuming that the electron number density follows a β profile,

$$n_e(r) = n_{e0}(1 + (\frac{r}{r_c})^2)^{-3\beta/2}, \tag{2.14}$$

one can find the projected 2-D β profile for SZ,

$$g(x) = (1 + x^2)^{\frac{1-3\beta}{2}}; \tag{2.15}$$

and for X-ray,

$$g(x) = (1 + x^2)^{\frac{1}{2}-3\beta}. \tag{2.16}$$

In this study, I use a fixed β value of $\frac{2}{3}$ [Neumann and Arnaud, 1999].

Putting all the ingredients together, I show in Figure 2.1 views of a sky patch centered on a $M_{\rm t} = 5 \times 10^{14} h^{-1} {\rm M}_\odot$ and $z_{\rm t} = 0.3$ target with projected halos down to $M = 2 \times 10^{11} h^{-1} {\rm M}_\odot$ shown out to $z_{\rm max} = 2$. In the upper left panel, I plot the projected matter sky surface density, and in the other three panels, I display the same sky patch as observed in optical, sub-millimeter, and X-ray wavelengths. The optical panel displays galaxies filtered by redshift / color, while the SZ and X-ray panels present the respective sky surface brightnesses of the SZ decrement and X-ray flux. The X-ray sightline is clearly dominated by the target while the optical signal is more confused. Relative to the X-ray, the SZ is less centrally concentrated and more susceptible to high redshift contamination.

In Figure 2.2 I show the shape of the mean intrinsic and projected radial profiles around this target halo via stacking the simulated sky patches of the same target. Each signal is normalized to the mean intrinsic value within a θ_{200} aperture, thus the intrinsic profiles

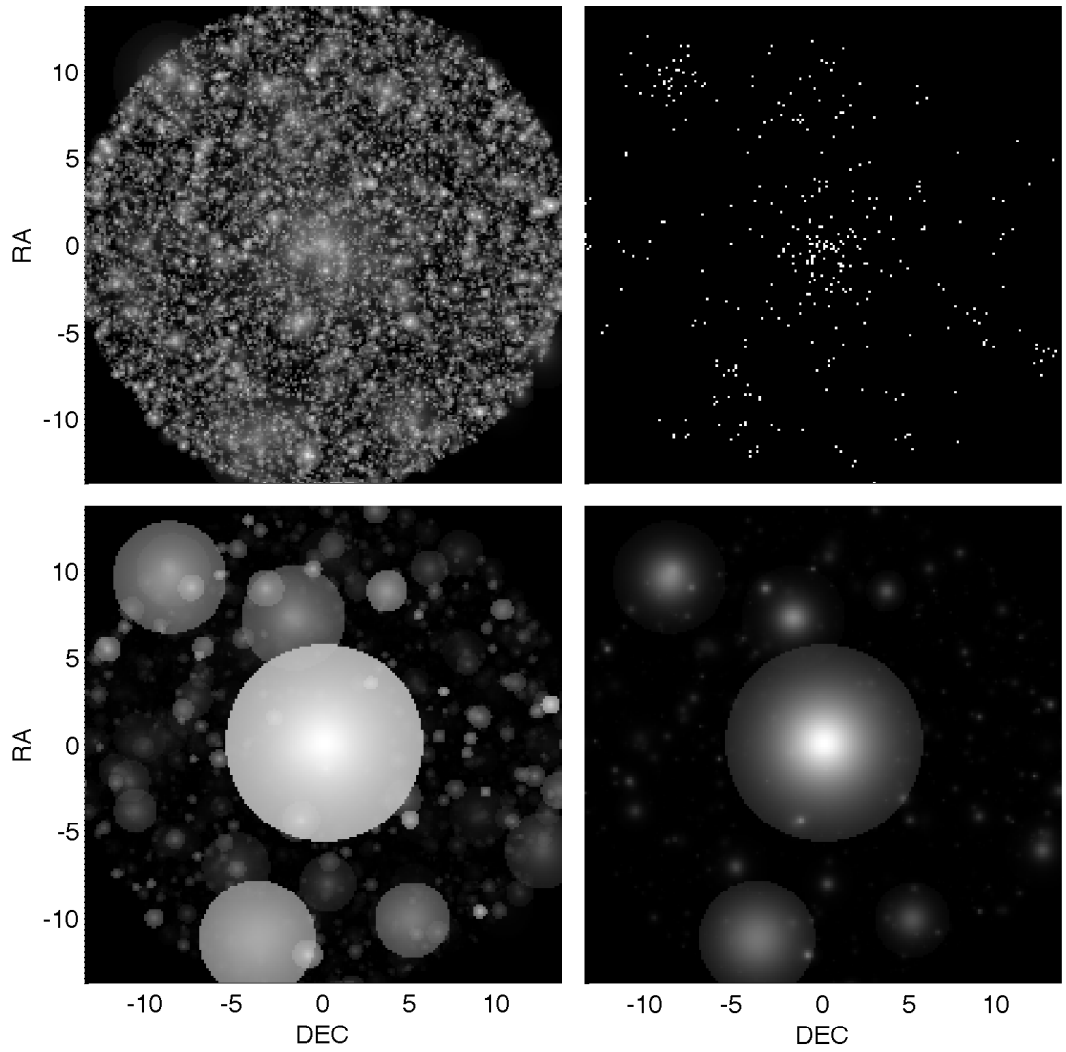

Figure 2.1: A simulated sky patch of 30 arcmin^2 centered on a target halo of $5\times10^{14}h^{-1}\mathrm{M}_\odot$ at $z_\mathrm{t} = 0.3$ as seen in projected dark matter sky surface density (upper-left), optical (upper-right), SZ flux (lower-left), and X-ray flux (lower-right). The optical panel contains only those galaxies whose magnitude is brighter than the cutoff implied by the HOD model and within the redshift filter as discussed in §2.3.2. In the other three panels, I plot the observed fluxes in 200×200 pixel maps and use a logarithmic color scale with a floor of 1% of the brightest pixel value.

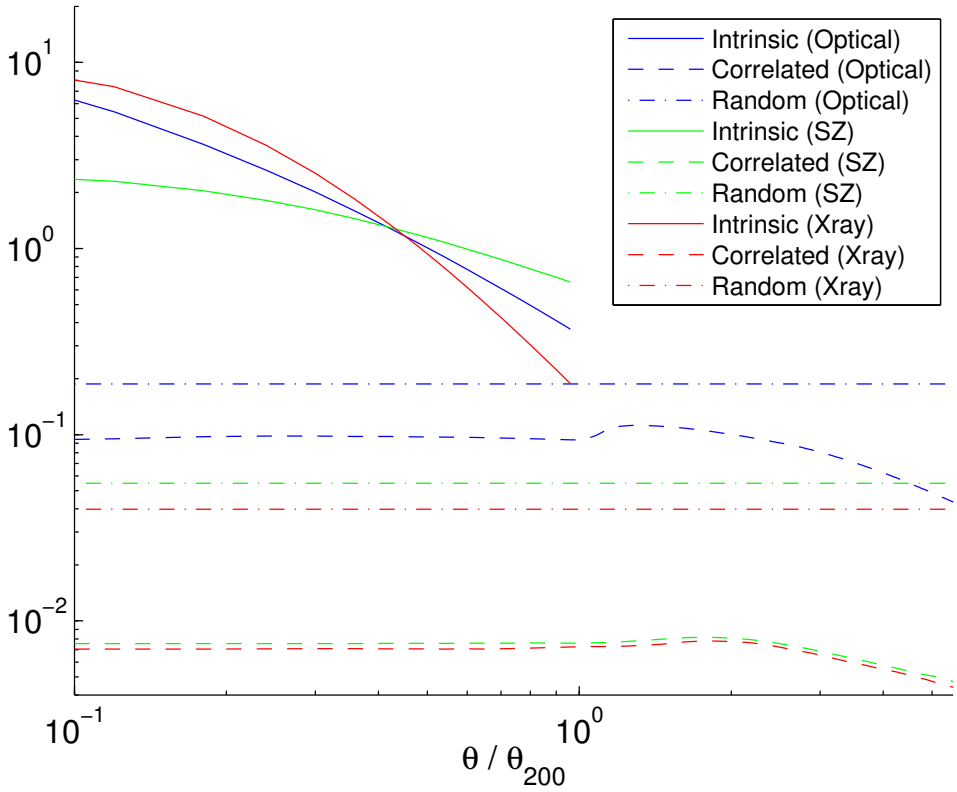

Figure 2.2: Scaled, angular profiles of optical (blue), SZ (green), and X-ray(red) wavebands, each broken down into its intrinsic (solid), correlated (dashed), and random (dot-dashed) components. The hard-sphere exclusion assumption creates the feature seen in the correlated component just beyond θ_{200}.

(solid lines) integrate to unity within the θ_{200} aperture, and the projected profiles represent fractional contributions to the intrinsic signal.

Projection in the optical is larger than the other wavebands, and the contribution from correlated halos (dashed lines) is a significant fraction of this total. The first feature reflects the shallower scaling relation slope in the optical, which allows contributions to $N^{\rm gal}$ from the more numerous haloes of lower mass, while the second feature reflects the relatively narrow length scale probed by the optical redshift filter, Equation 2.6, as discussed in § 3.1.2 below. The stronger mass scaling in the SZ and X-ray limits contributions to the projected partial signal function to a relatively rarified set of high mass haloes. Because of their wider redshift sensitivity, these signals are dominated by random projections; correlated halos contribute at a level below 1% of the intrinsic value.

2.3.3.1 Filtered Cluster Signals

The raw signal, $S^{\rm obs}(M_{\rm t}, z_{\rm t})$, computed above is convolved with a set of simple angular filters, $f^{\rm filt}(\theta)$, centered on the target halo. The projected component is then,

$$S^{\rm obs}(M_{\rm t}, z_{\rm t}) = \sum_{\rm i} S_{\rm i}(M_{\rm i}, z_{\rm i}) \int_{\Omega} \lambda(\theta, \phi \,|\, \theta_{\rm i}, \phi_{\rm i}) f^{\rm filt}(\theta) {\rm d}\Omega, \tag{2.17}$$

in which θ is the angular separation from the target centre, $S_{\rm i}$ is the observable signal as in Eq. 2.6, 2.8, and 2.9; and λ is the unitary-normalized version of the angular profile function, Equation 2.10. For more details, refer to Appendix B.

I consider three typical filtering scenarios: a simple top-hat; local background subtraction, and matched filter.

The top-hat filter simply sums the total signal within the known θ_{200} aperture centered on the target,

$$f^{\rm top-hat}(\theta) = \begin{cases} 0, & \theta > \theta_{200} \\ 1, & \theta < \theta_{200} \end{cases} \tag{2.18}$$

The θ_{200} top-hat filter measures the amplitude of projected signal onto the face of the cluster.

The second approach is a local Background Subtracted (Bg-sub) filter,

$$f^{\rm bg-sub}(\theta) = \begin{cases} 1, & \theta < \theta_{200} \\ -1, & \sqrt{3}\times\theta_{200} < \theta < 2\times\theta_{200} \\ 0, & otherwise \end{cases} \tag{2.19}$$

which subtracts signal that falls within an annulus defined by radii of $\sqrt{3}\theta_{200}$ and $2\theta_{200}$. The area enclosed in this region is equal to the area of the θ_{200} top-hat filter itself. Annulus subtraction techniques similar to this are commonly used in X-ray cluster analysis. While background subtraction can be performed either locally or globally in general, local background subtraction has the advantage of including part of the correlated component in the projected signal.

The third approach is a matched filter, which applies a weighted function to the sky map whose shape is taken to be the mean profile of each target signal, *i.e.*, the optical sky map will be convolved with a matched filter proportional to its profile in Eq. 2.13, and similarly for SZ and X-ray.

$$f^{\rm matched}(\theta) \propto g(\theta), \tag{2.20}$$

where $g(\theta)$ are the projected profiles of Eq. 2.13, Eq. 2.15, and Eq. 2.16. The amplitude is normalized such that the target cluster by itself would yield an observed signal $S^{\rm obs}(M_{\rm t}, z_{\rm t})$ equaling to itself $S^{\rm int}(M_{\rm t}, z_{\rm t})$ after the convolution.

When realizing a target halo, I allow the concentration to vary as a log-normal with scatter $\sigma_{\ln c} = 0.37$. Applying a single matched filter to the ensemble of targets will not necessarily return an unbiased average, and there will certainly be variance in the filtered signal induced by the use of a single profile. Filtering each instance with a filter tuned to its own concentration eliminates this source of variance, but at present there is no simple

way to apply this approach to large samples of observed clusters.

The model is idealized in several respects. First, I assume the perfect knowledge of the target halo center and redshift. There is no mis-centering, an effect that can wash out target signal and increase the importance of projection. Second, I assume perfect knowledge of the angular scale radius, θ_{200}, of the target halo. These idealizations mean that the effects of projection on the expected mean and variance of observed signals should be treated with some caution. Complementary analyses of synthetic simulated skies are necessary to determine a more complete picture of projection expected for specific survey data.

2.3.4 Special Cases

In the process of producing the multi-wavelength sky patch realizations as described in the previous sections, I come across several scenarios that require special treatment.

The first issue involves rare cases where a single projected halo overwhelms the target. I argue that, in these instances, the original "target halo" should be replaced by the largest contributing halo. Such patches are discarded in the simulation to avoid double counting. For reference, the fraction of these systems are 0.02% in Optical, 0.1% in SZ, and 0.4% in X-ray for a $M_{\rm t} = 5 \times 10^{14} h^{-1} {\rm M}_{\odot}$, $z_{\rm t} = 0.3$ target [1].

A second class of instances, which I do not discard, are cases in which the projection contamination is strong. I define Heavily Projected (HP) clusters as those for which the observed, filtered signal is more than 2.5 standard deviations larger than its intrinsic value,

$$\ln S^{\rm obs}_{\rm HP}(M_{\rm t}, z_{\rm t}) > \overline{\ln S^{\rm int}}(M_{\rm t}, z_{\rm t}) + 2.5\sigma_{\ln S}(M_{\rm t}, z_{\rm t}). \tag{2.21}$$

If there were no projections and all intrinsic signals are indeed log-normally distributed, the chance of observing such events is 0.62%. With line-of-sight projections, this likelihood will undoubtedly becomes larger. Scenarios categorized as HP will more likely be mis-

[1] The larger fraction in X-ray is caused by realizing haloes as close as $z_{\rm min} = 0.01$.

interpreted as a more massive halo and thus distort the inferred mass distribution at fixed $S^{\rm obs}$, as I shall show later in § 3.3.

Finally, when using the Bg-sub filter in Eq. 2.19, there is a chance that one or more sizable halos could lie in the subtraction annulus such that one would over-subtract, potentially resulting in an unphysical (negative) value for the filtered $S^{\rm obs}$. I consider it more likely for observers to notice the large companion in the outer annulus and hence make rational *ad hoc* modifications to avoid if encountered in real observations. For the above reasoning, I shall refer to cases in which $S^{\rm obs}$ is less than 50% of $S^{\rm int}$ as "over-subtracted" and not include in the following analyses. The fractions of such systems are 0.03% in Optical, 0.01% in SZ, and 0.4% in X-ray for a $M_{\rm t} = 5\times10^{14}h^{-1}{\rm M}_\odot$, $z_{\rm t} = 0.3$ target [2].

[2]The larger fraction in X-ray is caused by realizing haloes as close as $z_{\rm min} = 0.01$.

CHAPTER 3

Projection Effects on Galaxy Clusters

3.1 Projections of a Fixed Target

I begin with a benchmark case of a target halo with fixed mass of $M_{\rm t} = 5\times10^{14}h^{-1}{\rm M}_{\odot}$ at redshift $z_{\rm t} = 0.3$. Under a WMAP7 cosmology, one expects to find 370 haloes more massive than this one in the full sky between redshift 0.25 and 0.35, corresponding to a sky surface density of 1 per $100\,{\rm deg}^2$. Such target is a typical cluster that can be found in existing optical, SZ, and X-ray surveys.

Using the scaling relations presented in § 2.3.1, the target will have the following intrinsic properties

$$
\begin{aligned}
< N(M_{\rm t}, z_{\rm t}) > &= 71.0, \\
\exp < \ln Y(M_{\rm t}, z_{\rm t}) > &= 5.20\times10^{-5}{\rm h}^{-2}{\rm Mpc}^2, \\
\exp < \ln L(M_{\rm t}, z_{\rm t}) > &= 4.72\times10^{44}{\rm erg\ s}^{-1}{\rm cm}^{-2}.
\end{aligned}
$$

3.1.1 Observed Signals with Projection

I first examine shifts in the distribution of observed filtered signals relative to the intrinsic input distribution. Recall that the shape of the intrinsic variance is Poisson for optical counts and log-normal for the SZ and X-ray signals, with scatter of 0.12 and 0.40 in $\ln Y_{\rm SZ}$ and $\ln L_X$, respectively. I quote biases in the expected mean as well as the relative scatter

Table 3.1: Projection in Optical Clusters

Filter Type	Top-hat	Matched	Bg-sub
$< S^{\rm obs}/S^{\rm int} >$	1.158	1.067	0.996
$< \sigma_{\ln S} >$	0.125	0.182	0.165
HP fraction	9.25%	9.11%	1.89%

in $S^{\rm obs}$ at each of the three wavelengths.

I produce 30,000 realizations of sky patches centered on the reference target and process their signals with the top-hat, matched, and Bg-sub filters to obtain three measurements of $S^{\rm obs}$. The 30,000 realizations reduce the statistical uncertainties to the third significant digit.

3.1.1.1 Optical

Figure 3.1 shows the frequency distribution of intrinsic (halo) and observed (cluster) optical richness for the reference target. In the optical, line-of-sight projections using the Coupon et al. [2012] red galaxy HOD have a significant effect on observed counts using a straightforward top-hat filter within the θ_{200} target aperture. The mean increase in $S^{\rm obs}$ due to projection is 16% and in 9.3% of the time, the target will exhibit a $S^{\rm obs}$ more than 2.5 standard deviations away from the intrinsic mean, thus becoming "heavily-projected" in our definition. There is also a slight increase in the observed signal scatter, going from 11.9% in $\ln N^{\rm gal}$ without projections to 12.5% with them.

Applying the simple (non-compensated) matched filter reduces the overall signal bias from 16% in the top-hat scenario to 6.7%. It barely changes the HP fraction, which still hovers slightly above 9%. Although the matched filter does significantly reduce the signal bias on expectation, it possesses the undesired side-effect of amplifying the variance. The observed signal variance increases substantially, to 18.2%. This increase in scatter is due to both variations in intrinsic shape of the cluster profile – the intrinsic concentration varies for each target instance – as well as cosmic variance in the projected population. The latter

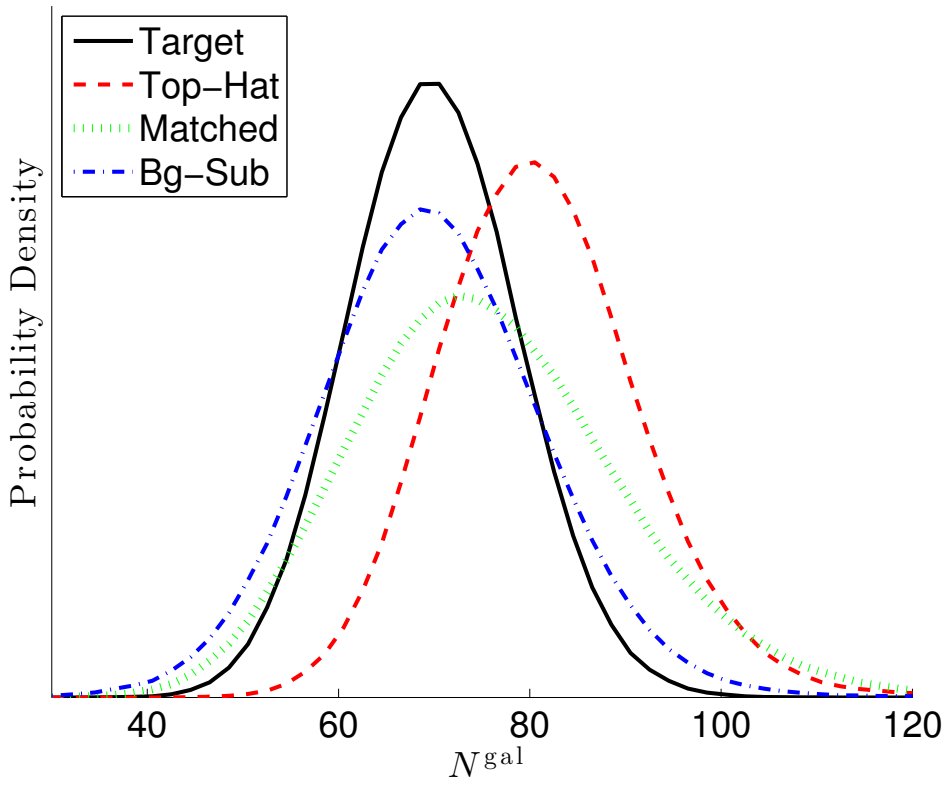

Figure 3.1: Distributions of optical richness, $N^{\rm gal}$, for a fixed $M_{\rm t} = 5 \times 10^{14} h^{-1} {\rm M}_{\odot}, z_{\rm t} = 0.3$ target are shown. The intrinsic, Poisson distribution (black, bold solid) is compared to versions of observed richness that include the effects of projection under top-hat filtering (red, dashed), a simple matched filter (green, dotted) and local background subtraction (blue, dot-dashed). Values of the mean and scatter for the observed distributions are listed in Table 3.1.

Table 3.2: Projection in SZ Clusters

Filter Type	Top-hat	Matched	Bg-sub
$< S^{\rm obs}/S^{\rm int} >$	1.061	1.053	1.001
$< \sigma_{\ln S} >$	0.127	0.131	0.138
HP fraction	3.16%	3.19%	1.60%

effect is a lower limit, since the random component of our model lacks spatial clustering.

The local Bg-sub filter performs almost perfectly in removing signal bias in the mean. While the random component is expected to cancel out, removal of the correlated component is not guaranteed due to its radial profile structure (Figure 2.2).

Similar to the matched filter case, local annulus subtraction also adds to the signal variance, increasing the scatter to 16.5%. This increase mainly arises from the fact that the variance in this filtered signal is the summed variance of the pseudo-independent signal and background regions, hence the enlargement by roughly $\sqrt{2}$ in the scatter.

3.1.1.2 SZ

Figure 3.2 shows the frequency distribution of intrinsic and observed thermal SZ effect for the reference target. The basic level of SZ signal contamination measured by the θ_{200} top-hat measurement is a boost of 6.1%, roughly a factor three smaller than the mean optical projection. Correspondingly, the HP fraction declines is lower at 3.2%, small but still a factor five larger than the 0.62% intrinsic value. The scatter in log-signal remains dominated by intrinsic variations, the observed top-hat filtered scatter is 12.7%, hardly changed from the 12% input value.

The matched and Bg-sub filters behave similarly to the optical case. The matched filter reduces the overall signal bias to 5.3% and background subtraction removes the bias almost perfectly. For reasons explained in the previous subsection, the standard deviation in log-signal increases to 13.1% for the matched filter and to 13.8% for the background-subtracted one.

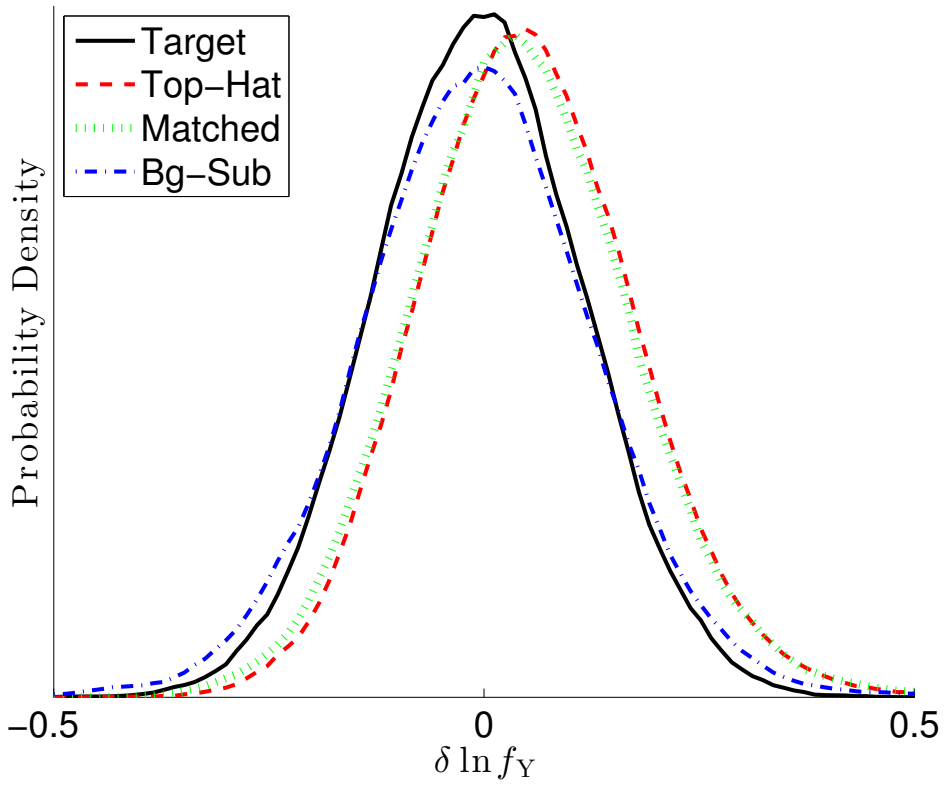

Figure 3.2: The distribution of SZ signals for the reference target halo is shown using the same format as Figure 3.1.

Table 3.3: Projection in X-ray Clusters

Filter Type	Top-hat	Matched	Bg-sub
$< S^{\rm obs}/S^{\rm int} >$	1.043	1.015	0.999
$< \sigma_{\ln S} >$	0.392	0.463	0.410
HP fraction	0.67%	1.64%	0.66%

3.1.1.3 X-ray

Figure 3.3 shows the frequency distribution of intrinsic and observed thermal X-ray flux for the reference target. It is obvious from Table.3.3 that the X-ray suffers a lesser degree of projections to begin with, both in terms of the overall 4.3% bias and the 0.67% heavily-projected fraction, the latter of which is almost on par with the 0.62% expected from intrinsic variations alone. The small HP fraction is a consequence of the larger intrinsic variance, $\sigma_{\ln S^{\rm int}} = 40\%$; the mean projected signal enhancement of 4.3% is a much smaller fraction of the intrinsic scatter, and chance projections that overwhelm the target flux are removed from our patch samples.

An interesting feature here is that the top-hat scatter about its mean is actually slightly lower than the intrinsic value. The primary source of variance in the projected signal is cosmic variance in the halo sight-line population, which fluctuates at roughly the 7% level for X-ray. Adding a much less volatile component to the intrinsic signal that has 40% scatter results in a smaller $< \sigma_{\ln S} >$ because the effect on the mean is larger than that of the scatter.

Similar to the results in Optical and SZ, applying the matched filter reduces the overall bias to 1.5% while the background-subtraction removes it completely. The steeper radial filter makes the matched filter more sensitive to the location of projected halos; well aligned projections lead to larger boosts in signal, as seen in Figure 3.3. The variance and HP fractions are therefore largest for this filtering scheme. Background subtraction enlarges the scatter by only a small amount, but I would like to caution that the background modeled here ignores the dominant point source contributions.

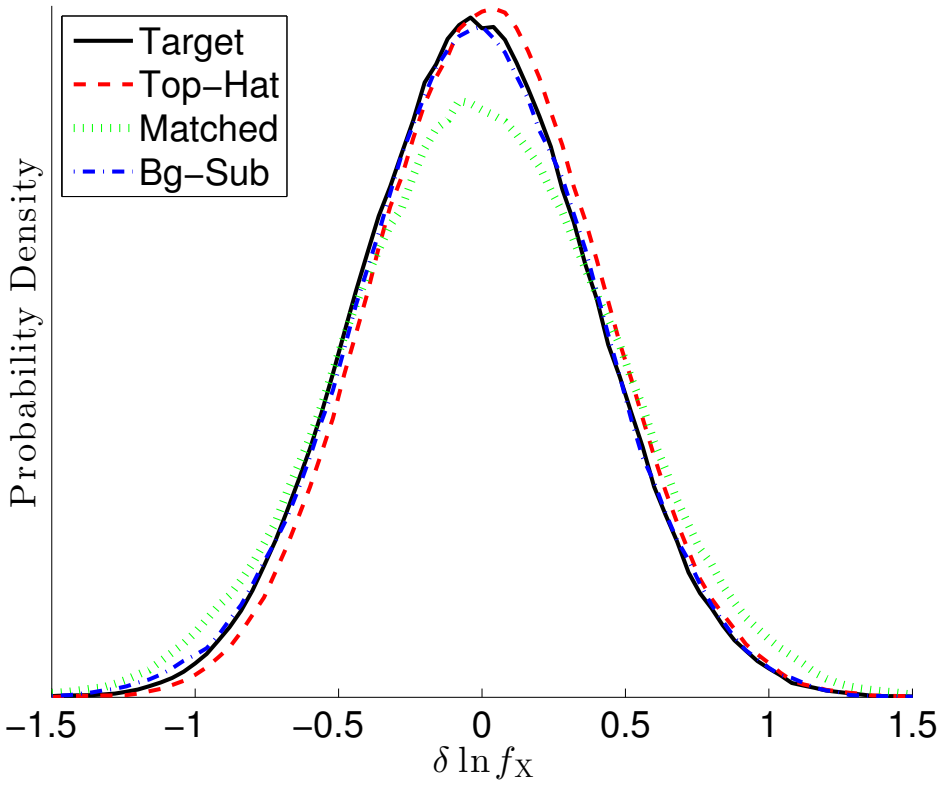

Figure 3.3: The distribution of X-ray signals for the reference target halo is shown using the same format as Figure 3.1.

3.1.2 Demographics of Projection Sources

In this section, I examine the demographics of projection for the reference halo by examining contributions to the top-hat filtered signal as a function of projected halo mass and redshift.

The upper panel of Figure 3.4 shows the cumulative contribution to the θ_{200} top-hat signals as a function of projected halo mass. In the SZ and X-ray, the super-linear scaling relations with mass limit projected contributions to the target halo from haloes above $1\times10^{13}h^{-1}\mathrm{M}_{\odot}$. In contrast, about half of the projections in the optical signal come from haloes below $4\times10^{12}h^{-1}\mathrm{M}_{\odot}$ in mass and only about 25% come from systems more massive than $1\times10^{13}h^{-1}\mathrm{M}_{\odot}$. The convergence below $1\times10^{12}h^{-1}\mathrm{M}_{\odot}$ in the upper panel of Fig. 3.4 marks the point at which halos are not expected to host a red galaxy brighter than the magnitude limit. The shape of the HOD creates a plateau in halo mass between $1\times10^{12}h^{-1}\mathrm{M}_{\odot}$ and $6\times10^{12}h^{-1}\mathrm{M}_{\odot}$) within which halos are likely to host a single galaxy. Because of their sheer numbers, haloes in this mass range contribute a large fraction of the observed count within the top-hat filter.

Along the redshift direction, it can be seen in the lower panel of Fig. 3.4 that both SZ and X-ray signals are subjected to projections along a wide redshift range. The less than 4 percent overall X-ray projection is split nearly equally between foreground and background, whereas the 6 percent projected signal in SZ is dominated by gas in high redshift haloes. In the optical, the redshift filter I assume for red-sequence galaxies, Eq. 2.7, limits contributions to a narrow redshift range centered on the target.

3.1.3 Correlated Projections

Figure 3.4 also shows the contributions to the top-hat filtered signals from spatially correlated halos as dashed lines. The correlated component adds 6 percent to the optical richness, about one-third of the overall top-hat filtered projection. The contribution to SZ or X-ray signals is at the level of ~ 0.6 percent overall, a small fraction of the random projected

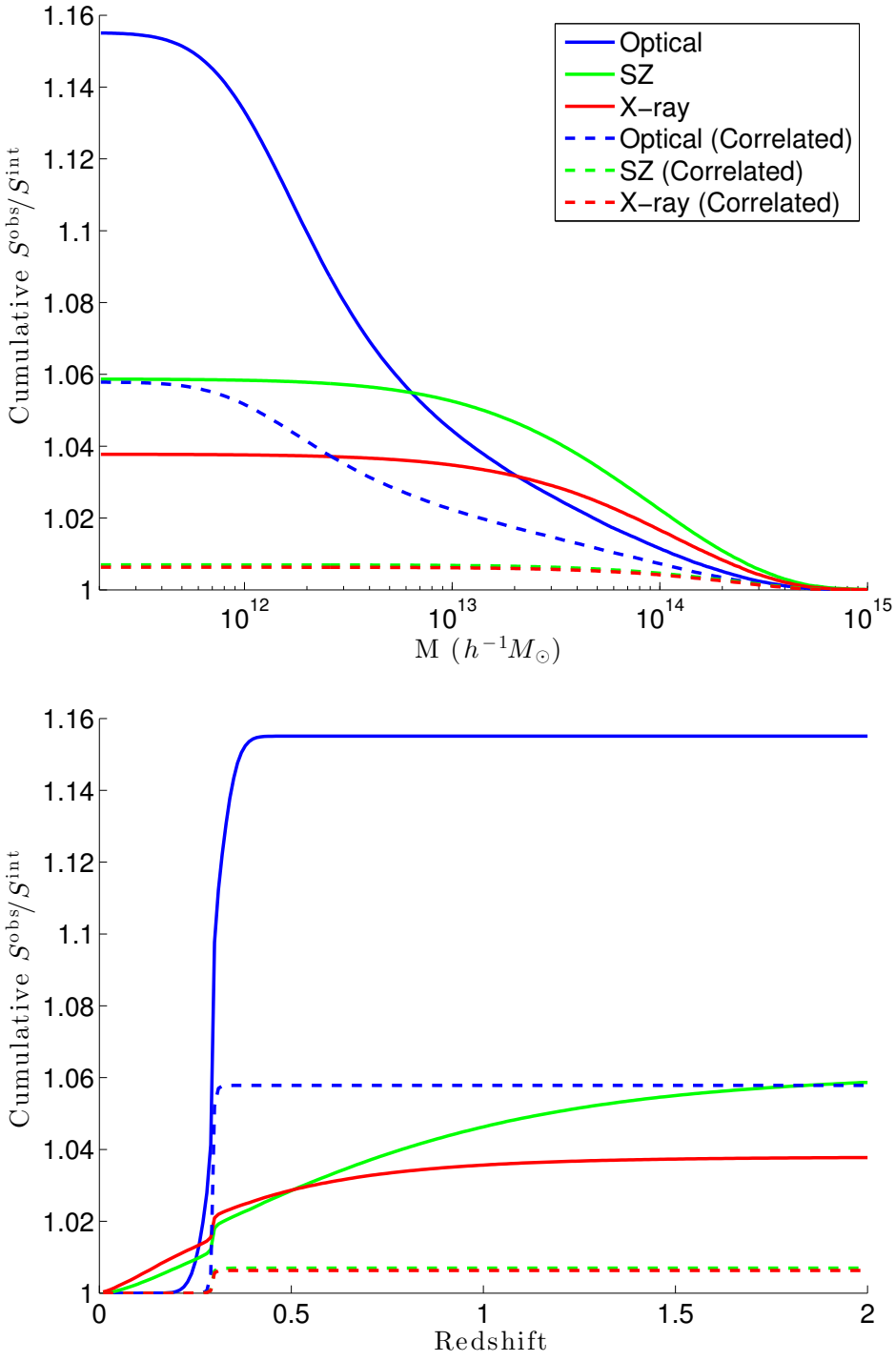

Figure 3.4: Cumulative observed signal over intrinsic signal as one sum the projected contributions along haloes of different mass (top panel), and along redshift (bottom panel), for a target mass of $M_t = 5 \times 10^{14} h^{-1} M_\odot$ at $z_t = 0.3$. For comparison across different wavelengths, observed signals are collected within the θ_{200} of the target with a top-hat window function.

contribution. These results reflect the fact that correlated projections reside in a relatively narrow bin in redshift space.

These differences in projection signatures lead to different trends when we vary the target mass and redshift in the next section. It also has a strong influence on the signal covariance, which I will discuss in Chapter 4.

3.2 Projection as a Function of Target Mass and Redshift

After studying projections on a fixed target, I move on to explore its behaviors as a function of target halo mass and redshift. I study these dependencies separately by fixing one parameter and varying the other, using the target halo of the previous section as a benchmark.

When varying redshift, I choose not to keep the target mass fixed, but instead employ a halo mass that matches the sky surface density of the reference $M_{\rm t} = 5\times10^{14}h^{-1}{\rm M}_\odot$ and $z_{\rm t} = 0.3$ target halo. For more details of this varying mass scale along redshift, refer to Appendix C.

3.2.1 Varying Target Halo Mass at $z = 0.3$

For target halos at $z_{\rm t} = 0.3$, Figure 3.5 presents trends in the mean projected $S^{\rm obs}/S^{\rm int}$ (solid lines) as well as its standard deviation (shaded colors) as a function of halo mass ranging from the group scale, $M_{\rm t} = 10^{13.8}h^{-1}{\rm M}_\odot$, to rich clusters, $M_{\rm t} = 1\times10^{15}h^{-1}{\rm M}_\odot$. The upper panel shows top-hat filtering while the lower panel shows local background subtracted signals. Results using the matched filter exhibit trends similar to an interpolation between these two cases, *i.e.,* the bias is reduced from the top-hat scenario but not to zero, so I choose not to present them explicitly here.

In the upper panel of Fig. 3.5, the overall (top-hat) projection amplitude, $S^{\rm obs}/S^{\rm int}$, increases as the target mass decreases. The driving factor here is the decrease in the denominator, $S^{\rm int}$, as one moves to less massive targets. optical clusters see their projec-

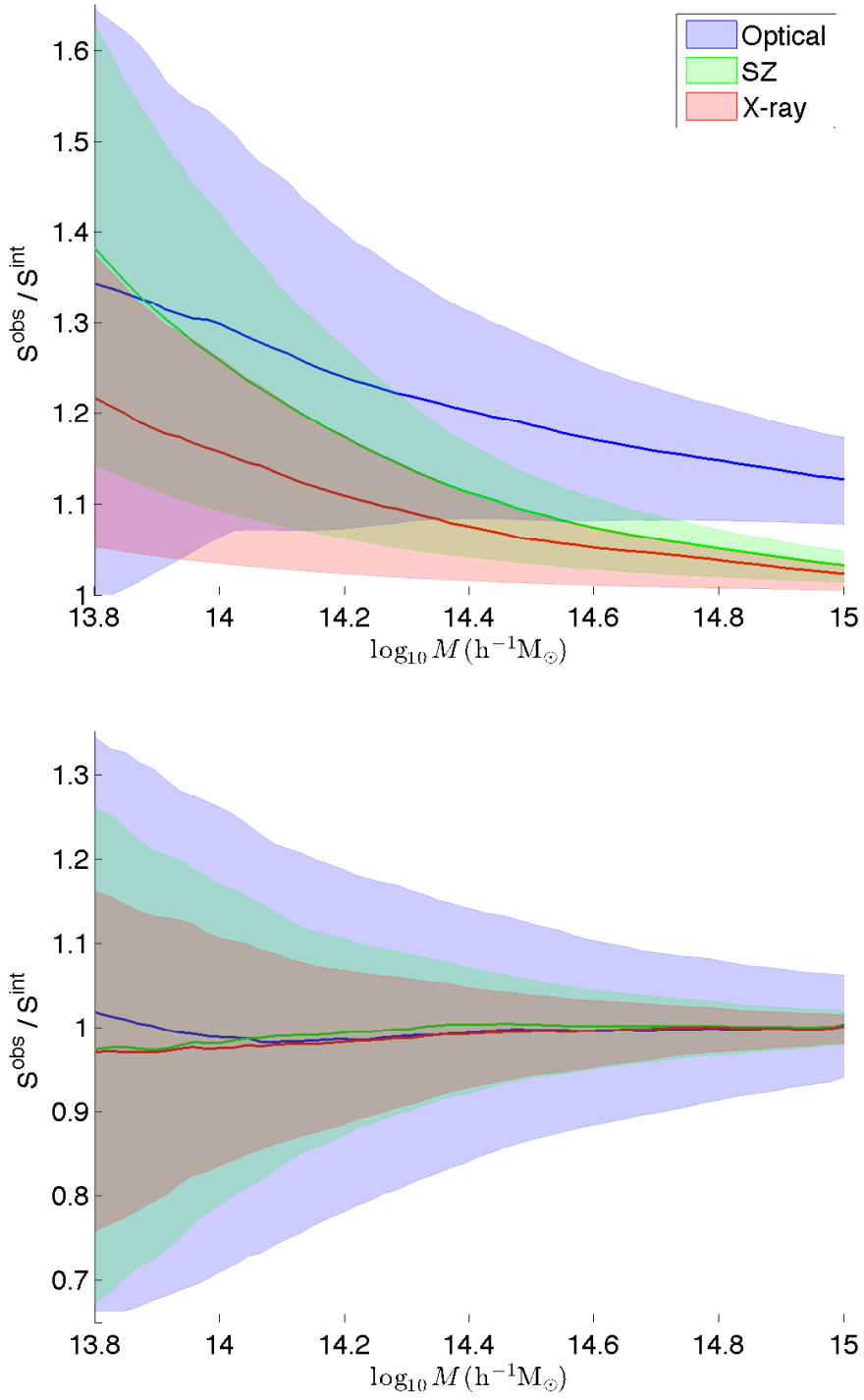

Figure 3.5: The expected value of $S^{\mathrm{obs}}/S^{\mathrm{int}}$ (solid lines) and 68%-quantile range (shaded) for the ratio of observed to intrinsic signals as a function of target halo mass at $z_{\mathrm{t}} = 0.3$. In the top panel, S^{obs} is calculated using a top-hat filter within θ_{200} while the bottom panel uses local background subtraction in an annulus between $\sqrt{3}\theta_{200}$ and $2\theta_{200}$.

tion enhancement grow from 13% at $M_{\rm t} = 1\times10^{15}h^{-1}{\rm M}_\odot$ to 34% at $M_{\rm t} = 6\times10^{13}h^{-1}{\rm M}_\odot$. Across the same mass range, the top-hat contribution to $S^{\rm obs}$ grows from 2.3% to 22% in X-ray and from 3.2% to 38% in SZ. The mean projected signal in SZ exceeds that in the optical for $M_{\rm t} < 10^{13.9}h^{-1}{\rm M}_\odot$.

In the optical, the intrinsic signal changes more gradually than that of the SZ and X-ray as a function of mass, resulting in a smaller gradient in $S^{\rm obs}/S^{\rm int}$. Furthermore, a significant portion of the projection comes from the correlated structure, which is proportional to the halo bias, so as the target mass decreases, the correlated contribution diminishes. Both the SZ and X-ray projections are dominated by the random component instead of the correlated one, which simply scales linearly with the halo's sky area, $\pi{\theta_{200}}^2 \propto {M_{200}}^{2/3}$. When combined with their intrinsic slopes near $\alpha \sim 5/3$ for these scaling relations, one expects $S^{\rm proj}/S^{\rm int} \propto M_{\rm t}^{-1}$, close to the behavior seen in the model calculations.

In the lower panel of Fig. 3.5, I apply the Bg-sub filter, which performs well in removing the projection induced bias across the mass range shown. The shaded areas in the plot show that the scatter in $S^{\rm obs}$ becomes larger at lower target masses, growing from 12%, 4.0%, and 3.5%, to 68%, 59%, and 40%, in optical, SZ, and X-ray, respectively, across the mass range shown.

Even though variances are kept constant in both SZ and X-ray intrinsic log-signals, as I have discussed in § 3.1, cosmic variance dominants the projected component uncertainty and its magnitude depends on the $\pi\theta_{200}$ sky area, which increases as the area gets smaller. Furthermore, the denominator in $S^{\rm obs}/S^{\rm int}$ becomes smaller as $M_{\rm t}$ decreases, exacerbating the amplification in signal variance we see in Fig. 3.5.

3.2.2 Varying Target Halo Redshift

When varying the target redshift, I choose not to simply use a constant mass because a $5\times10^{14}h^{-1}{\rm M}_\odot$ halo is much rarer at redshift of 1 than redshift of 0.3. Instead, I set the target mass by requiring that the sky surface density match that of our benchmark $M_{\rm t}$ =

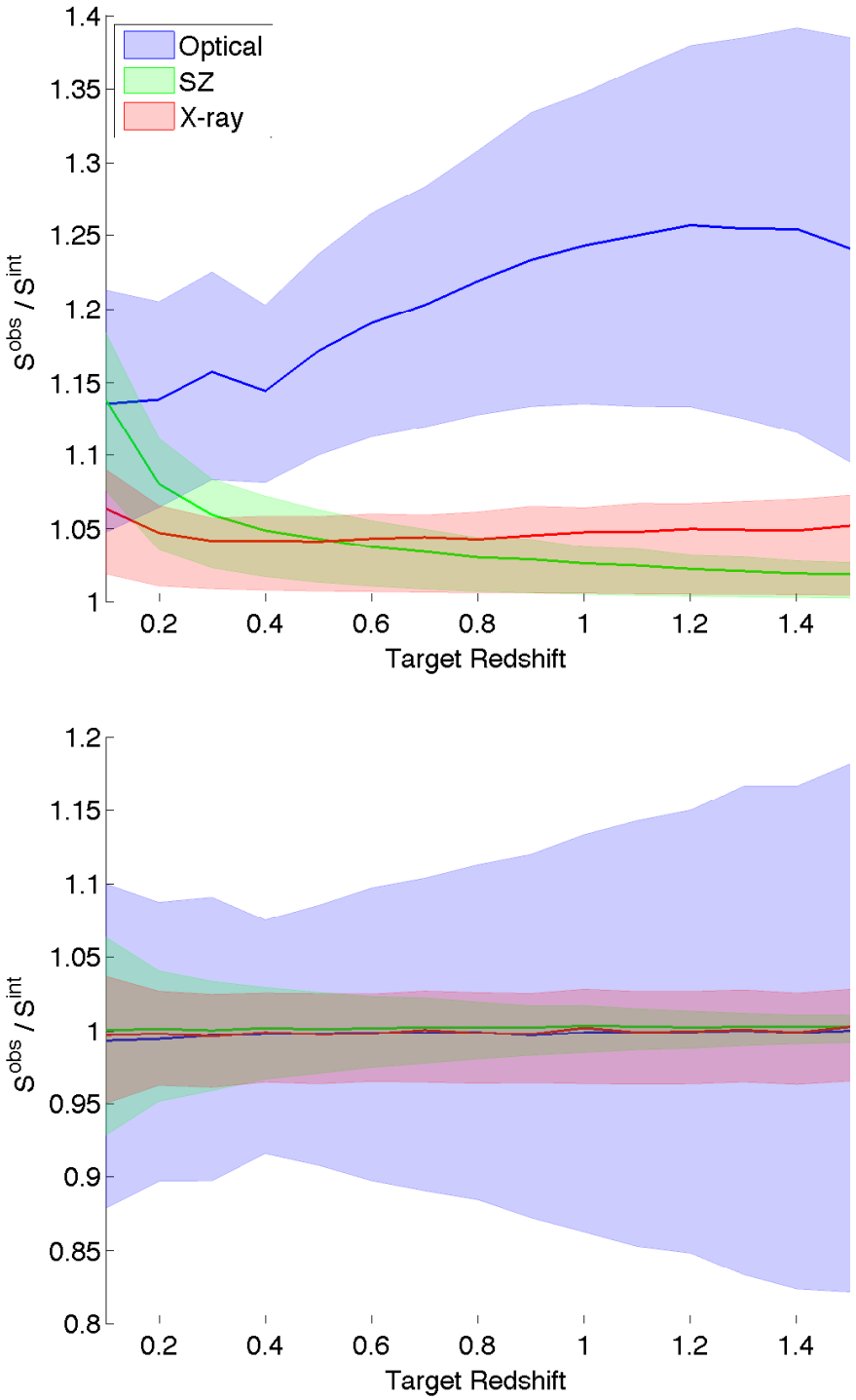

Figure 3.6: Similar to Figure 3.5, but showing behavior as a function of target redshift instead of mass. The target mass is varied with redshift to maintain a fixed sky surface density of target haloes (see text and Figure C.1).

$5\times10^{14}h^{-1}\mathrm{M}_{\odot}$ halo at $z_{\mathrm{t}} = 0.3$, which translates to a density of 1 per $\sim$ 100 deg^2. The target mass set this way is peaked near $z = 0.3$ and declines at lower and higher redshifts, falling to $2\times10^{14}h^{-1}\mathrm{M}_{\odot}$ at $z = 1.4$. Figure C.1 in Appendix C provides details.

In the upper panel of Figure 3.6, I compute $S^{\mathrm{obs}}/S^{\mathrm{int}}$ using the simple top-hat filter. The most striking feature is how the projection amplitude in the optical signals changes much differently compared to that in the SZ and X-ray. In those two wavebands, projections are dominated by the random component, which is a plain function of the sky area $\pi{\theta_{200}}^2$ covered by the target, thus the trend in $S^{\mathrm{obs}}/S^{\mathrm{int}}$ can be easily described by the ratio between the target $\pi{\theta_{200}}^2$ and its intrinsic signal flux. In the X-ray, the decreasing intrinsic flux with redshift means that top-hat projection effects are larger than those of SZ at $z > 0.6$.

In the optical, the trend is more complicated as multiple factors come into play. The ratio between the two correlated and random contributions increases weakly as a function of redshift (as can be seen in Figure A.1 in Appendix A). Within the correlated component itself, the behavior is not trivial as the halo-halo bias tends to increase the projection while the decline in the massive halo space density at earlier epochs pulls in the opposite direction. Another contributing factor is fact that the redshift filter, Eq. 2.6, widens with redshift. This effectively lengthens the projection cylinder at higher redshift which correspondingly increases the projection amplitude. Generally speaking, the upward trend in $S^{\mathrm{obs}}/S^{\mathrm{int}}$ before redshift of 1.2 is caused by the combination of an increased correlated projection and a larger effective cylindrical volume, whereas the decline beyond $z = 1.3$ is mainly due to the drop in the halo mass function.

The lower panel in Figure 3.6 shows that the Bg-sub filter works extremely well in removing the projection induced signal bias along the entire redshift range from 0.1 to 1.5.

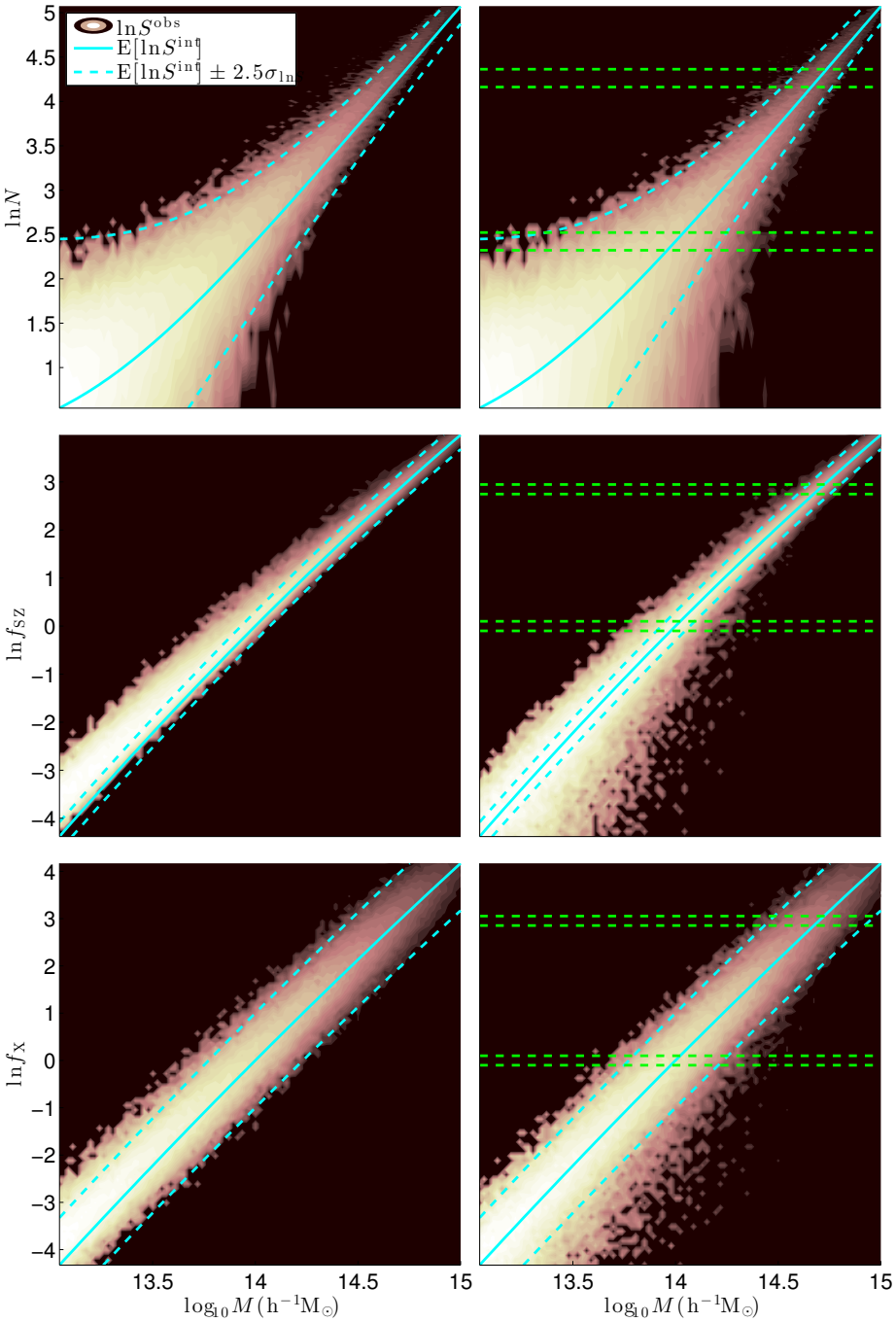

Figure 3.7: Population densities of haloes at $z_{\rm t} = 0.3$ are shown in the $\ln S^{\rm obs} - \log_{10} M$ plane for Optical, SZ, and X-ray (top to bottom) signals. The left-hand-panels show θ_{200} top-hat filtering while the right-hand panels are obtained using the local background subtraction filter. The expected log-mean $S^{\rm int}$ values are shown in solid cyan lines, and the range of $\pm 2.5\sigma_{\ln S^{\rm int}}$ in dashed. Systems that lie above the top dashed line are those defined to be "Heavily-Projected". The green horizontal dashed lines in right panels show the signal selection ranges for haloes in Figure 3.8.

3.3 The Effect on Inferred Halo Mass

So far I have focused on the probability distribution of the observed signal given a target mass and redshift, $P(S^{\rm obs}\,|\,M_{\rm t},\,z_{\rm t})$. However, when dealing with samples selected by observable, it is the inverse, the distribution of target mass given an observed signal $P(M_{\rm t}\,|\,S^{\rm obs},z_{\rm t})$, that is the relevant quantity. Inferring the underlying mass selection is an important common objective for clusters surveys of all wavelengths.

The fast halo sight-lines can be built with a range of target masses, as in § 3.2.1, allowing us to create an ensemble of observed cluster-halo pairs from individual sky patches. We then use these pairs to map out the distributions of underlying halo masses selected by observed signals.

To properly create the simulated survey catalogue, first, I generate sky patches with target masses sampled from a uniform distribution in large quantity. I then process these sky patches and obtain the observed signal $S^{\rm obs}(M_{\rm t},\,z_{\rm t})$ for each target in Optical, SZ, and X-ray. Subsequently, I apply a prior probability $P(M_{\rm t},z_{\rm t})$, which is proportional to the halo mass function, to each patch.

$$P(S^{\rm obs}|z\_rt) = \int_M P(S^{\rm obs}\,|\,M_{\rm t},z_{\rm t})P(M_{\rm t}\,|\,z_{\rm t}), \tag{3.1}$$

in which the prior distribution $P(M_{\rm t}\,|\,z_{\rm t})$ is the dark matter halo mass function at redshift $z_{\rm t}$. It is worth noting that since the mass function itself is not a proper prior (in the sense that it cannot be normalized), a cutoff mass has to be introduced in the actual computation. The results are not significantly affected by such cutoff as I investigate in a $S^{\rm obs}$ much higher than the expected value of the cutoff mass.

In Figure 3.7, I show the product of such simulated catalogue. Densities of the joint $S^{\rm obs}$ - $M_{\rm t}$ distributions are shown in heat maps. In panels on the left, the observed signal is computed with a θ_{200} top-hat filter, whereas the right-hand-side panels use the local Bg-sub filter. The expected intrinsic values with no projections are shown in solid cyan lines,

accompanied by their $\pm 2.5\sigma$ ranges in dashed lines. Systems that lie above the top dashed lines are defined to be "Heavily-Projected" in this model (Eq. 2.21).

The top-hat filtered signals are naturally enhanced relative to the intrinsic values, with SZ at low masses most strongly affected. Local background-subtraction removes the bias caused by projection but introduces additional scatter at the same time.

While theorists may prefer to look at Figure 3.7 this way, observers should see its transposed image in survey data, without a perfect knowledge of the actual $\ln M$. Inferring the underlying mass distribution at fixed $S^{\rm obs}$ is essentially slicing a horizontal piece from Figure 3.7 to obtain $P(M|S^{\rm obs})$.

As illustrated by the green horizontal dashed lines in Figure 3.7, I center on the expected intrinsic signals of a $5\times10^{14}h^{-1}\mathrm{M}_\odot$ and a $1\times10^{14}h^{-1}\mathrm{M}_\odot$ target and select systems whose $S^{\rm obs}$ fall within $\Delta = \pm 10\%$ of them, and plot their distributions in Figure 3.8.

The Probability Density Function (PDF)s as obtained in the simulated catalogue are presented in Figure 3.8 as histograms while their Gaussian fits are shown in solid black lines. The "Heavily Projected" systems are highlighted in red color while the rest are represented by shaded blue. I include the location of both the $M = 5\times10^{14}h^{-1}\mathrm{M}_\odot$ and $M = 1\times10^{14}h^{-1}\mathrm{M}_\odot$ halo on the plot with dashed line for reference. Results here are obtained using the Bg-sub filter as it removes the projection bias which may otherwise shift the PDFs significantly.

Note that the PDFs are not expected to center on the $M = 5\times10^{14}h^{-1}\mathrm{M}_\odot$ and $M = 1\times10^{14}h^{-1}\mathrm{M}_\odot$ dashed-lines. The deviation between the log-mean of the distributions and the target value into the observable-mass scaling relations is the Eddington bias driven by the convolution with a steep mass function, as described analytically in Rozo et al. [2012].

Another key feature in Figure 3.8 is the increase in mass scatter towards smaller clusters. The intrinsic optical signal scatter increases at lower mass due to the nature of Poisson distribution, but the variance in the log- SZ and log- X-ray signals are constant. While X-ray observations are less susceptible to projections and thus exhibit insignificant changes

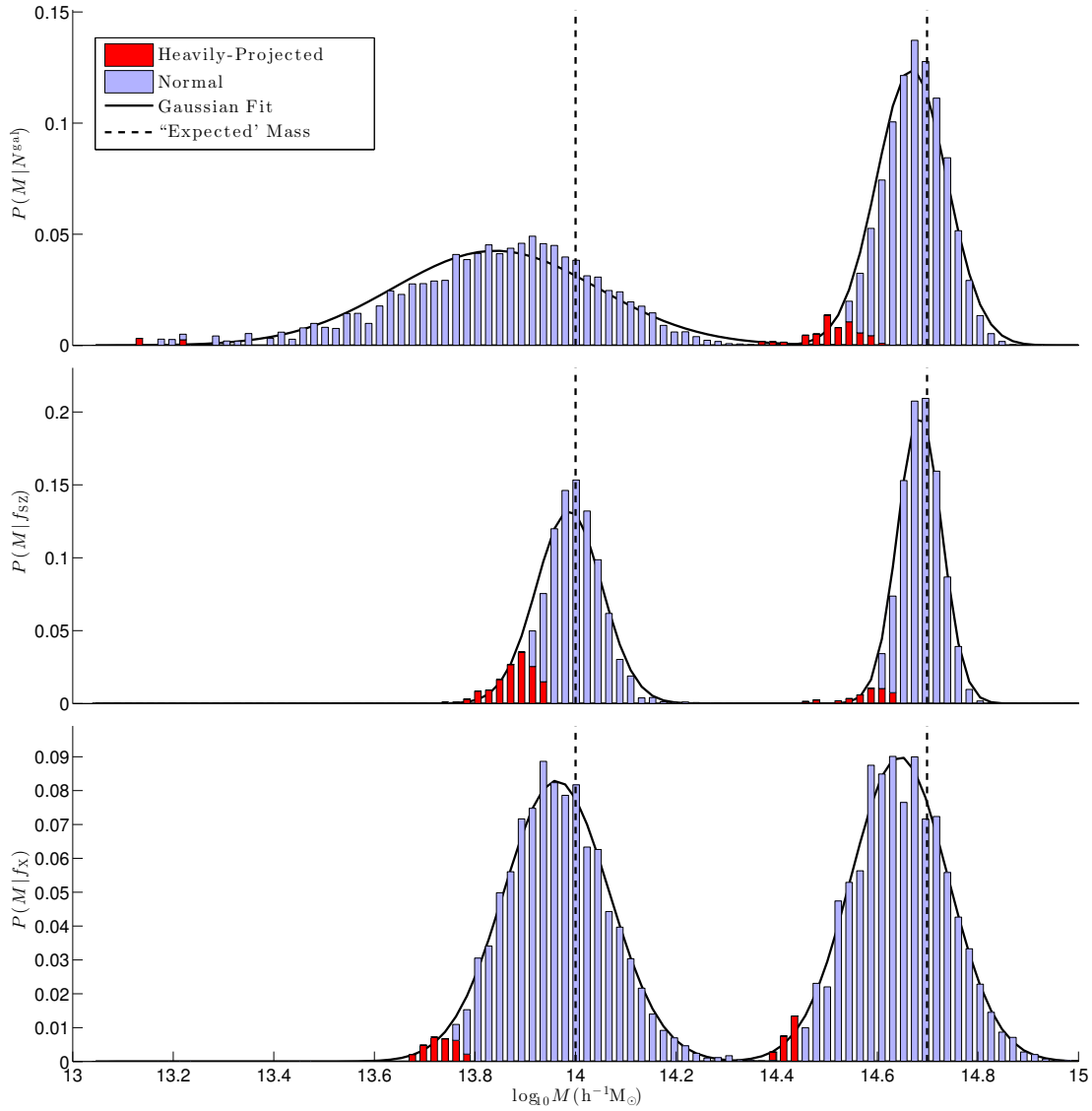

Figure 3.8: Conditional mass likelihood selected by local background subtracted signals at $z_t = 0.3$ in Optical, SZ, and X-ray (top to bottom). Clusters are selected if their observed signal lies within $\pm 10\%$ of the expected value of a $5 \times 10^{14} h^{-1} \mathrm{M}_\odot$ target (on the right) or a smaller, $1 \times 10^{14} h^{-1} \mathrm{M}_\odot$ target (on the left). The parts shaded red represent contributions from the "Heavily-Projected" systems. The solid black curves represent Gaussian fits to the data. Black dashed lines are added to show the mass scales at which I select the observed signals.

in the width of $P(M|S^{\rm obs})$, the inferred mass distribution widens noticeably in SZ as one moves to weaker signals. In optical, such increase in scatter is exacerbated by the increase in Poisson variance.

Additionally, the PDFs deviates form a perfect Gaussian shape, being skewed toward lower masses, especially in the optical. Such non-Gaussianity is driven by the "blended" systems as defined in Cohn et al. [2007], which has been further studied by Erickson et al. [2011].

3.4 Summary and Discussion

In Chapter 2, I presented an semi-analytical projected halo model, which enables the assessment of line-of-sight projections in galaxy clusters. Using a simple Monte Carlo approach, one may generate discrete sight-lines featuring both correlated and random haloes. The method serves as a much faster alternative to N-body simulations in studying galaxy cluster projections with greater statistical power, especially of the massive clusters.

In to assess projections in $S^{\rm obs}$, a simple multi-wavelength signal model is added to the projected halo model, in which intrinsic signals are put in via scaling relations and assigned to the simulated sky patches using proper profiles. $S^{\rm obs}$ was presented with three filtering schemes, top-hat, matched, and background-subtracted.

In Chapter 3, the observed signal bias and variance for a fiducial target of mass $5\times10^{14}h^{-1}{\rm M}_{\odot}$ at $z_{\rm t}=0.3$ in a WMAP7 cosmology have been measured. Optical richness is most susceptible to projection, with a simple, top-hat filtered boost of 16%, compared to 6% and 4% in SZ and X-ray, respectively, for the fiducial target.

Projection in the optical is also more localized in redshift and therefore more dependent on nearby, correlated haloes. Background subtraction removes the signal bias but increases the variance in observed signals. I examined the sensitivity of these effects to target mass and redshift, finding that at $z_{\rm t}=0.3$, the top-hat projected SZ boost exceeds

that in the optical at halo masses below $\sim 10^{13.9} h^{-1} \mathrm{M}_{\odot}$. I further discussed the fraction of "Heavily-Projected" systems in each observable, and examined the shape of the mass selection function at fixed S^{obs}.

CHAPTER 4

Observed Signal Covariance

We live in an era where large surveys at different wavelengths begin to provide abundant statistics of galaxy clusters. In the optical, existing surveys such as the SDSS [Ahn et al., 2012, Stoughton et al., 2002] have provided optical galaxy clusters on the order of 10,000. Up-coming surveys such as the Dark Energy Survey (DES) [Annis et al., 2005, The Dark Energy Survey Collaboration, 2005], the Visible and Infrared Survey Telescope for Astronomy (VISTA) at the European Southern Observatory (ESO) [Saito et al., 2012], *etc.* will add to this pool in statistics and at deeper redshift. In the sub-millimeter wavelength, an increasing number of SZ clusters has been observed by Planck [Planck Collaboration et al., 2011a,b,c], and by the South Pole Telescope (SPT) [Carlstrom et al., 2011] in recent years. In the X-ray, missions like the X-ray Multi-Mirror Mission (XMM-Newton) [Finoguenov et al., 2007, Hasinger et al., 2007], the XMM Cluster Survey (XCS) [Mehrtens et al., 2012], and the eRosita mission [Cappelluti et al., 2011, Pillepich et al., 2012] continue to add to the X-ray cluster pool.

The overlap of survey fields has provided a number of clusters observed in multiple wavelengths. Joint studies between SZ and optical [*e.g.*, Planck Collaboration et al., 2011d], SZ and X-ray [*e.g.*, Planck Collaboration et al., 2012], X-ray and lensing [*e.g.*, Leauthaud et al., 2010, Mahdavi et al., 2013], *etc.* have already emerged in recent years. In the near future, studies on the observable joint distribution of galaxy clusters [*e.g.*, Mantz et al., 2010, Rozo et al., 2009] are expected to come in greater quantity as the number of

clusters observed in multi-wavelengths increases.

Such studies of the observable covariance in cluster signals lead us towards better understanding of the intra-cluster physics and higher accuracy in joint mass estimations. In this chapter I aim at utilizing the projected halo model to understand the various effects on observed signal covariance when line-of-sight projections are introduced.

4.1 Extensions to the Model

Starting from the beginning of the projected halo model, I shall now treat the observed signal, $S^{\rm obs}$ in Eq. 2.1, as a vector, $\boldsymbol{S}^{\rm obs}$, which contains multi-wavelength measurements in the optical, SZ, or X-ray. In this chapter, I shall use a subscript i to represent an observation at a specific wavelength, for example $S^{\rm obs}_{\rm i} = N^{\rm gal}$ when i = *optical*, *etc.*.

4.1.1 The Intrinsic Covariance

It was not until recently did studies of intrinsic signal covariance through gas dynamic simulations began to emerge [*e.g.*, Stanek et al., 2010]. Observational studies, on the other hand, can only provide insights to the observed covariance of $\mathrm{Cov}(S^{\rm obs})$ with the limited number of jointly observed clusters. I shall show later in this chapter, that $\mathrm{Cov}(S^{\rm obs})$ may differ from $\mathrm{Cov}(S^{\rm int})$ due to line-of-sight projections.

Following the formalism in Chapter 2, I first consider modeling the covariance in the intrinsic signal $\Pi(M, z)$ as discussed in § 2.3.1.

I shall mainly discuss two scenarios of the intrinsic covariance matrix, $\mathrm{Cov}(\Pi)$. The first is a zero correlation case, in which correlations between pairs of intrinsic optical, SZ, and X-ray signals are all zeros. The "zero" case provides a perfect starting point for one to see the effects of projections on observed signal covariance. The second scenario is a "typical" intrinsic correlation matrix as shown in Table 4.1, in which the SZ and X-ray components are 78% intrinsically correlated in log-signal, while the optical has a -20%

Table 4.1: The "Typical" Intrinsic Correlation Matrix

	Optical	SZ	X-ray
Optical	1	-0.2	-0.2
SZ	-0.2	1	0.78
X-ray	-0.2	0.78	1

The correlation matrix of the logarithmic intrinsic signals in the optical, SZ, and X-ray. The SZ and X-ray signals follow log-normal distributions with standard deviations of 12% and 40%, respectively. In this case, the optical signal is sampled from a log-normal distribution with a variance equivalent to that of the Poisson distribution. Please refer to § 4.1.2 for more details on this approximation.

correlation to each of them.

The 78% correlation between SZ and X-ray is motivated by the simulation results in Stanek et al. [2010], as their observations both scale with the electron density in the ICM (Equations 1.23 and 1.24).

With respect to the optical - SZ / optical - X-ray correlations, both stripping and feedback processes caused by supernovae winds and black hole jets are mechanisms that lower baryonic matter composition in galaxies and raises gas fraction in the ICM, which could potentially create a negative intrinsic correlation between the optical and X-ray / SZ signals. Unfortunately, there exist no literature to provide a precise quantitative measurement of these correlations. I choose a fiducial value of -20% in both the optical - SZ and the optical - X-ray intrinsic correlations.

4.1.2 Introducing Intrinsic Correlations to the Optical Signals

Common optical galaxy cluster mass proxies such as the cluster richness $N^{\rm gal}$ dictate its distribution to be Poisson at fixed mass, which posses a conundrum for this study when using the "typical" intrinsic correlations in Table 4.1.

Since most target clusters are massive, having sufficiently high optical richnesses (*i.e.*, $N^{\rm gal}_{\rm tar} >> 1$), I use a log-normal approximation of the Poisson distribution to introduce the negative correlation between optical and the other two intrinsic signals.

I find that, when $N > 12$, a log-normal distribution with the following scatter fits the Poisson distribution scatter well,

$$\sigma_{\ln N} = \begin{cases} \exp(0.1 - 0.52 \ln N) & \ln N \geq 2.5 \\ 0.3012 & \ln N < 2.5 \end{cases} . \tag{4.1}$$

I choose not to simply employ the $\frac{1}{\sqrt{N}}$ scatter because it underestimates the Poisson variance in $\ln N$ when N is small, can be seen in Figure 4.1, whereas the fit provided by Eq. 4.1 gives better agreement down to the level of $N \approx 12$. The plot shows the scatter of $\ln N$, when N is drawn from Poisson distributions in blue solid line. The data samples 10,000 independent identically distributed N values for each mean. The red solid line shows the fit using Eq. 4.1 and the solid black line is the canonical $\frac{1}{\sqrt{N}}$ value.

The log-normal approximation of a Poisson distribution becomes poor when $N < 12$, both in terms of the scatter and the asymmetrical shape in the distribution. Thus, the usage of this approximation is limited to the target haloes only, *i.e.*, intrinsic optical signals $\Pi_{\rm opt}$ of the projected haloes are still drawn from the Poisson distribution and will exhibit no correlation with either the SZ or the X-ray signals. It will be shown later in § 4.2.3, that the projection contribution to the observed signal covariance is dominated by cosmic variance, which makes the effect of not including the -20% correlations amongst the projected signals insignificantly.

4.1.3 Inclusion of Halo Mass

In addition to the optical, SZ, and X-ray, I shall include a fourth component in the covariance matrix, the projected mass along the entire line-of-sight. Such measurement may serve as an approximation to lensing mass of galaxy clusters, which essentially measures the abundant mass along the line-of-sight relative to the background density with a weighing function in redshift and angular distance.

Precise modeling of the lensing mass requires decisions about the lensed galaxy popu-

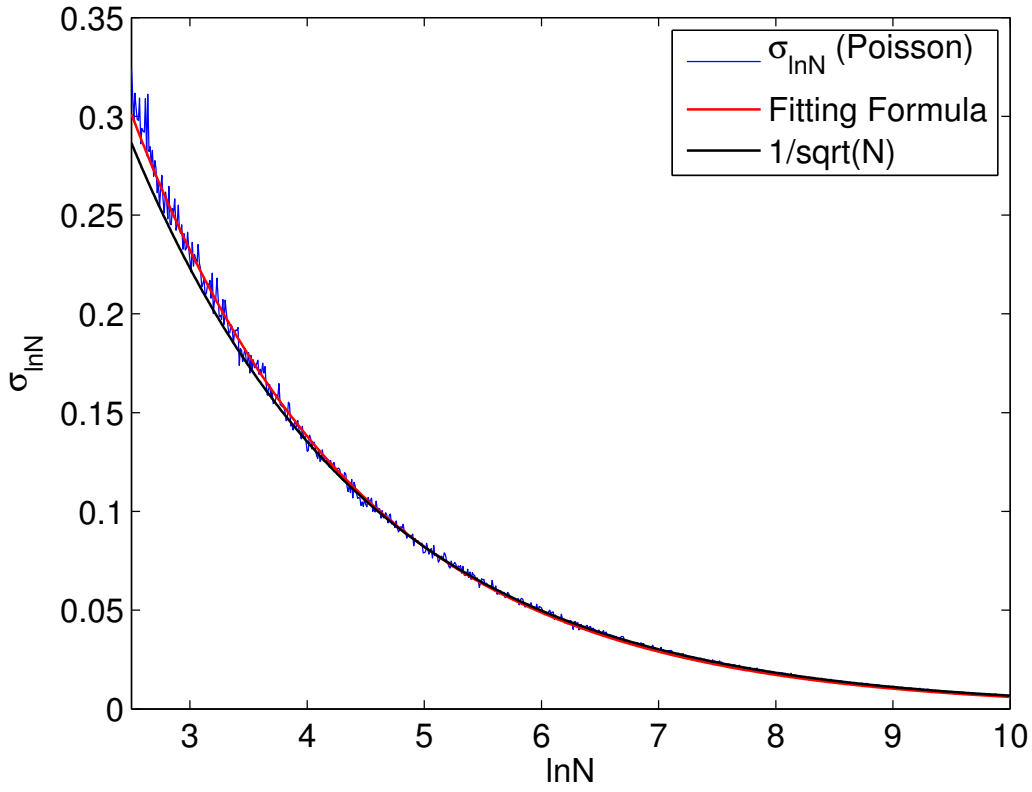

Figure 4.1: The scatter of 10,000 independent identically distributed random variables drawn from the same Poisson distribution for given mean N (in blue) fitted by the log-normal scatter fitting form given in Eq. 4.1 (in red).

lation, a quantity that differs from survey to survey. The typical approach in simulations is to use a multi-plane ray tracing technique and find the projected mass via lensed images.

Since this study is exploratory, I choose to include the projected mass directly as opposed to applying the ray tracing technique to maintain the simplicity of the model. Ultimately, the goal of this study is to make a first attempt of covariance assessment with the presence of line-of-sight projections and the projected halo mass measurement serves this goal well.

4.1.4 Contributions to the Observed Covariance

Within the model of framework, the intrinsic component is independent from the projected one. Obviously the uncorrelated random component should exhibit no correlation to the other components, as there exist no astrophysical process that relates, for instance, the abundance in optical galaxies in one halo to $N^{\rm gal}$ in another one hundreds of Mpc away. However, some models, such as the cooperative galaxy formation model [Bower et al., 1993], have proposed mechanisms in which the correlated component may exhibit weak spatial correlations. I choose to exclude such possible weak cross-correlations in this model because it is a higher order correction, thus enforcing $\mathrm{Cov}(S_{\rm i}^{\rm int}, S_{\rm j}^{\rm proj}) = 0$.

Covariance of the observed signal $S^{\rm obs}$ can be expanded in the following form,

$$\begin{aligned}
&\mathrm{Cov}(S_{\rm i}^{\rm obs}, S_{\rm j}^{\rm obs}) \\
&\quad = \mathrm{Cov}(S_{\rm i}^{\rm int}, S_{\rm j}^{\rm int}) + \mathrm{Cov}(S_{\rm i}^{\rm proj}, S_{\rm j}^{\rm proj}) \\
&\quad = \sigma_{\rm i}^{\rm int}\sigma_{\rm j}^{\rm int}\rho_{\rm ij}^{\rm int} + \sigma_{\rm i}^{\rm proj}\sigma_{\rm j}^{\rm proj}\rho_{\rm ij}^{\rm proj},
\end{aligned} \tag{4.2}$$

in which σ is the the standard deviation in linear S, and subscripts i, j stand for the observed signal at different wavelengths.

Although the intrinsic signals in both SZ and X-ray are assumed to follow log-normal distributions with fixed $\mathrm{Cov}(\ln S_{\rm i}^{\rm int}, \ln S_{\rm j}^{\rm int})$ values, the study will focus on examining $\mathrm{Cov}(S, S)$

instead of $\mathrm{Cov}(\ln S, \ln S)$ henceforth as S represents the physical quantities, *i.e.*, number of galaxies and flux, which add linearly. The additive feature of S allows for the separation of components in Eq. 4.2, making physical interpretations much easier.

4.2 Projection Induced Covariances

With the extensions to the model, I study covariances in S^{obs} via populating haloes in the simulated sight-lines with multivariable signals that are intrinsically correlated as described in § 4.1.1.

Figure 4.2 shows the $\delta \ln S$ - $\delta \ln S$ matrix generated from 30,000 simulated sight-lines on a $M_{\mathrm{t}} = 5 \times 10^{14} h^{-1} \mathrm{M}_{\odot}$, $z_{\mathrm{t}} = 0.3$ target halo with the "typical" intrinsic correlation matrix (Table 4.1). S^{obs}s are obtained using the Bg-sub filter to remove the bias. The diagonal blocks show the distribution of $\ln S_{\mathrm{i}}^{\mathrm{obs}}$ and $\ln S_{\mathrm{i}}^{\mathrm{int}}$ for each observable. In the off-diagonal panels, lower-left contours show the intrinsic $\delta \ln S^{\mathrm{int}}$ - $\delta \ln S^{\mathrm{int}}$ joint distributions, whereas the upper-right ones display the observed joint distributions (the intrinsic halo mass is defined to be M_{t}, thus creating the effect seen in the last row of Figure 4.2).

In following parts of this chapter, I shall extract correlation / covariance information on S^{obs} from the simulated sight-lines as seen in Figure 4.2.

4.2.1 The Zero Intrinsic Correlation Scheme

Covariance of S^{obs} from a projected sight-line standpoint depends on a variety of factors, *e.g.*, the intrinsic correlation, signal variance, filtering scheme, *etc.*. To disentangle the problem, I first start with an perhaps unrealistic but simple scenario by setting the intrinsic correlations to zero and use a simple top-hat filter of the size θ_{200} of the target cluster.

In better reference to the results in Chapter 3, the same benchmark target of $M_{\mathrm{t}} = 5 \times 10^{14} h^{-1} \mathrm{M}_{\odot}$, $z_{\mathrm{t}} = 0.3$ is used here. By creating 30,000 realized light-lines and subsequently convolving the signal sky patch with a θ_{200} top-hat filter, the correlation / covari-

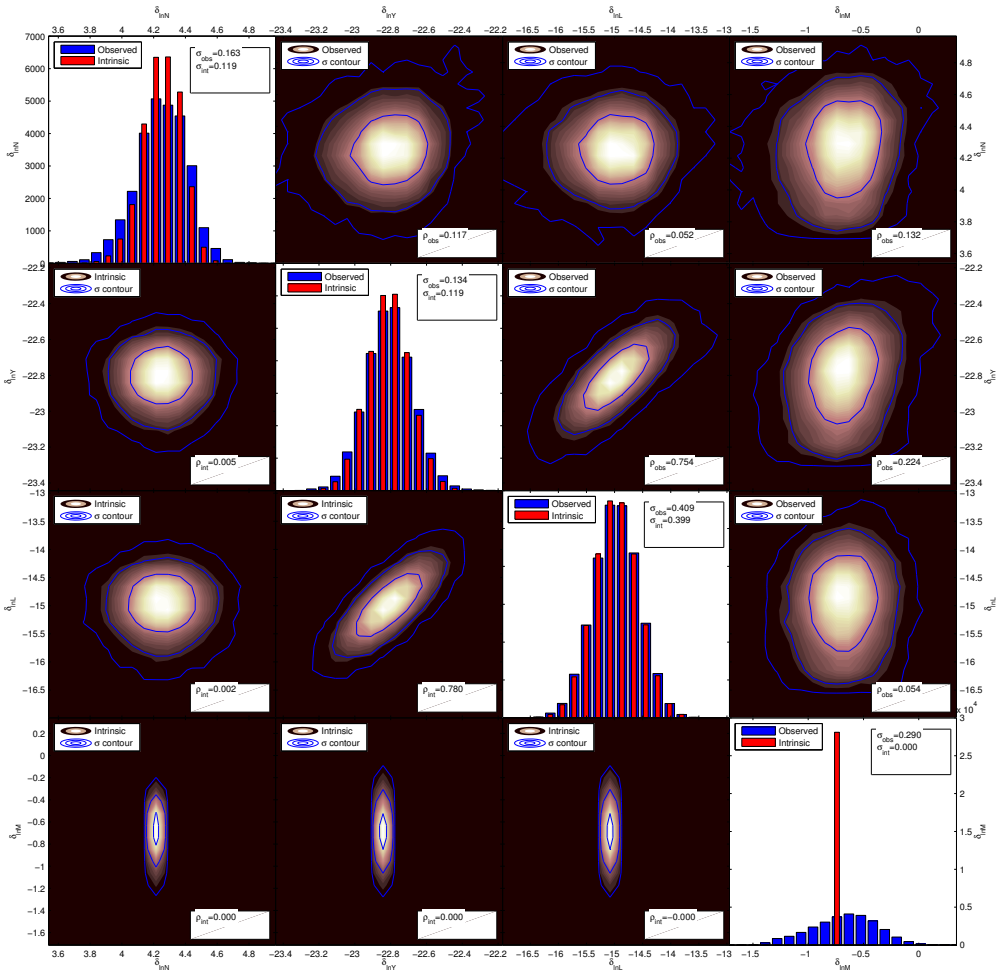

Figure 4.2: Mock optical, SZ, X-ray, and projected mass joint survey result using 30,000 fast halo sight lines simulated with a $M_{\rm t} = 5\times10^{14}h^{-1}{\rm M}_{\odot}$, $z_{\rm t} = 0.3$ target to the depth of $z_{\rm max} = 2$. Observed signals are computed via applying the background-subtracted filter. Histograms on the diagonal show the distributions of $\delta\ln S^{\rm int}$ and $\delta\ln S^{\rm obs}$, the deviations of log-signals about their means, while the lower-left off-diagonal panels display the joint distributions for each intrinsic signals pairs, and the upper-right ones show that for each observed signal pair.

Figure 4.3: I present the correlation / covariance matrix of a $M_{\rm t} = 5 \times 10^{14} h^{-1} {\rm M}_{\odot}, z_{\rm t} = 0.3$ target with no intrinsic correlations amongst signals. The result is computed with 30,000 realizations and the statistical uncertainty of each entry is on the ±0.01 level. The upper-right entries are correlations of the observed signals while the lower-left entries show that of the intrinsic. The values in blue color along the diagonal are the normalized standard deviations, $\sigma(S^{\rm obs}) \,/\, < S^{\rm int} >$.

ance matrix of $S^{\rm obs}$ in obtained and shown in Figure 4.3.

In this figure and similar ones to follow, I display correlations in the intrinsic signal, $\rho(S^{\rm int}_{\rm i}, S^{\rm int}_{\rm j})$, in the lower-left entries of the matrix; and show those of the observed signal, $\rho(S^{\rm obs}_{\rm i}, S^{\rm obs}_{\rm j})$, in the upper-right entries. The scatter in observed signal normalized by its expected log-mean intrinsic value, $\sigma(S^{\rm obs}) \,/\, < S^{\rm int} >$, in each observable, is presented along the diagonal.

As seen in Figure 4.3, there are overall increases in the observed signal variance at each wavelength due to the additional projected component in Eq. 4.2, which have been seen in Chapter 3. In addition to the increase in variance, correlations amongst observed signals

are shown to be positive, despite no intrinsic correlations in the model.

It can be seen from Eq. 4.2 that such positive correlation can only come from a correlated projected signal, if we model ρ_{ij}^{int} to be zero. Amongst the signals, the correlation between the optical and SZ leads at 10%, with a 6% observed correlation between SZ and X-ray and 2% in X-ray and optical to follow. In § 4.2.2, I shall show that the larger observed correlation between the optical and SZ signal is caused by a larger scatter in the projected component of those signals, as opposed to a greater correlation in ρ^{proj}. In fact, Figure 4.4 shows that the largest correlation in the projected signals comes from X-ray and SZ, $\rho^{proj} = 83\%$.

The projected mass exhibits larger induced correlations with the observables in general, due to its $\sim 26\%$ scatter, as seen in the right-most column in Figure 4.3. SZ signals show the strongest correlation with projected mass, at 25%, because it effectively probes the deepest sight-line amongst the three observables (Figure 3.4).

4.2.2 Covariance of the Projected Component

To further reveal details about covariance of the projected component, I investigate the projected signal by itself in Figure 4.4, which shows the correlation / covariance matrix of only the projected signals. Instead of $\rho(S_i^{obs}, S_j^{obs})$, the upper-right entries in the figure show $\rho(S_i^{proj}, S_j^{proj})$, and the diagonal ones are $\sigma(S^{proj}) / < S^{int} >$ instead of $\sigma(S^{obs}) / < S^{int} >$. The target cluster ($M_t = 5 \times 10^{14} h^{-1} M_\odot$, $z_t = 0.3$) and filtering scheme (θ_{200} top-hat) are kept the same with those used to create Figure 4.3.

It can be seen that the projected signals are highly correlated, with ρ^{proj} between SZ and X-ray leading the way at 83%. As previously discussed in § 3.1.2, the two share a very similar trait in terms of the contributions from the different redshift (Figure 3.4). The amplitude of variance in the projected signals is around the 7% level, except for projected mass. The 26% scatter in projected mass essentially characterize the level of mass variance in the sight-line relative to $M_t = 5 \times 10^{14} h^{-1} M_\odot$, hence in this case the scatter of the summed

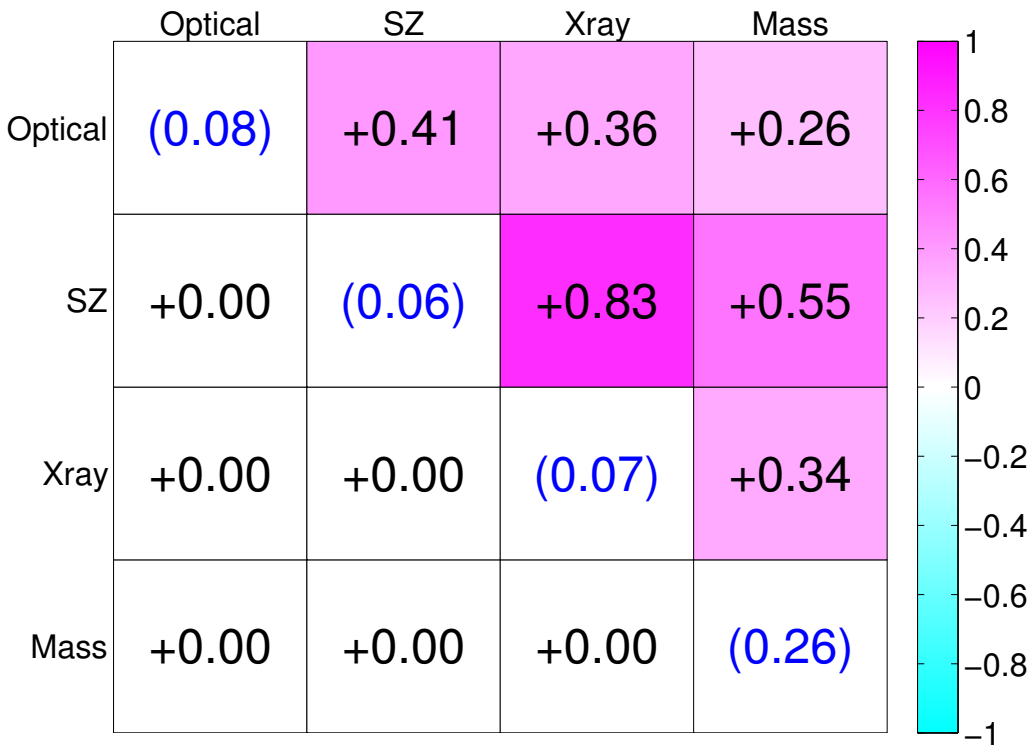

Figure 4.4: Correlation / covariance matrix of the projected signals in sight-lines centered on $M_{\rm t} = 5 \times 10^{14} h^{-1} {\rm M}_{\odot}$, $z_{\rm t} = 0.3$ targets with no intrinsic correlations. The result is computed on 30,000 realizations and the statistical uncertainty of each entry is $\pm \sim 0.01$. See figure 4.3 and text in § 4.2.1 for more details.

projected mass within the θ_{200} aperture has $\sigma(M^{\rm proj}) \sim 0.26 \times (5 \times 10^{14} h^{-1} {\rm M}_{\odot})$.

The correlation between projected mass and projected optical signal is seen to be the smallest in Figure 4.4, since projected optical signals are extremely localized (Figure 3.4) in this model, whereas projected mass simply sums masses from all redshift with an even weight. Nonetheless, $\rho^{\rm proj}$ between the optical and projected mass is still shown to be very significant, at 26%, which, I argue, is likely driven by cosmic variance.

4.2.3 Cosmic Variance

In this model framework, covariances introduced by projections come from mainly two sources, the covariances in the projected signals, and cosmic variance *i.e.*, covariances due to the spatial arrangement of haloes in each line-of-sight. Obviously clusters that reside in densely populated sight-lines should have higher $S^{\rm obs}$ compared to those residing in cleaner environments. This effect, by itself, will introduce an extra piece of variance as well as correlation to the intrinsic covariances.

Since correlations in the intrinsic signals are kept to be zeros, most of the correlations seen in Figure 4.4 should come from cosmic variance. To examine the amplitude of covariance introduced by cosmic variance, I present an idealized situation, in which all randomness from other components are turned off, *i.e.*, every halo contributes a signal equaling to exactly its expected value, making cosmic variance the only remaining source of uncertainty.

Results in Figure 4.5 show that cosmic variance is the dominant factor in the projected covariance seen in Figure 4.4. The amount of scatter introduced by cosmic variance is $\sim$ 5 - 6% in $\sigma_{\ln S}$, and the correlations are almost uniformly higher than those in the projected signals in § 4.2.2. Despite localized in redshift, the optical signal correlates with projected mass in the entire line-of-sight at 31%, due to the fluctuations in the number and masses of haloes in the correlated structure. On the other hand, the similar redshift dependency in SZ and X-ray signals yields the highest correlation of 87% due to cosmic variance.

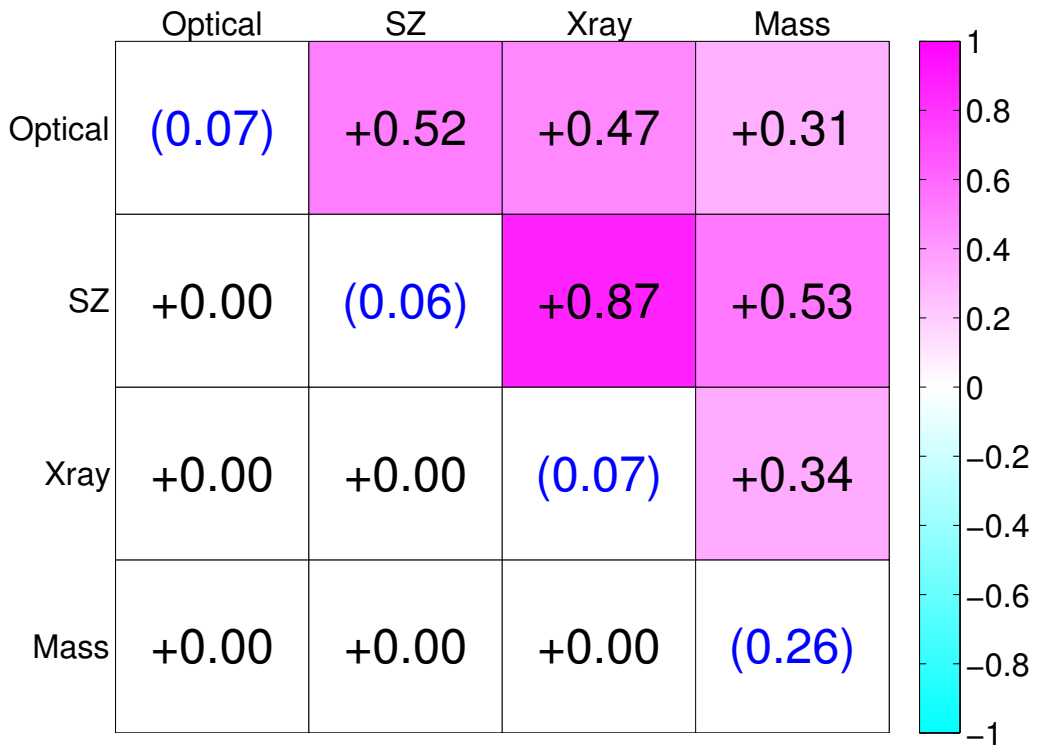

Figure 4.5: Correlation / covariance matrix in the Cosmic Variance only scenario. The result is computed on 30,000 realizations and the statistical uncertainty of each entry is $\pm \sim 0.01$. The target haloes in these sight-lines are still $M_{\rm t} = 5 \times 10^{14} h^{-1} {\rm M}_{\odot}$, $z_{\rm t} = 0.3$. See figure 4.3 and text in § 4.2.1 for more details.

The result here also justifies not including corrections between optical and SZ / X-ray in the projected haloes, as discussed in § 4.1.2.

4.3 Distortions to the Intrinsic Covariance

Moving on from the idealized scenario in which signals are intrinsically independent, I shall now investigate the effect of projections on a given intrinsic covariance. In this section, the "typical" intrinsic correlation matrix in Table 4.1 is used to examine the influence on $\mathrm{Cov}(S^{\mathrm{obs}})$ by the line-of-sight projections. For easier reference, the same target halo with $M_{\mathrm{t}} = 5\times10^{14}h^{-1}\mathrm{M}_{\odot}$, $z_{\mathrm{t}} = 0.3$ and the θ_{200} top-hat filter are used. Figure 4.3 shows the correlation / covariance matrix of S^{obs} for such a target cluster with 30,000 realizations.

In the "typical" scheme, the -20% intrinsic correlation between the optical and SZ signals is much reduced to only -3% when projections are included, echoing the results in § 4.2, which saw a positive correlation introduced by projections. In essence, the negative ρ^{int} in Eq. 4.2 is counteracted by the positive ρ^{proj}, with the final balance in ρ^{obs} determined by the scatter in those signals.

Hence, the -20% intrinsic correlation between the optical and SZ signals is more severely distorted to -3%, compared with a -11% correlation between observed signals in Optical and X-ray, as the projection contribution is larger in SZ than in X-ray, which can be seen either directly in Table 3.3, or indirectly from Figure 4.3.

The observed correlation between SZ and X-ray signals remains strong at 73%, compared to its intrinsic value of 76% in linear signals. As discussed in § 4.2.2, the projected SZ and X-ray signals establish a strong correlation ($> 80\%$) due to similar redshift dependency, hence it is expected that the observed correlation does not differ much from its high intrinsic value.

Findings here answer an important question, if the intrinsic signals are negatively correlated in optical - SZ or optical - X-ray due to reasons explained in § 4.1.1, observational

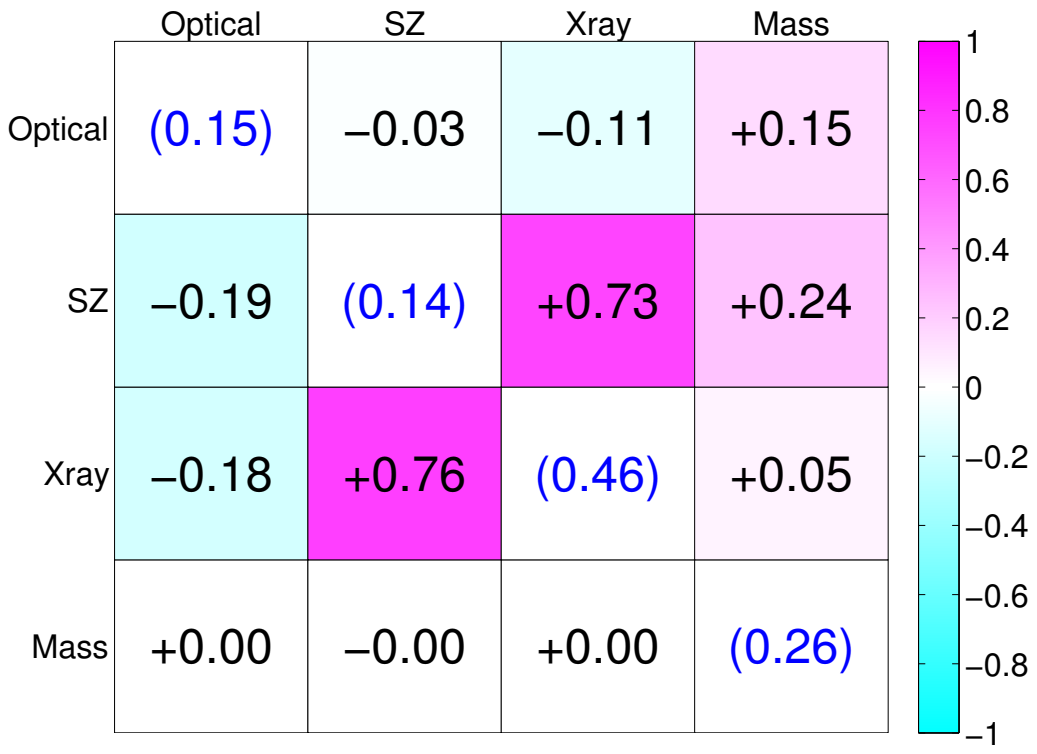

Figure 4.6: Correlation / covariance matrix of $S^{\rm obs}$ when the target halo has $M_{\rm t} = 5\times10^{14}h^{-1}{\rm M}_{\odot}, z_{\rm t} = 0.3$ and the "typical" intrinsic correlations in Tab. 4.1. The result is computed on 30,000 realizations and the statistical uncertainty of each entry is $\pm \sim 0.01$. See figure 4.3 and text in § 4.2.1 for more details.

studies on jointly resolved clusters in multi-wavelength surveys may see a much reduced value due to line-of-sight projections. In fact, the various idealizations made in this model tend to underestimate the projection-induced covariance. Uncertainties in locating the cluster centers, especially in the optical, and subsequently determining the correct θ_{200} size, will introduce additional variances to the problem. If such variances are uncorrelated, *i.e.*, if one expects, for example, mis-centering in the optical not to correlate with measurements in the X-ray, the actual $\rho(S_{\rm i}^{\rm obs}, S_{\rm j}^{\rm obs})$ from observations may lie even further from its intrinsic -20%.

4.4 Covariances at Higher Redshifts

As future surveys such as the DES [Annis et al., 2005, The Dark Energy Survey Collaboration, 2005], XCS [Mehrtens et al., 2012], *etc.* move to deeper redshift, it is important to understand how $\mathrm{Cov}(S^{\rm obs})$ of clusters are affected by projections at redshifts beyond 0.3.

Figure 4.7 shows the correlation / covariance matrix of $S^{\rm obs}$ for a $M_{\rm t} = 4.38 \times 10^{14} h^{-1} \mathrm{M}_{\odot}$ target halo at $z_{\rm t} = 0.7$, under the top-hat filter scheme with no intrinsic correlations (top panel) versus the "typical" intrinsic correlations in Table 4.1. The target mass here is derived from matching the sky surface density of the benchmark $M_{\rm t} = halo514$, $z_{\rm t} = 0.3$ target. For more details on the abundance matching scheme, refer to Appendix C.

Compared to the results at $z_{\rm t} = 0.3$, the observed covariance, $\mathrm{Cov}(S^{\rm obs})$, $z = 0.7$ shows similar effects from projections, but at a reduced level.

For instance, in the zero intrinsic correlation scenario (top-panel of Figure 4.7), the correlation between the observed signals in Optical and SZ stands at 6%, compared to 10% at $z_{\rm t} = 0.3$. The scaled down projection induced correlation here, as well as between SZ and X-ray, are direct consequences of the reduced projection fraction resulting from the smaller $\pi\theta_{200}$ sky area, as explained in § 3.2.2, as one moves to higher redshift. This effect is heavily compensated by the rapid decline in intrinsic flux in X-ray signal, as it scales

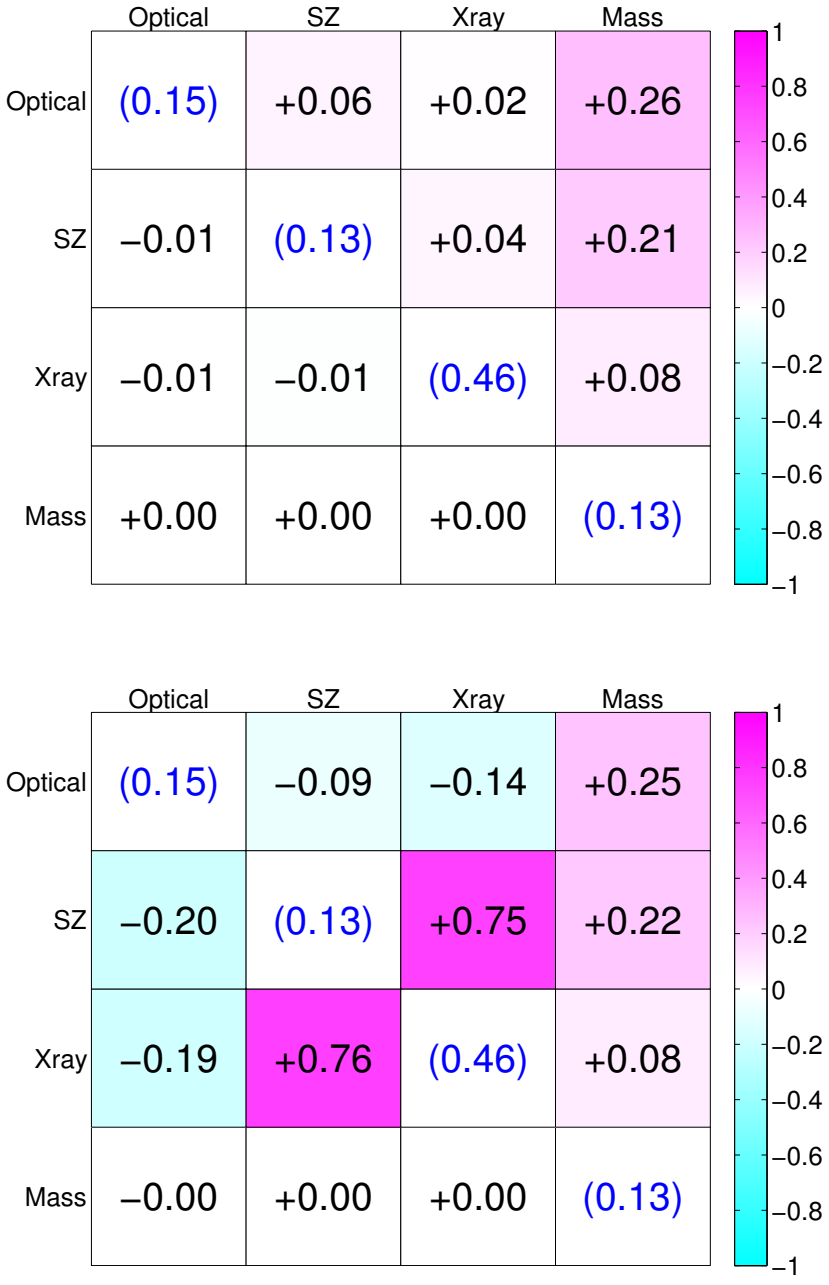

Figure 4.7: Correlation / covariance matrix of $S^{\rm obs}$ when the $M_{\rm t} = 4.38 \times 10^{14} h^{-1} {\rm M}_{\odot}$ is at $z_{\rm t} = 0.7$. In the top panel, a "zero" intrinsic correlation is assumed, while in the bottom one, I use the "typical" intrinsic correlations. See figure 4.3 and text in § 4.2.1 for more details.

with luminosity distance (Eq. 2.9) as opposed to angular diameter distance in SZ (Eq. 2.8).

Similarly, with the "typical" intrinsic correlations (bottom-panel of Figure 4.7), the distortions due to projections are also reduced, yielding a -9% observed correlation between Optical and SZ, and -14% between Optical and X-ray, compared to -3% and -10% in Figure 4.3 when $z_t = 0.3$. Therefore, if the optical signal does exhibit negative intrinsic correlations to SZ and X-ray, they should be easier to observe at higher redshifts as a consequence of the reduced line-of-sight projections.

On the other hand, the observed correlation between Optical and projected mass is increased to 26% at $z = 0.7$, compared to only 14% at $z = 0.3$. It can be seen in Figure A.1 in Appendix A, that the correlated component occupies a greater fraction of the optical projection as one moves to higher redshift. Such an increase in the correlation fraction, exacerbated by the larger bias of a $M_t = 4.38 \times 10^{14} h^{-1} M_\odot$ halo at $z_t = 0.7$, causes the increase in the observed Optical - Mass correlation.

4.5 Discussions

The studies in this chapter provide several important insights to cluster signal covariance.

First, the model shows that the projected signal contributions are positively correlated by nature, mainly due to cosmic variance, uncertainties in the spatial displacement of haloes along the sight-line. The scatter in $S^{\rm obs}$ due to cosmic variance is measured to be between 6 and 7 percent in Optical, SZ, and X-ray. The projection-induced correlations is measured to be 10% or less amongst the observables for a target halo of $M_t = halo514$, $z_t = 0.3$.

In addition, the model shows that a negative intrinsic correlation in the optical with either SZ or X-ray is reduced when projections are included, suggesting that uncovering negative intrinsic correlations at the -20% level between Optical and SZ / X-ray may be difficult in observation. Furthermore, the projection effects on signal covariances are reduced at higher redshifts, particularly in the SZ, as a result of the reduced fractional pro-

jection seen in § 3.2.2.

The study here is aimed at providing an exploratory investigation on the signal covariance of galaxy clusters in multi-wavelength surveys. Findings in this chapter may provide guidance to future analyses of the current and up-coming joint surveys, *e.g.*, the DES, the XCS, and Planck, as well as existing studies [*e.g.*, Mantz et al., 2010, Rozo et al., 2009] on the observed signal covariance for clusters.

CHAPTER 5

Modeling Optical Galaxies and Their Velocity Dispersion

In this chapter, I narrow my focus to the optical wavelength and discuss how I model the optical galaxy clusters, in terms of the HOD and a color model, to the SDSS galaxy catalogue [Adelman-McCarthy et al., 2008, Ahn et al., 2012], in an attempt to use the projected halo model and recreate the stacked galaxy velocity dispersion measurement in optical richness bins in SDSS clusters by Becker et al. [2007].

5.1 The Sloan Digital Sky Survey

The SDSS is a deep, multi-band optical survey over more than a quarter of the sky with $\sim$ one million galaxies after eight years of operations in its two phases [Ahn et al., 2012, Stoughton et al., 2002]. Its enormous catalogue of optical galaxies and the subsequent galaxy clusters between redshift $0.1 \sim 0.3$ [Hao et al., 2010, Koester et al., 2007a] had led to a number of HOD [Abazajian et al., 2005, Coupon et al., 2012, Tinker et al., 2012, Zehavi et al., 2011] and color models [Guo et al., 2013, Zehavi et al., 2011] to describe the galaxy population.

The most relevant components relating to the Becker et al. [2007] velocity dispersion study are the Sloan Digital Sky Survey 7th Data Release (SDSS-DR7) spectroscopic data [Abazajian et al., 2009b] and the MaxBCG galaxy cluster catalogue [Koester et al., 2007a].

Amongst the > 100 million galaxies with 5-band photometry in the SDSS main sample, only ∼ one million were followed-up with spectroscopy. The spectroscopic sub-set is designed to be complete for galaxies brighter than an R-band apparent magnitude 17.76, except when the galaxies are too close to each other to insert optical fibers for both. Such an event is described as "fibre collision" and the level of incompleteness in the spectroscopic sample due to it is estimated to be ∼ 10% [Abazajian et al., 2009b].

The MaxBCG catalogue [Koester et al., 2007a] is a red-sequence galaxy cluster catalogue with 13823 resolved clusters found in the SDSS main sample using an algorithm, which assumes that there is always a Brightest Central Galaxy (BCG) in the centre of a cluster and subsequently looks for galaxies that are most likely to be BCGs at each redshift [Koester et al., 2007b]. The algorithm then tries to estimate the θ_{200} size of the cluster from the location of the BCG and count the number of galaxies within the aperture that fall into the corresponding color range. This galaxy count, $N^{\rm gal}$, is often referred to as the richness of the cluster.

5.2 Velocity Dispersion in SDSS Galaxy Clusters

Evrard et al. [2008] studied virialized haloes in an ensemble of simulations to show that dark matter velocity dispersion forms a power law relationship to halo mass,

$$\sigma_{\rm DM}(M,z) = \sigma_{\rm DM,15}(\frac{M}{10^{15}h^{-1}{\rm M}_\odot})^\alpha, \tag{5.1}$$

in which the logarithmic slope, α, is found to be $\sim 1/3$ with an intercept $\sigma_{\rm DM,15} = 1083{\rm kms}^{-1}$. In addition, the log-scatter in this power-law relation, $\sigma_{\ln\sigma}$, was measured to be 4.3%.

Becker et al. [2007] measured the observed galaxy velocity dispersion in the MaxBCG clusters, via computing $c\delta z$ for every galaxy with spectroscopy in the vicinity of a BCG and subsequently stacking the signals into four richness bins to create the histograms seen in Figure 5.1. The log-scatter in the radial velocity dispersion, $c\delta z$, is shown to increase

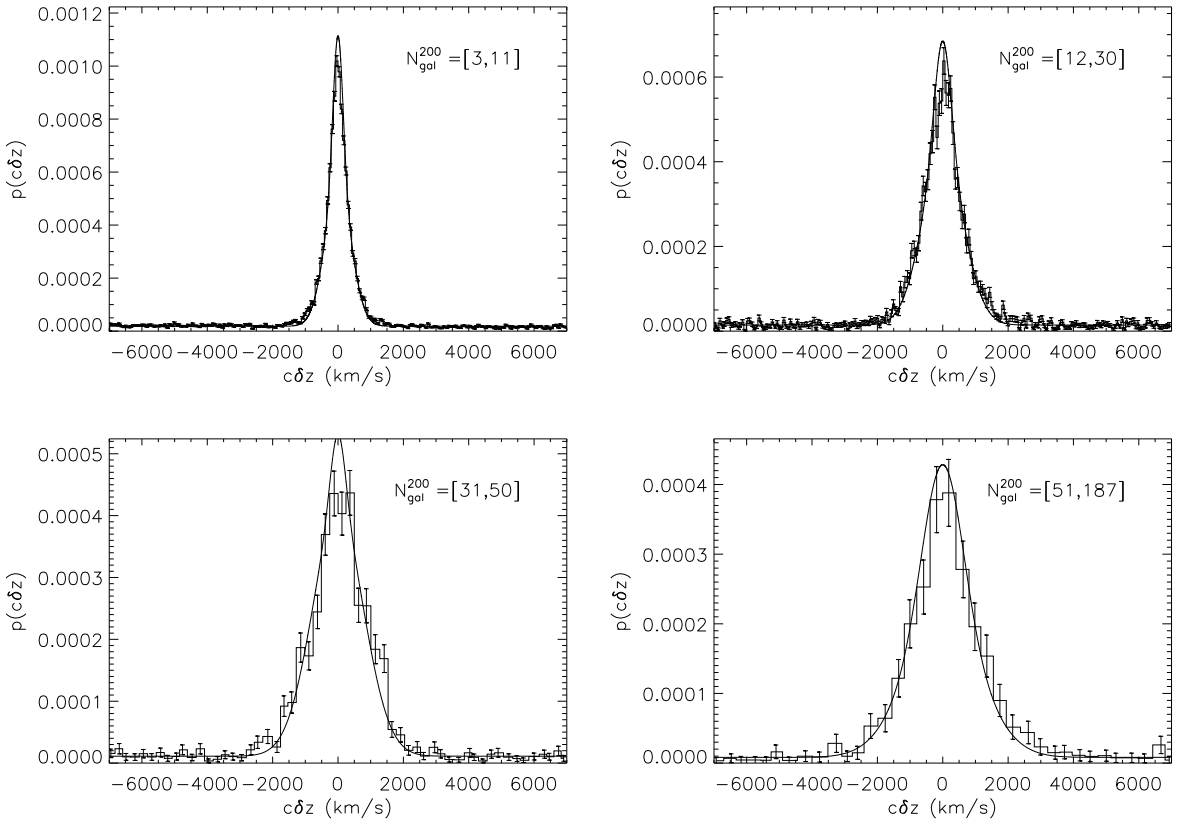

Figure 5.1: The pairwise velocity difference histograms stacked in four richness bins of the MaxBCG cluster catalogue in Becker *et al.*, 2008.

from $\sim 15\%$ when $N^{\rm gal} \approx 88$ to 40% at $N^{\rm gal} \approx 10$.

Though measuring similar properties, the 4.3% scatter as measured by Evrard et al. [2008] is the scatter at fixed mass, while Becker et al. [2007] measures the log-scatter in radial velocity at fixed richness, which contributes significantly towards the $\sigma_{\ln\sigma}$ measurement, especially at the low richness end.

The stacked radial velocity dispersion measurement made in Becker et al. [2007] can be used to test the projected halo model in observation, as it captures the correlated structure in both the foreground and background of a cluster. Using the projected halo to reproduce the observed histograms in Figure 5.1 can provide observational verification of the model and improve our understanding of the observed scatters in galaxy velocity dispersion.

To use the Projected Halo Model, two components in addition to Eq. 5.1 are needed to

simulate the observed velocity dispersion. One is the mass-richness relation of MaxBCG clusters and the other is the likelihood function of each member to have spectroscopic follow-up in the SDSS, *i.e.*, $m_R < 17.76$. While Johnston et al. [2007] provided a good mass-richness study using weak lensing measurements, the latter component does require an HOD model based on the SDSS R-band magnitude.

5.3 The HOD Model

Traditionally, the HOD contains two components, the number of galaxies above some threshold luminosity / magnitude limit in a given halo; and the spatial distribution of these galaxies. Since only the first component, *i.e.*, the number density, is relevant for the purpose of this study, I shall omit the spatial distribution in my HOD model.

Studies have shown that central and satellite galaxies have distinct features in many physical properties, *e.g.*, the central ones are usually brighter and redder than their counterparts [*e.g.*, Hao et al., 2009, Loh et al., 2008]. In consistency with the MaxBCG algorithm, I follow the two-component treatment and demand that the central galaxy be brighter than any other member in the cluster.

$$N^{\rm gal}(M_r, M, z) = N^{\rm gal}_{\rm cen}(M_r, M, z) + N^{\rm gal}_{\rm sat}(M_r, M, z), \tag{5.2}$$

in which $N^{\rm gal}(M_r, M, z)$ is the number of galaxies brighter than absolute magnitude M_r [1] residing in a halo with mass M and redshift z and subscript cen and sat represent its central and satellite components, respectively. An illustration of such a two-component model can be seen in Figure 5.2.

By definition, the expected value of $N^{\rm gal}_{\rm cen}$ of an halo should lie between 0 and 1. Inspired by previous works [Brown et al., 2008, Zheng et al., 2005, 2009], I model this expection

[1] Since the symbol M has been assigned to denote halo mass, I shall refrain from using it as the convention for absolute magnitude. Instead, in places of absolute magnitudes, I use the R-band magnitude, M_r, directly. It is worth noting that the HOD formalism presented here is generic and can be applied to any other band.

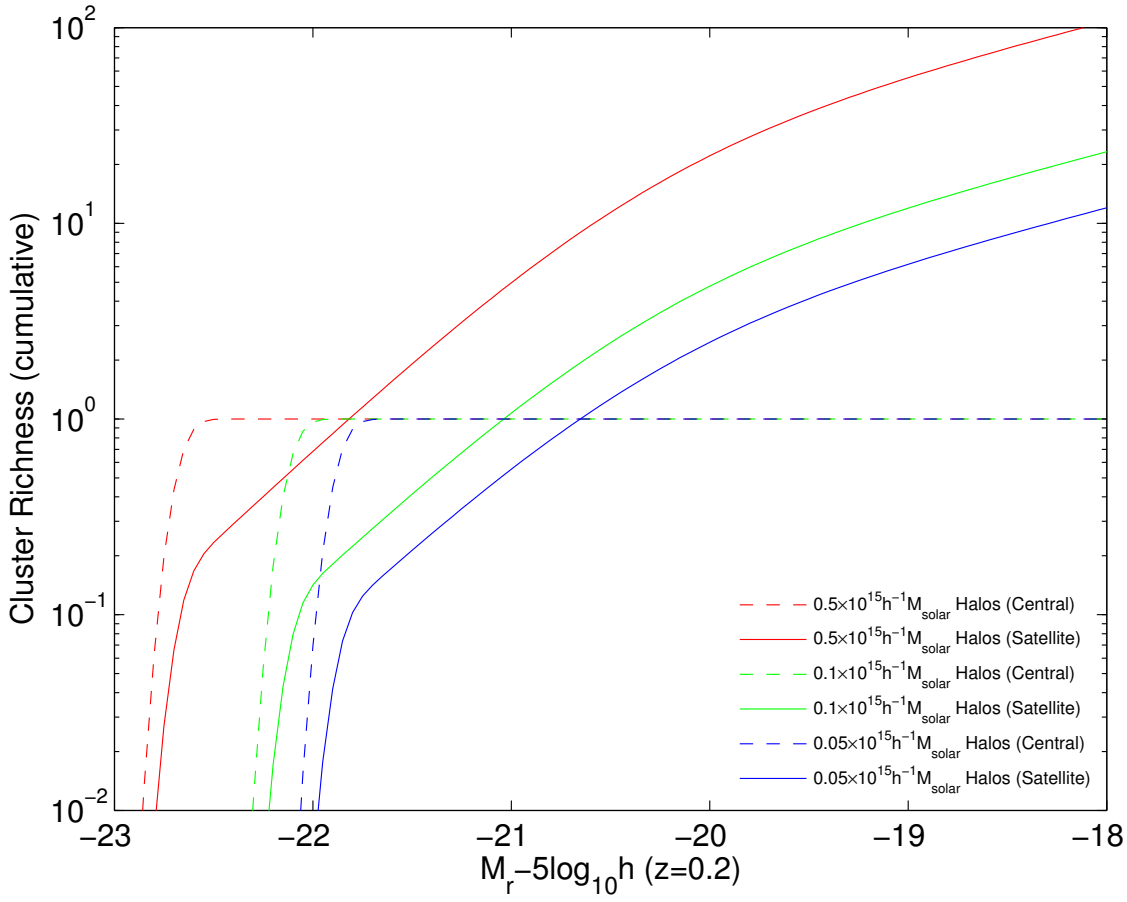

Figure 5.2: The luminosity function of galaxies in haloes with mass $5\times10^{14}h^{-1}\mathrm{M}_{\odot}$, $1\times10^{14}h^{-1}\mathrm{M}_{\odot}$ and $5\times10^{13}h^{-1}\mathrm{M}_{\odot}$, broken down into central and satellite components, according to the suggested HOD parameter values in Table.5.1.

value with an error function.

$$< N_{\rm cen}^{\rm gal} > (M_r, M, z) = \frac{1}{2} + \frac{1}{2}{\rm erf}(\frac{\ln M - \ln M_{\rm min}(M_r, z)}{\sigma_{\ln M}}), \tag{5.3}$$

in which $M_{\rm min}(M_r, z)$ is the minimal mass above which, roughly speaking, a halo is expected to host a central galaxy brighter than M_r. The parameter $\sigma_{\ln M}$ controls the scatter in $\ln M$ for any given magnitude of the central galaxy.

Results of N-body simulations have found that the number of sub-haloes follows a power law relationship to the halo mass with a slope close to 1. Since satellite galaxies are formed in the centers of these sub-clumps, their number density is expected to exhibit similar relations. Observational studies such as Johnston et al. [2007] have provided evidences towards such claim. Hence, I model the expected number of satellite galaxies as the following,

$$< N_{\rm sat}^{\rm gal} > (M_r, M, z) =< N_{\rm cen}^{\rm gal} > (M_r, M, z)(\frac{M}{M_{\rm s}(M_r, z)})^{\alpha}, \tag{5.4}$$

in which $M_s(M_r, z)$ is the scaling mass, at which a halo is expected to host a second galaxy brighter than M_r. The $< N_{\rm cen}^{\rm gal} > (M_r, M, z)$ term ensures that Haloes cannot have satellite galaxies without a central one.

The quantities $M_{\rm min}(M_r, z)$ and $M_s(M_r, z)$ are observed to have different slopes at the bright and faint end of the absolute magnitude axis [Brown et al., 2008, Zehavi et al., 2011, Zheng et al., 2007], therefore, I parameterize them using a broken power law,

$$M_{\rm min}(M_r, z) = (1+z)^{\beta}\{\exp[\mu_1(M_r - M_r{}^{\star}) + \ln M_{\rm min}^{\star}] + \exp[\mu_2(M_r - M_r{}^{\star}) + \ln M_{\rm min}^{\star}]\}, \tag{5.5}$$

in which $(1+z)^{\beta}$ is the redshift evolution term, $M_r{}^{\star}$ is the turnover magnitude in the broken power law, $M_{\rm min}^{\star}$ is approximately the minimal mass at $M_r{}^{\star}$ and redshift of 0, $M_{\rm min}(M_r{}^{\star}, 0)$, and μ_1 & μ_2 are the two slopes, respectively.

Table 5.1: Fitted Values of the HOD Parameters

Parameter	Best-fit Value	σ
α	0.9519	0.0125
β	2.4518	0.0690
$M_{r\star}$	-20.297	0.0119
$\sigma_{\ln M}$	0.3	N/A
μ_1	-0.2814	0.0208
μ_2	-2.5816	0.0267
$\ln M^{\star}_{\rm min}$	-6.8984	0.0858
ν_1	-0.5204	0.0129
ν_2	-2.1417	0.0309
$\ln M^{\star}_{\rm s}$	-6.2093	0.0717

The best-fit values and 1σ uncertainties of the HOD model parameters in Eq. 5.2 through 5.6 constrained by MCMC. I fixed the value of $\sigma_{\ln M}$ to 0.3 because the SDSS-DR7 data, to which I fit this HOD model, is not sensitive to its value.

And similarly for the scaling mass,

$$M_{\rm s}(M_r, z) = (1+z)^{\beta}\{\exp[\nu_1(M_r - M_r{}^{\star}) + \ln M^{\star}_{\rm s}] + \exp[\nu_2(M_r - M_r{}^{\star}) + \ln M^{\star}_{\rm s}]\}, \qquad (5.6)$$

in which $M^{\star}_{\rm s}$ is approximately the scaling mass at $M_r{}^{\star}$ and redshift of 0, $M_{\rm s}(M_r{}^{\star}, 0)$.

It is worth noting that through the parameterization in Eq. 5.5 and Eq. 5.6, I have implicitly assumed the same redshift revolution for $M_{\rm min}$ and $M_{\rm s}$, as well as a common characteristic magnitude, $M_r{}^{\star}$.

Thus, the HOD model has α, $\sigma_{\ln M}$, β, $M_r{}^{\star}$, $\ln M^{\star}_{\rm min}$, $\ln M^{\star}_{\rm s}$, μ_1, μ_2, ν_1 and ν_2, in total 10 parameters. I constrained values of these parameters by fitting the observed R-band distribution of galaxies in the SDSS-DR7 main sample [Abazajian et al., 2009a], and in the spectroscopic subset with redshifts, using an Markov Chain Monte Carlo (MCMC) approach.

I list the best-fit HOD parameter values in Table 5.1 with their 1σ uncertainties suggested by Markov chains. The HOD model's goodness of fit to the SDSS-DR7 spectroscopic data can be seen in Figure 5.3, in which the observed galaxy number density in the magnitude - redshift plane is plotted in noisy contours, whereas the prediction made by the

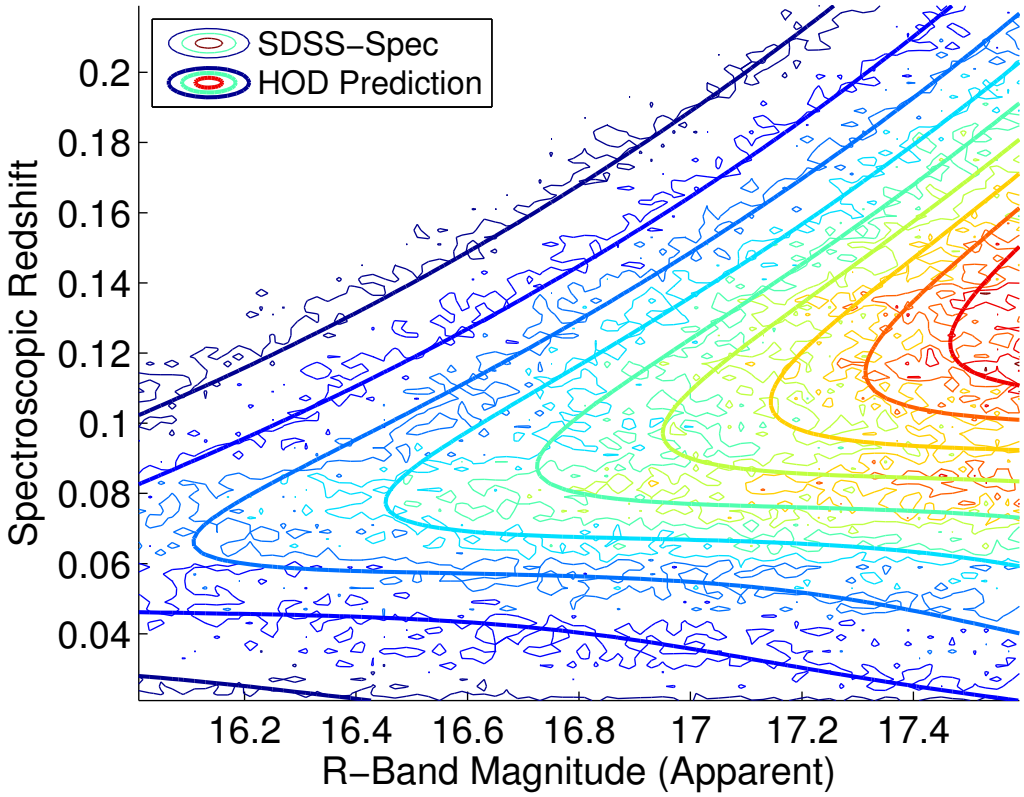

Figure 5.3: The contour plot indicates galaxy density in the magnitude-redshift space as observed in SDSS (shown in noisy thin contour lines) and that predicted by the empirical HOD model with parameters suggested by Table 5.1 (shown in thick colored lines).

HOD model is painted in solid lines.

I use a fiducial value of 0.3 for $\sigma_{\ln M}$ because the observational data, *i.e.*, the SDSS main sample and the spectroscopic subset, are very insensitive to this value. More details of fitting the SDSS-DR7 result using MCMC can be found in Appendix E.

The HOD model by itself cannot used to predict the MaxBCG richness of haloes, as the latter one measures only the red-sequence galaxy fraction of the total population. For this purpose, an additional piece to describe the colors of these galaxies is necessary in the model.

5.4 The Color Model

Galaxy color obtained by multi-band photometry can be processed to provide photometric redshift estimation or used directly as a proxy to redshift, particularly for the red-sequence galaxies. The color of a galaxy observed using multi-band photometry is defined as the differences in magnitude (or equivalently the ratio between fluxes) as received between filter bands.

The SDSS five-band photometry (G, R, I, Z, and Y) yield 4 such colors, of which $G-R$, $R-I$, and $I-Z$ are frequently used from low to high redshifts. Since the 4000 angstrom break shifts redder on observed spectra as redshift increases, $G-R$ color is primarily used at low redshift in the SDSS as a redshift proxy, while $R-I$ and $I-Z$ colors become useful beyond $z \approx 0.35$. For the purpose of this study, I shall focus on $G-R$ in the color model in coherence with the MaxBCG catalogue.

Analyses of the SDSS red-sequence galaxy color have shown that the mean $G-R$ increases almost linearly with z until $z \approx 0.35$, at which point the evolution becomes almost flat, until it begin increasing again around $z = 0.6$ [Hao et al., 2009].

Thus I model the SDSS galaxy $G-R$ color in the red and blue populations (denoted by

subscripts r and b, respectively) using simple / piecewise linear models:

$$< G-R >_r (z) = \begin{cases} a_r z + c_r, & z \leq 0.35 \\ a_r'(z-0.35) + c_{0.35}, & 0.35 < z \leq 0.6 \\ a_r''(z-0.6) + c_{0.6}, & z > 0.6 \end{cases} , \tag{5.7}$$

$$\sigma_r^{G-R}(z) = b_r z + d_r, \tag{5.8}$$

$$< G-R >_b (z) = a_b z + c_b \tag{5.9}$$

$$\sigma_b^{G-R}(z) = b_b z + d_b \tag{5.10}$$

in which a is the gradient of the expected $< G-R >$ color against redshift z, b denotes the slope in the scatter's redshift evolution. The constant term $c_{0.35}$ and $c_{0.6}$ are the respective values of $< G-R >_r$ at each turning point, which is determined by the value in the previous segment as I enforce continuity in the model.

The two-population prescription requires a red galaxy fraction (red-fraction) to be defined. While few observational studies of this fraction exists for the fainter galaxies, the red-fraction should depends on galaxy luminosity with its value bounded between 0 and 1.

Therefore, the simplest model would be a linear model of magnitude bounded by lower and upper limits of 0 and 1,

$$f_r(M_r) = \max\{\min[0\,, \frac{1}{2} + s_f(M_r - {M_r}^c)]\,, 1\} \tag{5.11}$$

in which ${M_r}^c$ is the R-band absolute magnitude at which half of the galaxies are red, and s_f is the slope of $f_r(M_r)$.

I constrained the model parameters in Eq. 5.7 through 5.11 via an MCMC approach, which attempts to fit the model to the joint color-magnitude distribution (Figure 5.4) of the SDSS-DR7 main galaxy sample and the spectroscopic subset.

In Table 5.2, I list the best-fit model parameter values with their 1σ uncertainties suggested by Markov chains. The goodness of fit to the SDSS-DR7 data of the $G-R$ color

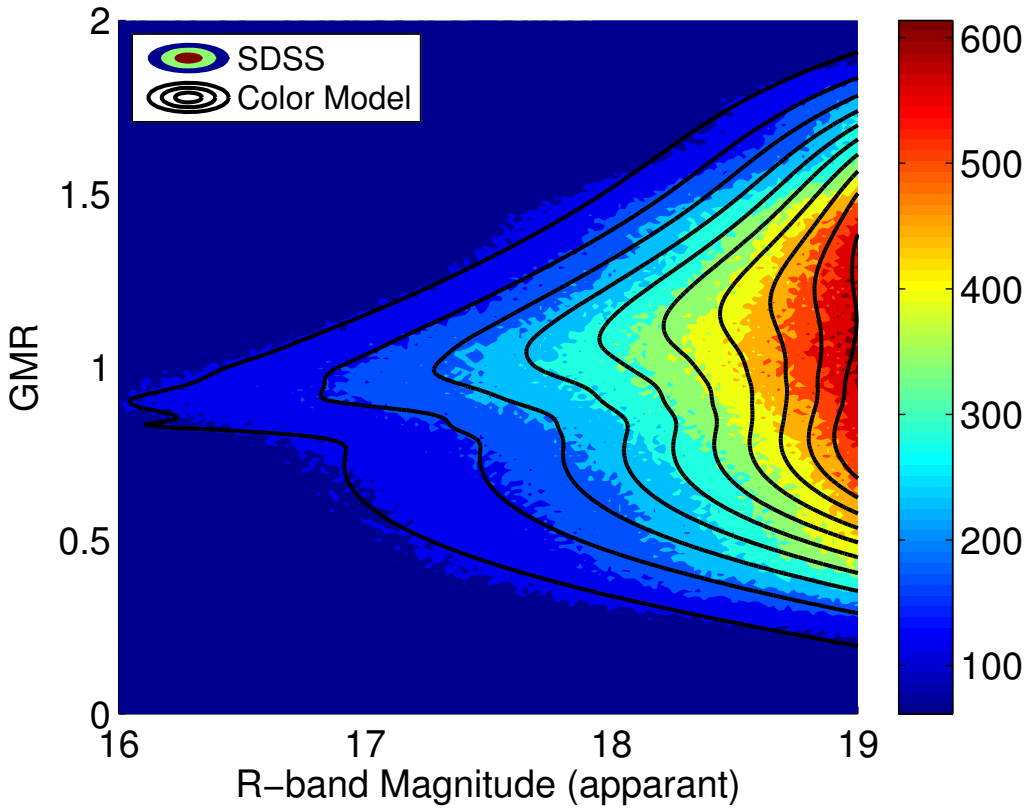

Figure 5.4: The contour plot indicates galaxy density in the color-magnitude space as observed in SDSS main sample (shown in filled contours) and that predicted by the color model with parameters suggested by Table.5.2 (shown in thick black lines).

Table 5.2: Fitted Values of the $G-R$ Color Model Parameters

Parameter	Best-fit Value	σ
a_r	2.7574	0.0031
a'_r	-0.6	N/A
a''_r	3	N/A
b_r	0.6899	0.0004
c_r	0.4222	0.0020
d_r	0.0011	0.0003
a_b	0.9705	0.0083
b_b	0.6294	0.0014
c_b	0.4221	0.0053
d_b	0.1991	0.0008
s_f	-0.1636	0.0011
${M_r}^c$	-20.886	0.0089

The best-fit values and 1σ uncertainties of the $G-R$ color model parameters in Eq. 5.7 through 5.11 constrained by MCMC. I fixed the slope a'_r and a''_r to -0.6 and 3 respectively, because the SDSS-DR7 data, to which I fit this color model, is not sensitive to their values.

model using values in Table 5.2 can be seen in Figure 5.3, in which the observed galaxy number density in the $G-R$ color - m_r plane is plotted in filled color contours, whereas the color model prediction is plotted in bold solid black lines.

I use fiducial values of -0.6 for a'_r and 3 for a''_r because it is found that the fitting data is insensitive to their values (there are simply not enough bright galaxies at high redshift to constrain the $G-R$ color evolution slope beyond $z = 0.3$.). The fiducial values of these slopes are based on the results of Hao et al. [2009]. Please refer to Appendix E for more details of fitting the SDSS-DR7 data using MCMC and the limitations.

5.5 Modeling the Observed Galaxy Velocity Dispersion

With the HOD and $G-R$ color model, the fast halo sight-line technique in Chapter 2 can be applied to generate sky patches with simulated galaxies that have R-band magnitude and $G-R$ color. Subsequently, these two pieces of information allow for predictions of clusters' observed richness in MaxBCG and the number of galaxies that would have spectroscopic

follow-up in SDSS, both essential to reproduce the stacked velocity dispersion histogram in Figure 5.6.

Figure 5.5 shows an visualized sky patch of $0.4 \times 0.4 arcmin$ in size centered on a $2 \times 10^{14} h^{-1} \mathrm{M}_{\odot}$ target cluster. The halo sight-line includes all haloes above $M_{\mathrm{min}} = 5 \times 10^{13} h^{-1} \mathrm{M}_{\odot}$ to a maximum redshift of $z_{\mathrm{max}} = 1.2$. Optical galaxies are simulated using the HOD model in §5.3 and the $G-R$ color model in §5.4. The "×" symbols represent galaxies in the target cluster, while the "+" symbols are those residing in a projected haloes. The size of each symbol correspond to the apparent R-band magnitude of that galaxy (a larger symbol indicate a brighter galaxy, and *vice versa*). The color of each symbol reflects the simulated $G-R$ color of that galaxy, as indicated by the color scale to the right. In the top panel of Figure 5.5, I plot the θ_{200} size of each halo in solid blue lines, with the exception of the target one, which in shown in black color. In the lower panel, I circle galaxies whose $G-R$ color fall within the appropriate red-sequence color range as defined in the MaxBCG cluster finding algorithm [Koester et al., 2007b] in green. These objects, if falling within the θ_{200} aperture of the target cluster, would count towards the MaxBCG cluster richness.

It is worth mentioning that in my simulations, I use the correct halo centers and θ_{200} values to find the N^{200} richness. Such N^{200} measurements will have a smaller variance than the actual MaxBCG clusters, as it ignores the mis-centering effect and the uncertainty in θ_{200} estimation during cluster-finding.

Nonetheless, it is now possible to go into each sky patch like the one in Figure 5.5 and identify galaxies brighter than $m_R = 17.76$, then apply the analytical velocity dispersion in Eq. 5.1 by Evrard et al. [2008]. The observed radial velocity dispersion $c\delta z$ for each BCG-galaxy pair with spectroscopy can be consequently computed and placed into the corresponding N^{200} richness bin as in Figure 5.6.

The four panels (richness between $10 \sim 15$, $16 \sim 30$, $31 \sim 50$, and $51 \sim 199$) in Figure 5.6 cover all MaxBCG clusters with $N^{200} \geq 10$. The "+" symbols correspond to the observations in SDSS-DR7 by Becker et al. [2007] whereas the solid lines in cyan color

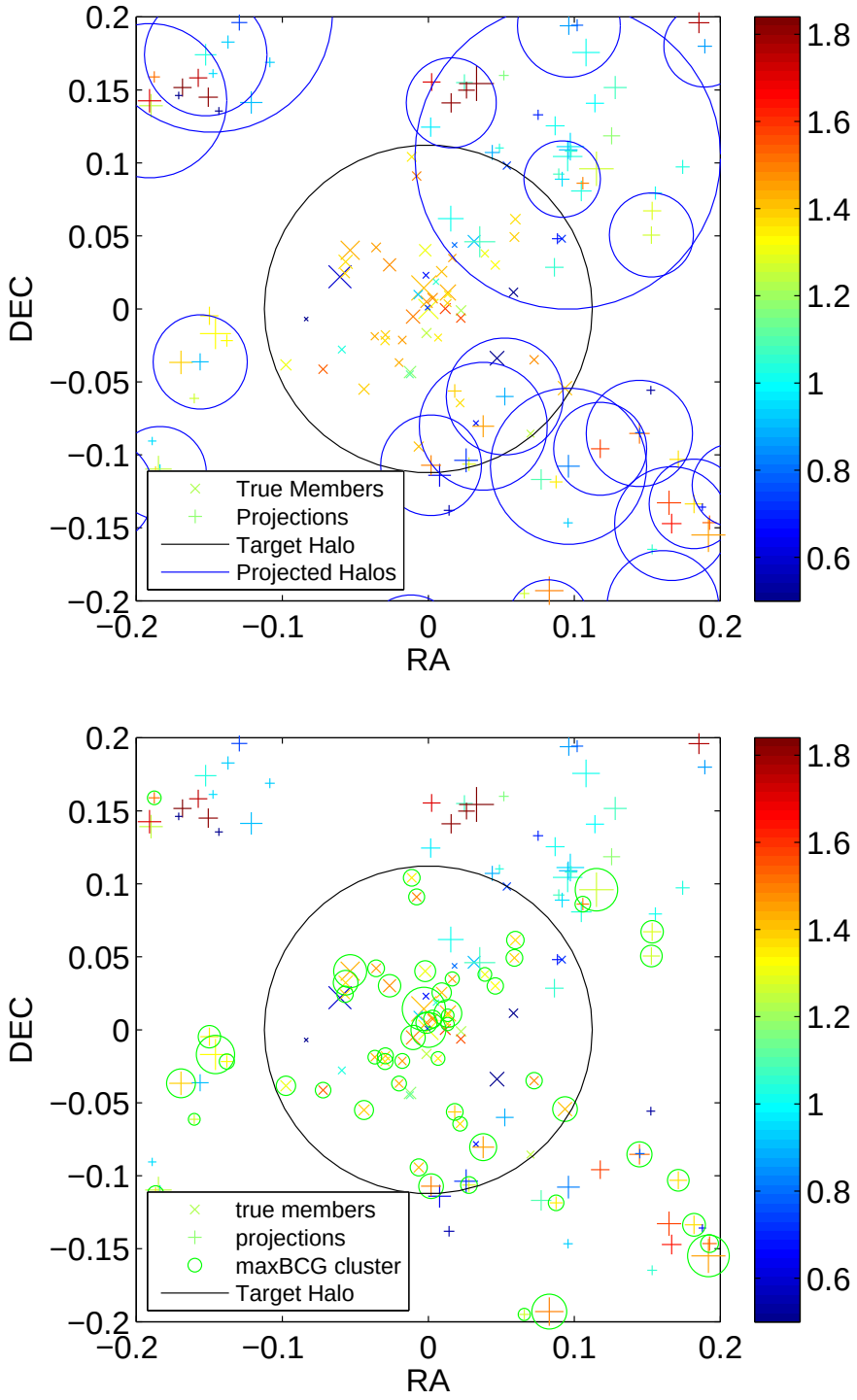

Figure 5.5: A visualized sky patch of 0.4×0.4 *arcmin* in size centered on a $2 \times 10^{14} h^{-1} \mathrm{M}_{\odot}$ target cluster. The size of each symbol reflect the apparent R-band magnitude of that galaxy while its color indicates the galaxy's $G-R$ color. The top panel shows the θ_{200} sizes of the underlying haloes, whereas the bottom one highlights galaxies that fall within the MaxBCG color window.

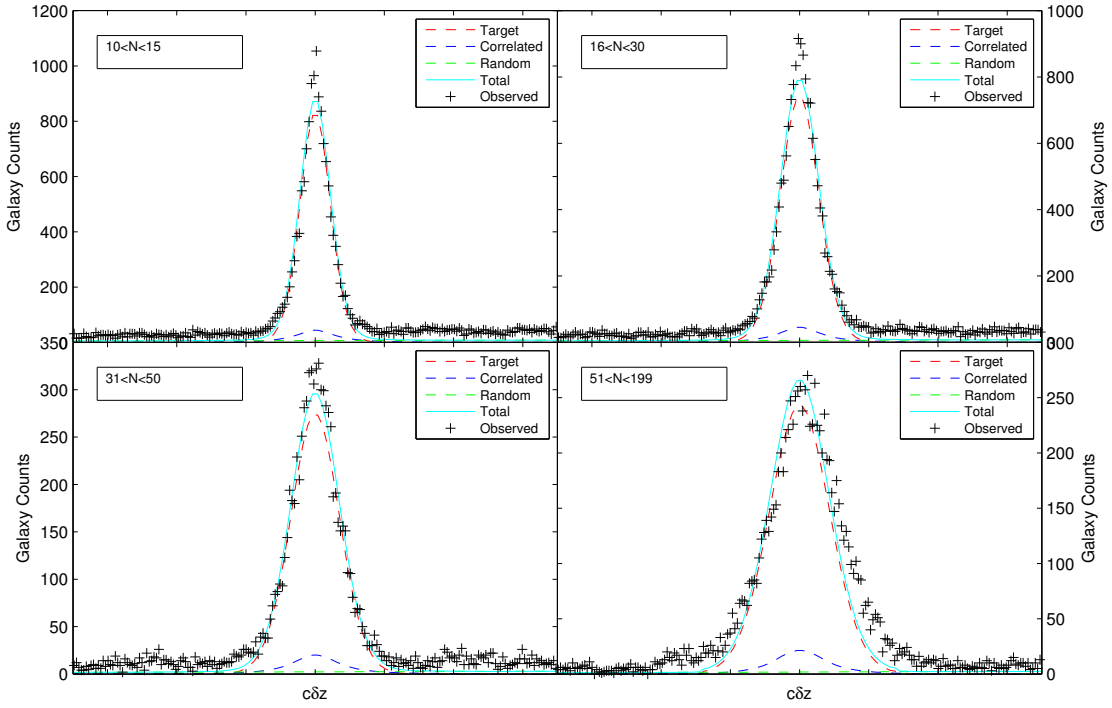

Figure 5.6: The stacked galaxy radial velocity dispersion in four richness bins ($10 \sim 15$, $16 \sim 30$, $31 \sim 50$, and $51 \sim 199$) of the MaxBCG catalogue. The "+" symbols correspond to the observation by Becker *et al.*, whereas the solid lines in cyan show the result predicted by the projected halo model. The total signal is subcategorized into the intrinsic target contribution (red dashed), correlated contribution (blue dashed), and the random background (green dashed). For further details on the model prediction, see text in § 5.5.

display the result predicted by the projected halo model using the HOD and color model discussed previously. In the model prediction, the total contribution is broken down into the intrinsic target (red dashed), correlated (blue dashed), and random background (green dashed) contributions.

As can be seen in Figure 5.6, the modeled radial velocity dispersions fit the observations well in the main Gaussian modes. The model also shows that the correlated structure has an effect less than 5% on this measurement, mostly because of the spectroscopic selection which limits the contributions from smaller haloes.

The discrepancy on the wings indicates that the HOD model is under-predicting the number of galaxies brighter than $m_R = 17.76$ in small haloes from the random background component. Furthermore, the most massive clusters ($51 < N^{200} < 199$) exhibit an asymmetry in the radial velocity dispersion in the observation, which is not accounted for by the model.

5.6 Discussions

Modeling and explaining the stacked radial velocity dispersion in MaxBCG clusters was an initial attempt to validate and apply the projected halo model to observations. Modeling the HOD and red and blue galaxy populations were later found to be necessary in order to reproduce the result in Figure 5.6.

The result showed that correlated contributions have a less than 5% effect on this measurement, limited by the spectroscopic selection in SDSS. Furthermore, it also showed that the asymmetry in observed $c\delta z$ at the highest richness bin cannot be explained by correlated haloes nearby.

While encompassing a wide range of topics and having its own historical significance, the results shown in this chapter were not perfectly suitable for publication in refereed journals. Though nontrivial, the HOD and color model describing the galaxy populations

in SDSS were by-products of the process. In addition, the HOD model was modeled with the absence of a spatial component and subsequently fitted without the galaxy angular correlation data, which are considered canonical.

Hence, works shown in this chapter remained in the form of manuscripts as I moved on to produce the results in Chapter 3 and Chapter 4.

APPENDIX A

The Projected Halo Model Validation

To validate the projected halo model, I take two independent light cones (namely PO and NO) from the Hubble Volume simulation catalogue [Evrard et al., 2002], and compare the number of haloes projected within a quasi-cylindrical volume centered on a target halo from the simulation with the analytical prediction. Note that in this appendix, I adopt the same cosmology used in the Hubble Volume simulation, *i.e.*, $\Omega_m = 0.3$, $\Omega_\Lambda = 0.7$, and $\sigma_8 = 0.9$ for comparison. For the same reason, I use the mass function fitted by [Evrard et al., 2002], too.

In the simulated light cones, I choose target haloes whose mass fall within $M_{\rm t} = 2 \times 10^{14} h^{-1} {\rm M}_\odot \pm 10\%$[1] and count all haloes, whose masses lie above the minimal mass of $M_{\rm min} = 5 \times 10^{13} h^{-1} {\rm M}_\odot$ in the catalogue and are located within volume bounded by the θ_{200} aperture of the target halo with a length of ± 0.03 in redshift[2].

I show, in Figure A.1, such number counts from the two light cones in red and blue solid lines with their $\pm 1\sigma_m$ error bars, and the analytical prediction using the projected halo model in a solid black line. As can be seen, the analytical model yields numbers consistent with the simulation results. In addition, results calculated including only the random contribution, *i.e.*, ignoring halo-halo correlations completely, are shown in solid green color. Via highlighting the gap between the projected halo model and the random-

[1] I choose $M_{\rm t} = 2 \times 10^{14} h^{-1} {\rm M}_\odot$ as opposed to the more frequently quoted $M_{\rm t} = 5 \times 10^{14} h^{-1} {\rm M}_\odot$ in Chapter 3 and 4 for its greater statistical power.

[2] For consistency with the SDSS photometric redshift uncertainty of ± 0.03.

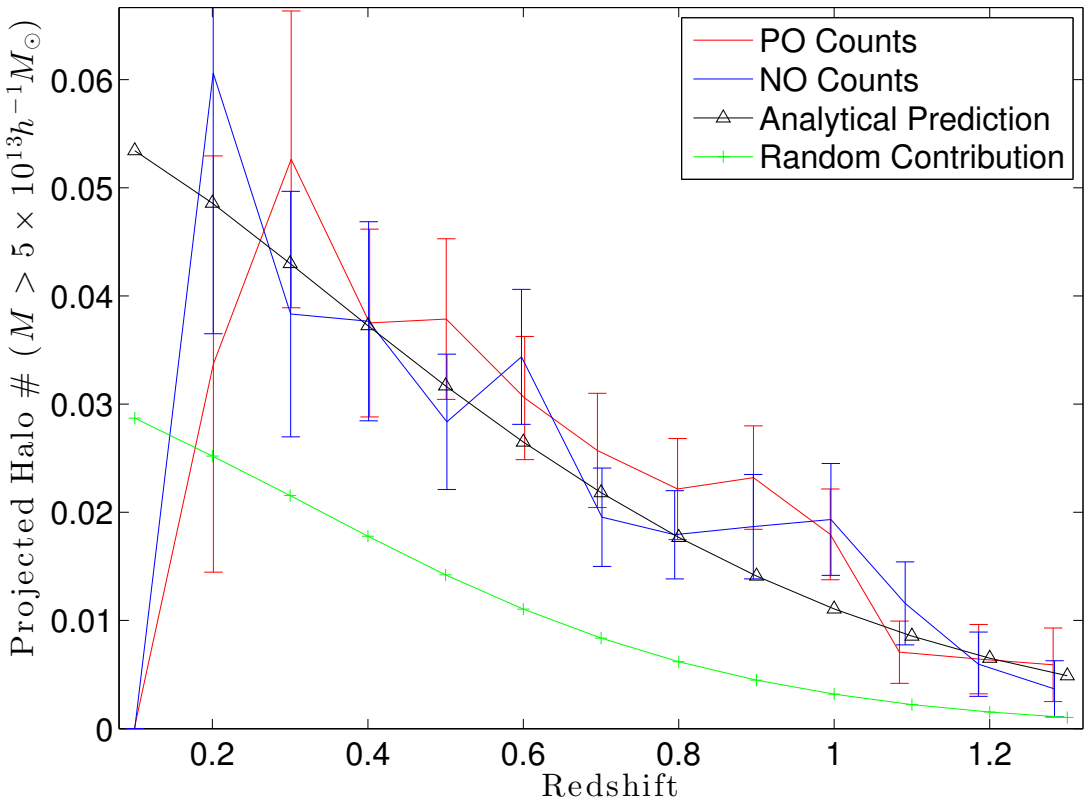

Figure A.1: A comparison to the Hubble Volume simulation, in which PO and NO are two independent light cones in the simulation catalog. In this plot the target halo mass $M_{\rm t} = 2 \times 10^{14} h^{-1} {\rm M}_\odot$; the redshift range is set to $z_{\rm t} \pm 0.03$ to mimic the level of redshift uncertainties in photometric redshift measurements; the aperture size is taken to be that equivalent to the θ_{200} of the target and counted everything above $5 \times 10^{13} h^{-1} {\rm M}_\odot$ within the covered region. Error-bars indicate the Poisson uncertainty within each bin.

only scenario, I show that i) a uniform background estimation is inefficient when dealing with massive targets; and ii) the halo-halo correlation will dominate cluster projections as one moves to deeper redshifts.

APPENDIX B

Computing the Conditional Signal Function

When a galaxy cluster lies in the same sight-line with the target cluster, one expects a fraction of the projected halo's signal to be counted towards $S^{\rm obs}$ of the target cluster in Eq. 2.1. An obvious approach to compute this fraction is to lay the signal of each halo in the sight-line onto a pixel map, as shown in Fig. 2.1, and apply the signal filters to get $S^{\rm obs}$. However, this method suffers two major drawbacks. Firstly, in order to obtain accurate values, the resolution of the pixel map needs to be sufficiently high, which quadratically increases the computation time. Secondly, the stacked pixel map erases information of the host haloes, without which the study of projection demographics in §3.1.2 would have been impossible.

In this appendix, I explain how computations of this fraction can be quantified into a 4-parameter mathematical problem, hence allowing for interpolations of pre-computed value tables, which significantly reduce the computation time and save information of the host haloes in the meantime.

As can be seen in Fig. B, the fraction, $f^{\rm CSF}$, of the projected signal that will get assigned to $S^{\rm obs}$ depends on the following factors: the size and profile of the signal filter, ${\theta_{200}}^{\rm tar}$, ${\theta_{\rm core}}^{\rm tar}$; the size and profile of the projected cluster ${\theta_{200}}^{\rm proj}$, ${\theta_{\rm core}}^{\rm proj}$; and the angular separation between the centers d_θ. Placing the projected cluster at the origin and integrating

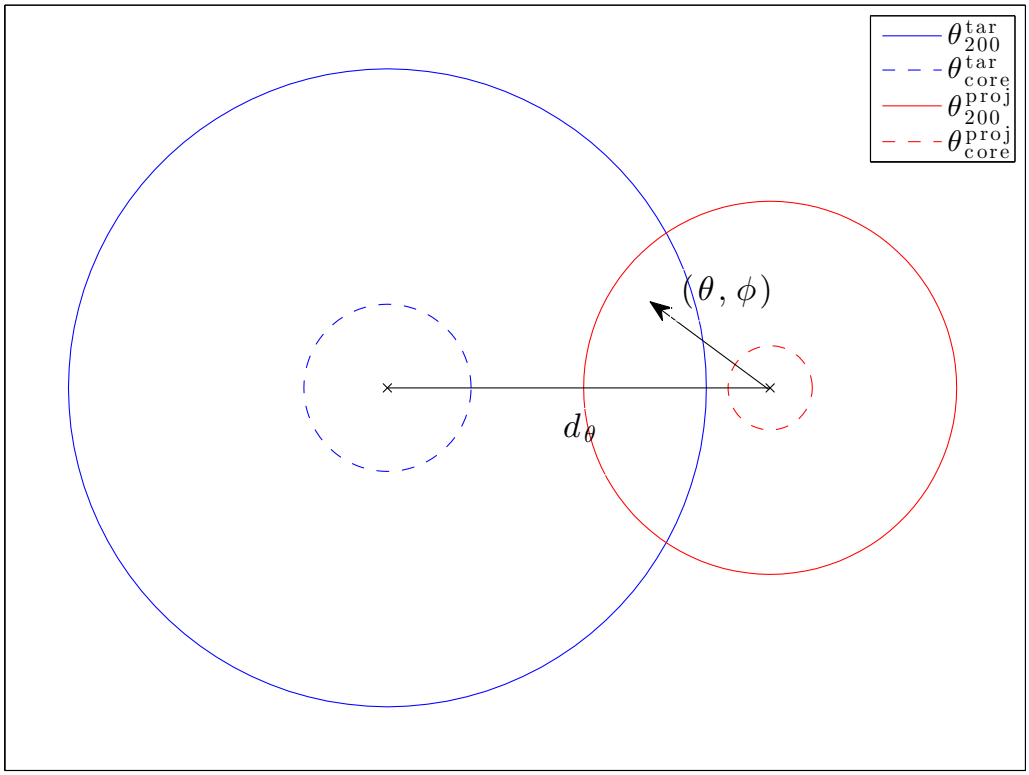

Figure B.1: An illustration of the Conditional Signal Function problem. The red circle indicates the θ_{200} size of the projected halo in the sky and the blue circle shows that of the target. For reference, this figure is produced using the sizes of a $M_{\mathrm{t}} = 5\times10^{14}h^{-1}\mathrm{M}_{\odot}, z_{\mathrm{t}} = 0.3$ target and a $M = 1\times10^{14}h^{-1}\mathrm{M}_{\odot}, z = 0.3$ projected halo.

its signal profile within ${\theta_{200}}^{\rm proj}$ in polar coordinates

$$f^{\rm CSF} = \int\int f^{\rm filt}(d_x)\lambda^{\rm proj}(\theta)\sin\theta {\rm d}\theta {\rm d}\phi, \tag{B.1}$$

$$d_x = \sqrt{d_\theta^2 + \theta^2 + 2d_\theta\theta\cos\phi}, \tag{B.2}$$

in which $f^{\rm filt}$ is the filter function in §2.3.3.1 and $\lambda^{\rm proj}$ is the signal profile of the projected cluster.

I pre-compute values of $f^{\rm CSF}$ and store them in a 4-dimensional data table, by rescaling everything to ${\theta_{\rm core}}^{\rm proj}$ using self-similarities of the signals. In the case of the top-hat or the Bg-sub filter, the number of parameters can be further reduce to 3 as their shapes only depend on ${\theta_{200}}^{\rm tar}$. When computing contributions to $S^{\rm obs}$ from each projected halo, I simply use a 4- or 3-D interpolation of the pre-computed tables.

In Figure B, I move a $M = 1\times10^{14}h^{-1}{\rm M}_\odot, z = 0.3$ projected halo gradually towards the center of a $M_{\rm t} = 5\times10^{14}h^{-1}{\rm M}_\odot, z_{\rm t} = 0.3$ target and compute $f^{\rm CSF}$ as a function of their separation d_θ in the SZ wavelength using the interpolation (in solid lines) method versus creating 1001×1001 pixel maps (in dashed lines). As indicated, the interpolation method gives accurate results for both the top-hat and the matched filter along the entire dynamic range.

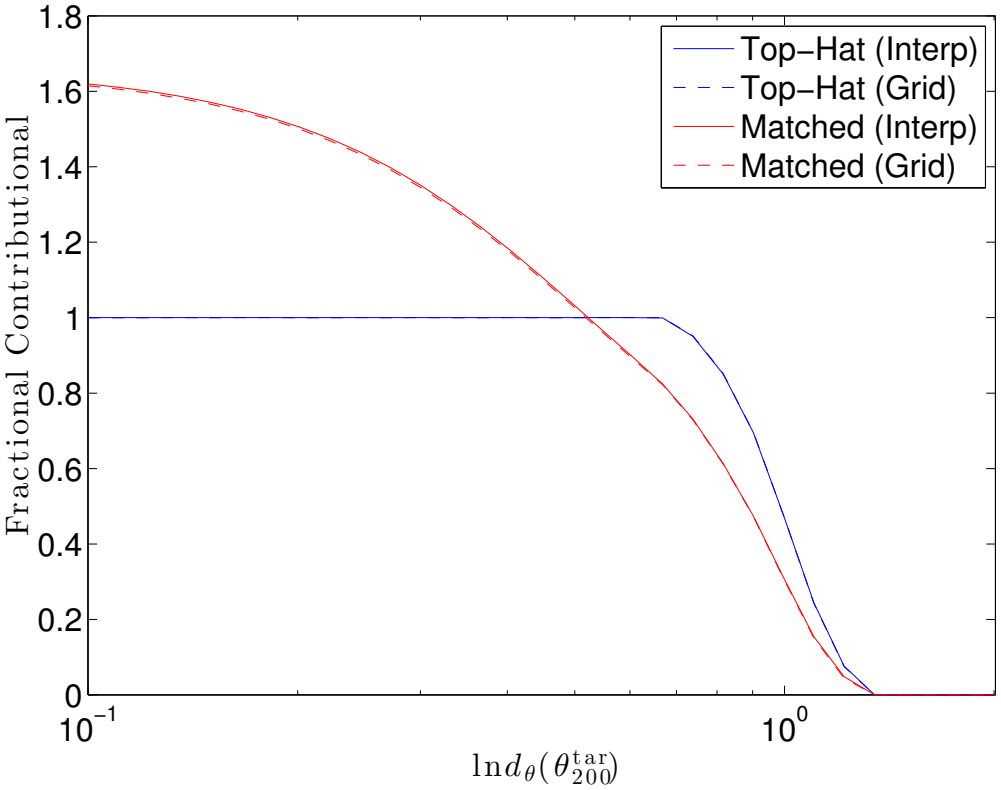

Figure B.2: A comparison of the conditional signal fraction, $f^{\rm CSF}$, computed using interpolations versus pixel maps. The target halo has $M_{\rm t} = 5\times10^{14}h^{-1}{\rm M}_\odot, z_{\rm t} = 0.3$ and the projected halo is $M = 1\times10^{14}h^{-1}{\rm M}_\odot, z = 0.3$. The signal profiles are taken to be the projected β-profiles in SZ with a β of $2/3$.

APPENDIX C

The Characteristic Mass Scale Defined by a Sky Surface Density

In § 3.2, I explored the projection enhancement as a function of the target mass and redshift. It is obvious that, when investigating the effect of varying target halo redshift, using a constant target mass across the entire range from $z_t = 0.1$ to $zt = 1.5$ is not optimal, as a $5 \times 10^{14} h^{-1} M_\odot$ halo may be common between redshift of $z = 0.2 \sim 0.4$, but is much rarer near $z = 1.5$.

Thus, I adopt a characteristic mass scale defined by a constant sky surface density, *i.e.*, a series of halo masses at different redshifts that share a common sky surface density per redshift. In Figure C.1, I show the two scales defined by $M(z = 0.3) = 5 \times 10^{14} h^{-1} M_\odot$ and $M(z = 0.3) = 1 \times 10^{14} h^{-1} M_\odot$ using blue and green lines, respectively. For the first scale defined by $M(z = 0.3) = 5 \times 10^{14} h^{-1} M_\odot$, one expects to observe 1 halo above such mass scale per $\sim 100\,\mathrm{deg}^2$ in a redshift shell of ± 0.05 in thickness. The second scale ($M(z = 0.3) = 1 \times 10^{14} h^{-1} M_\odot$) approximately translates to a sky surface density of 1 per 2 deg^2 in the same redshift slice. The sharp decline towards $z = 0.1$ seen in Figure C.1 is driven by the sky area effect, *i.e.*, the physical space projected in the same redshift range becomes rapidly smaller as $z \to 0$; and the decrease beyond $z \sim 0.4$ corresponds to the decline in the halo mass function as there are fewer massive haloes at earlier epoch.

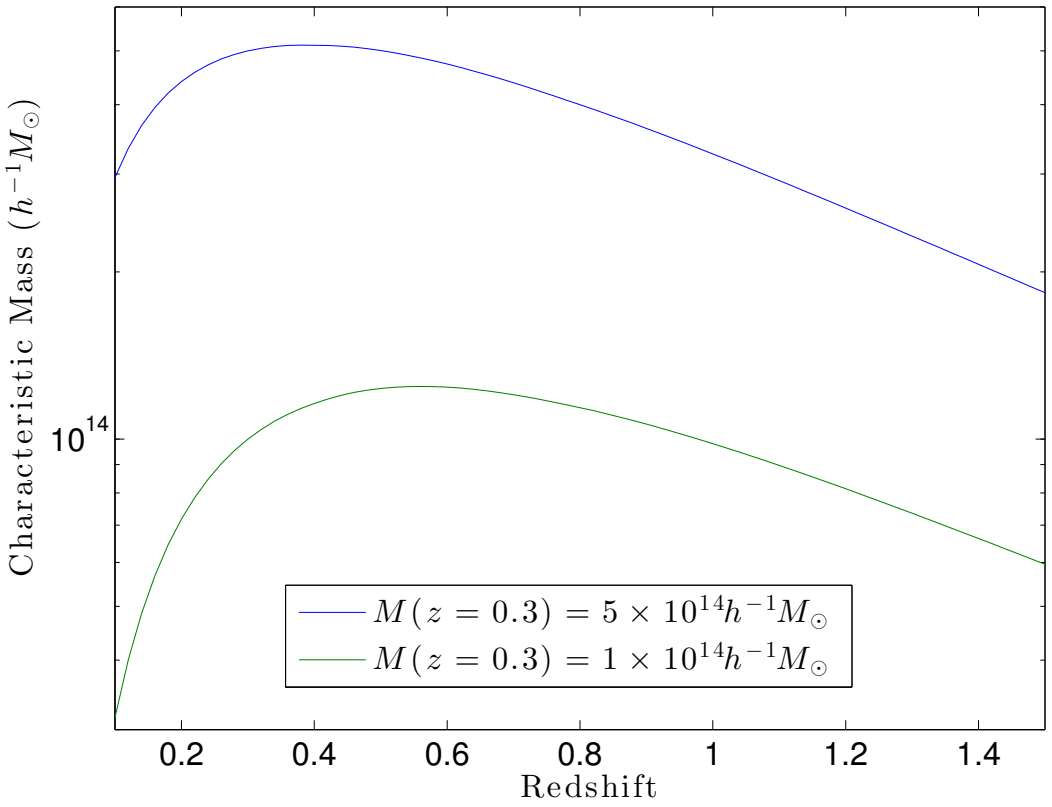

Figure C.1: The characteristic mass scales defined by constant sky surface densities. We plot two scales, $M(z=0.3) = 5\times10^{14}h^{-1}\mathrm{M}_\odot$ and $M(z=0.3) = 1\times10^{14}h^{-1}\mathrm{M}_\odot$, from redshift of 0.1 to 1.5. The higher mass scale corresponds to a sky surface density of $\sim$ 1 per 100 deg^2 in a redshift shell of $\pm$0.05 in thickness while the lower one has a density of $\sim$ 1 per 2 deg^2 in the same range.

APPENDIX D

M_{200} with Respect to the Critical Density vs. the Mean Density

It has been a controversy whether to use M_{200_c} or M_{200_m} in the halo mass convention. The previous is defined with respect to the critical density whereas the latter is defined with respect to the matter one. In this dissertation, I adopt the M_{200_c} convention, but confront with the need to covert masses defined in M_{200_m} to M_{200_c}, or *vice versa* in several occasions. For instance, in the Coupon et al. [2012] HOD model in Eq. 2.4, halo masses represented by M' use the M_{200_m} convention.

One possible mean to covert from M to M' is re-integrating the NFW density profile with an assumed concentration to the new boundary. In this work, I choose a simpler approach, which matches the sky surface densities of the two convention at each redshift, creating a one-to-one mapping between M_{200_c} and M_{200_m} at each cumulative sky surface density. I argue that this approach has the merit of being completely density profile independent.

The author would like to note that such conversion is applied only when using the Coupon et al. [2012] HOD model in Eq. 2.4. While the [Tinker et al., 2008] mass function also adopts the M_{200_m} convention, I simply has to re-computed the $\delta(z) = 200$ values with respect to $\overline{\rho}_{\rm crit}$ to the corresponding $\Delta(z)$s with respect to $\overline{\rho}_m$.

APPENDIX E

Using MCMC to Constrain HOD and Color Model Parameters

In Chapter 5, I presented an HOD model (Eq. 5.2 through 5.6) and a $G-R$ color model (Eq. 5.7 through 5.11) of the SDSS-DR7 galaxies. The HOD model has 10 parameters while the color model uses 12. Due to the dimensions of these parameter spaces, I employed an MCMC approach to constrain those parameters.

E.1 MCMC

MCMC was first introduced by Metropolis et al. [1953] as an efficient method to find the minimum / maximum in an unknown probability distribution with a large number of parameters. Instead of computing the probability at each grid point, MCMC utilizes a Markov chain and visits points along its path in a stochastic process. Therefore, the computational complexity of MCMC scales linearly with the number of parameters, instead of exponentially, making it particularly useful in this case.

An important piece of the MCMC approach is the random walk sampling algorithm. In this work, I used a Metropolis-Hastings [Hastings, 1970] algorithm to sample the next step. Specifically, at each step of the Markov chain with location vector $\boldsymbol{x}_{\rm i}$ in the parameter space and its probability, $P(\boldsymbol{x}_{\rm i})$, and number of stays $s_{\rm i}$,

- The trial step location $\boldsymbol{x}_{\mathrm{i+1}}^{trial}$ is proposed by

$$\boldsymbol{x}_{\mathrm{i+1}}^{trial} = \boldsymbol{x}_{\mathrm{i}} + \delta\boldsymbol{x}, \tag{E.1}$$

  where $\delta\boldsymbol{x}$ is a random variable drawn from a multivariate normal distribution,

$$\delta\boldsymbol{x} \sim \mathrm{N}(\mathbf{0}, l^2\,\boldsymbol{\Sigma}_{\boldsymbol{x}}), \tag{E.2}$$

  in which $\boldsymbol{\Sigma}_{\boldsymbol{x}}$ is the covariance of the sampling distribution and l is the step-length.

- Probability at the trial step location $P(\boldsymbol{x}_{\mathrm{i+1}}^{trial})$ is then computed and compared to $P(\boldsymbol{x}_{\mathrm{i}})$ with a random number p sampled from a U(0, 1) distribution.

  – If $p < P(\boldsymbol{x}_{\mathrm{i+1}}^{trial})/P(\boldsymbol{x}_{\mathrm{i}})$, the chain accepts and moves into location

$$\boldsymbol{x}_{\mathrm{i+1}} = \boldsymbol{x}_{\mathrm{i+1}}^{trial}, \tag{E.3}$$

$$s_{\mathrm{i+1}} = 1. \tag{E.4}$$

  – Otherwise, stay at $\boldsymbol{x}_{\mathrm{i}}$ and add one to the number stays

$$s_{\mathrm{i}} = s_{\mathrm{i}} + 1. \tag{E.5}$$

This process is repeated until the desired convergency is reached. A simple illustrative code of this process using Matlab language can be seen in Program E.1.

E.2 The Score Functions

A key component in the MCMC method discussed in § E.1 is the computation of $P(\boldsymbol{x})$. In constraining both the HOD and the color model, I summarized the observation results into binned distributions with galaxy counts in each bin. Thus, the score functions in both cases

```
function AnboMCcore(scoreFun, probFun, chain, covMat, maxTrial)
%anboMCcore - MCMC core function
%   scoreFun evaluates the position vector
%   probFun takes in trialScore and lastScore, gives prob between 0 and 1
%   chain must be a Java Stack object with {loc, stay, score} structure
%       and not empty
%   this allows resuming a previously run chain

lastLoc = chain.Loc.pop();
lastStay = chain.Stay.pop();
lastScore = chain.Score.pop();

for i = 1:maxTrial
    trialLoc = mvnrnd(lastLoc,covMat);
    trialScore = scoreFun(trialLoc);
    prob = probFun(trialScore,lastScore);
    if rand < prob
        chain.Loc.push(lastLoc);
        chain.Stay.push(lastStay);
        chain.Score.push(lastScore);
        lastLoc = trialLoc;
        lastScore = trialScore;
        lastStay = 1;
    else
        lastStay = lastStay + 1;
    end
end

chain.Loc.push(lastLoc);
chain.Stay.push(lastStay);
chain.Score.push(lastScore);

end
```

Program E.1: A simple illustration of the MCMC process in Matlab code.

are the χ^2 statistics.

For the HOD model, initially, I used the galaxy sky surface density as a function of apparent R-band magnitude in the SDSS-DR7 main galaxy catalogue and its joint distribution in apparent magnitude - redshift space in the spectroscopic subset. It was later discovered that these two benchmarks are not enough to tailor the 10-parameter model to yield results consistent with the MaxBCG catalogue, hence, the MaxBCG results subsequently brought in to the score function.

$$\chi^2_{\rm HOD} = \chi^2_{main} + \chi^2_{spec} + \chi^2_{MaxBCG}, \tag{E.6}$$

in which χ^2_{main} is calculated via comparing the predicted galaxy sky surface density as a function of apparent R-band magnitude to that observed in SDSS-DR7; χ^2_{spec} is computed via comparing the HOD prediction of galaxy distribution in $m_R - z_{spec}$ space (solid thick lines in Figure 5.3) to that observed in SDSS-DR7 (scattered thin lines in Figure 5.3); and χ^2_{MaxBCG} is calculated via comparing the predicted cluster distribution as a function of richness versus the actual MaxBCG catalogue, as can be seen in Figure E.1.

In constraining the color model parameters, only the SDSS-DR7 main galaxy catalogue and the spectroscopic subset data are used. In the main sample, the color model's prediction of the the galaxy distribution in $G-R-m_R$ space (shown as black solid lines in Figure 5.4) is compared to the observation (shown as filled color contours) to yield $\chi^2_{main'}$. For the spectroscopic subset, the same quantity is calculated in individual redshift slices and then combined to yield $\chi^2_{spec'}$. Hence,

$$\chi^2_{color} = \chi^2_{main'} + \chi^2_{spec'}. \tag{E.7}$$

Note that primes are used to distinguish from the HOD model χ^2s in Eq. E.6.

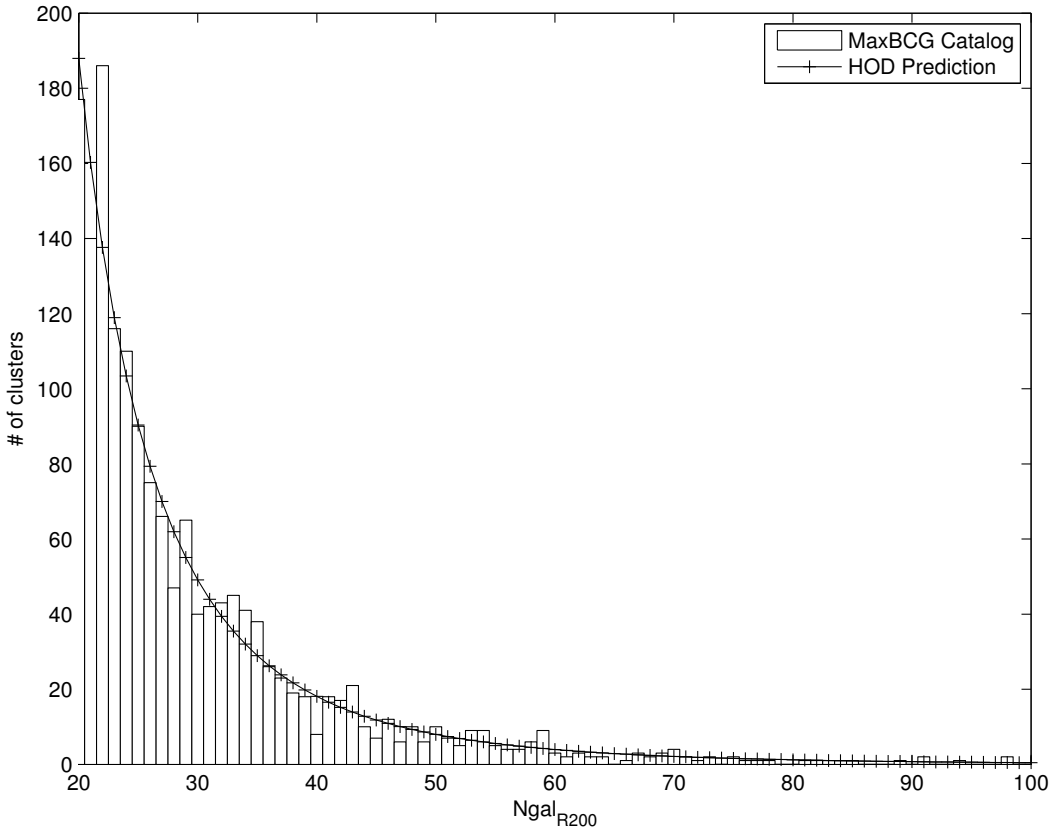

Figure E.1: Histogram of the number of galaxy clusters as a function of N_{gal} in the MaxBCG catalogue and that predicted by the HOD model using the parameters described in Table.5.1.

E.3 The Automated Optimizer

In practice, I found that the convergence rate for the HOD model using the canonical MCMC process as described in § E.1 to be unsatisfactory. Because of the degeneracy in the model parameters that cannot be well disentangled by observational data, the chain wanders in the gigantic parameter space for a long time before converging. Each step of the MCMC process takes about 5 seconds to compute, requiring more than 24 hours for 20,000 steps.

Furthermore, Dunkley et al. [2005] has shown that to gain the fastest convergency in a rather complicated probability function space, the acceptance rate, *i.e.*, the percentage at which a trial step is accepted in the process described in § E.1, should roughly be around 0.3. The acceptance rate, can be tuned by the step-length l in Eq. E.2.

Besides the tuning to achieve optical acceptance rate, evaluation of the covariance, $\mathbf{\Sigma}_{\boldsymbol{x}}$, in Eq. E.2 is equally crucial. Since the model is known to have degeneracies, it is much more efficient to sample steps using the local covariance $\mathbf{\Sigma}_{\boldsymbol{x}}$, which essentially samples along orthogonal directions in the eigenvector of $\boldsymbol{x}$.

Both adjusting l and evaluating $\mathbf{\Sigma}_{\boldsymbol{x}}$ require one to pause the running chain and engage in command-line interactions. To exacerbate the situation, adjusting l to achieve optimal acceptance rate usually requires a "trial and failure" approach that needs multiple rounds of inputs / adjustments during a period of time. To obtain absolute automation such that these MCMC can be run in parallel, I designed an Automated Optimizer, which works as a master controller to oversee the individual MCMC segments and make adjustments in between.

The Automated Optimizer runs MCMC segments in two modes, a long run (10,000 steps) and a short run (100 steps). The short run is executed for adjusting the acceptance rate α to the desired value $\alpha^{optimal}$, at which point a long run is then executed using the step-length l and covariance matrix $\mathbf{\Sigma}_{\boldsymbol{x}}$.

From the controller's point of view, at each break after the previous MCMC segment i,

- if run i was a short run,
  - if α_{i} falls within an "acceptable" range $\alpha^{optimal} \pm \Delta\alpha$, then execute a long run $\mathrm{i}+1$ with the same parameters, *i.e.*, $l_{\mathrm{i}+1} = l_{\mathrm{i}}$, $\mathbf{\Sigma}_{\mathrm{i}+1} = \mathbf{\Sigma}_{\mathrm{i}}$.
  - otherwise, execute a short run with the adjusted step-length

$$l_{\mathrm{i}+1} = l_{\mathrm{i}} * \sqrt{\frac{\alpha_{\mathrm{i}}}{\alpha^{optimal}}}. \tag{E.8}$$

- if run i was a long run, re-evaluate the covariance matrix $\mathbf{\Sigma}_{\mathrm{i}+1}$ based on the i-th chain and submit a short run $\mathrm{i}+1$ to allow for adjustments in the acceptance rate α.

By inserting a flag that test for overall drift of location $\boldsymbol{x}$ in the parameter space, the controller even tell if the MCMC process has converged.

In practice, the above Automated Optimizer greatly increased the computation efficiency by removing intermediate processing and allowed for execution in parallel on a Central Processing Unit (CPU) cluster.

In Figure E.2, I show an illustration of a converged chain in the 10-dimensional parameter space of the color model (2 of the parameters were set to their fiducial values, as explained in § 5.4). The lower left triangle of the plot matrix includes the scattered points of visits in the Markov chain, whereas the upper right ones indicate the 1, 2, and 3σ contours in joint parameter spaces. Distributions of each parameter are shown along the diagonal. All results here have points weighted by their numbers of stays.

Finally, as an example to the Automated Optimizer described in this section, a Matlab code that carries out such tasks is attached in Program E.2.

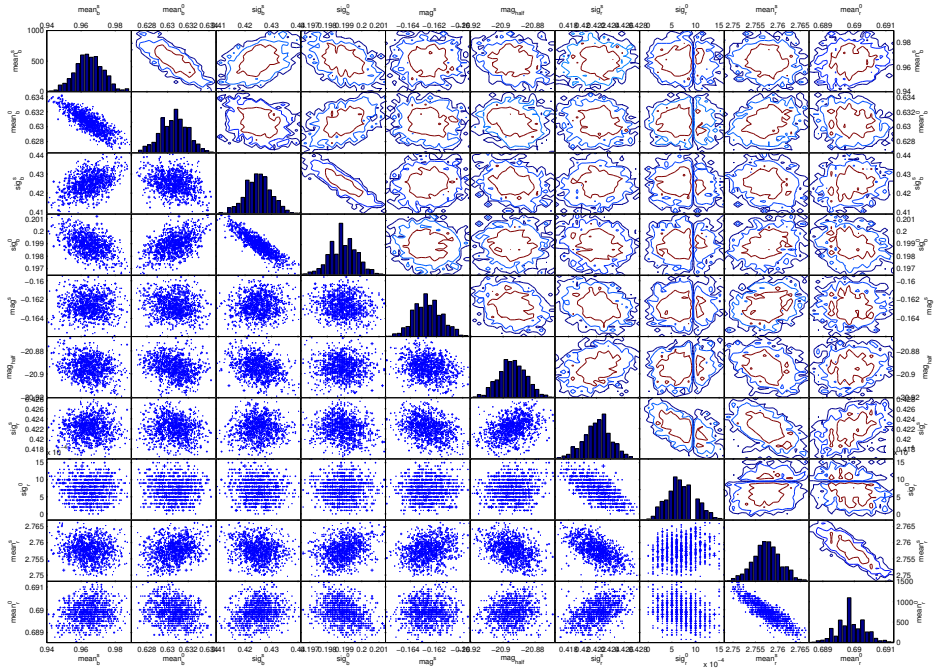

Figure E.2: A sample snapshot of the MCMC simulation after parameters have converged when constraining the color model parameters. Lower left shows the scatter plots of covariances among parameters with the sizes of symbols indicating the number of steps the chain stayed there. Upper right convert these scattered points into a weighted covariance contours with each contour representing 1, 2 and 3σ intervals. The diagonal contains the variances of each parameter.

```
function chain = AnboMCbot(scoreFun,probFun,startLoc,startCov,totTime,ver
% A sample Matlab code performing the Automated Optimization process of M

shortRun = 100;
longRun = 10000;
safeTimeFac = 1.1;
optimalAccRate = 0.3;
goodAccDiff = 0.05;
goodDrift = 1;
minAmp = 1e-4;

%identify the eval time
firstTic = tic;
startScore = scoreFun(startLoc);
eachTime = toc(firstTic);
verbFun(sprintf('Processing time each step = %.4f sec', eachTime));

chain.Loc = java.util.Stack;
chain.Stay = java.util.Stack;
chain.Score = java.util.Stack;
chain.Loc.push(startLoc);
chain.Stay.push(0);
chain.Score.push(startScore);

thisAmp = 2;
thisCov = startCov;
thisTrialN = shortRun;
thisRun = 1;
goodRun = 0;
adjAccFlag = true;

while totTime - toc(firstTic) > safeTimeFac*longRun*eachTime

    AnboMCcore(scoreFun, probFun, chain, thisAmp.*thisCov, thisTrialN);

    thisCP = AnboMCchainProp(chain);
    verbFun(sprintf('\nRun #%d',thisRun));
    verbFun(sprintf('\tSteps   = %d',thisTrialN));
    verbFun(sprintf('\tAccRate = %.2f',thisCP.accRate));
    verbFun(sprintf('\tDrift   = %.2f',norm(thisCP.drift)));
```

```
if adjAccFlag
    % if we were adjusting the acceptance rate
    if abs(thisCP.accRate - optimalAccRate) < goodAccDiff
        % if it is good enough, continue running
        adjAccFlag = false;
        thisTrialN = longRun;
    else
        % else resubmit the chain with adjusted Amp
        thisAmp = max(minAmp,...
            thisAmp*sqrt(thisCP.accRate/optimalAccRate));
        thisTrialN = shortRun;
        chain.Loc.clear();
        chain.Stay.clear();
        chain.Score.clear();
        chain.Loc.push(thisCP.bestLoc);
        chain.Stay.push(0);
        chain.Score.push(thisCP.bestScore);
    end
else
    % if it were a long run
    if norm(thisCP.drift) < goodDrift
        % if it is also stable
        goodRun = goodRun + 1;
        verbFun(sprintf('\nPossible covergence [%d]',goodRun));
        verbFun(sprintf('Current location: %s',...
            num2str(thisCP.bestLoc)));

        if goodRun > 5
            break;
        end

        chain.Loc.clear();
        chain.Loc.push(thisCP.bestLoc);
        chain.Stay.clear();
        chain.Stay.push(0);
        chain.Score.clear();
        chain.Score.push(thisCP.bestScore);

        thisCov = thisCP.covmat;
        adjAccFlag = true;
        thisTrialN = shortRun;
```

```
            else
                % if it has not converged
                goodRun = 0;

                chain.Loc.clear();
                chain.Loc.push(thisCP.bestLoc);
                chain.Stay.clear();
                chain.Stay.push(0);
                chain.Score.clear();
                chain.Score.push(thisCP.bestScore);

                thisCov = thisCP.covmat;
                adjAccFlag = true;
                thisTrialN = shortRun;
            end
        end

    thisRun = thisRun + 1;

    end

    end
```

Program E.2: An illustration of the Automated Optimizer described in § E.3 using Matlab.

BIBLIOGRAPHY

K. Abazajian, Z. Zheng, I. Zehavi, D. H. Weinberg, J. A. Frieman, A. A. Berlind, M. R. Blanton, N. A. Bahcall, J. Brinkmann, D. P. Schneider, and M. Tegmark. Cosmology and the Halo Occupation Distribution from Small-Scale Galaxy Clustering in the Sloan Digital Sky Survey. *ApJ*, 625:613–620, June 2005. doi: 10.1086/429685.

K. N. Abazajian, J. K. Adelman-McCarthy, M. A. Agüeros, S. S. Allam, C. Allende Prieto, D. An, K. S. J. Anderson, S. F. Anderson, J. Annis, N. A. Bahcall, and et al. The Seventh Data Release of the Sloan Digital Sky Survey. *ApJS*, 182:543, June 2009a. doi: 10.1088/0067-0049/182/2/543.

K. N. Abazajian, J. K. Adelman-McCarthy, M. A. Agüeros, S. S. Allam, C. Allende Prieto, D. An, K. S. J. Anderson, S. F. Anderson, J. Annis, N. A. Bahcall, and et al. The Seventh Data Release of the Sloan Digital Sky Survey. *ApJS*, 182:543, June 2009b. doi: 10.1088/0067-0049/182/2/543.

G. O. Abell. The Distribution of Rich Clusters of Galaxies. *ApJS*, 3:211, May 1958. doi: 10.1086/190036.

C. Adami, F. Durret, C. Benoist, J. Coupon, A. Mazure, B. Meneux, O. Ilbert, J. Blaizot, S. Arnouts, A. Cappi, B. Garilli, L. Guennou, V. Lebrun, O. Lefèvre, S. Maurogordato, H. J. McCracken, Y. Mellier, E. Slezak, L. Tresse, and M. P. Ulmer. Galaxy structure searches by photometric redshifts in the CFHTLS. *A&A*, 509:A81, Jan. 2010. doi: 10.1051/0004-6361/200913067.

J. K. Adelman-McCarthy, M. A. Agüeros, S. S. Allam, C. Allende Prieto, K. S. J. Anderson, S. F. Anderson, J. Annis, N. A. Bahcall, C. A. L. Bailer-Jones, I. K. Baldry, J. C. Barentine, B. A. Bassett, A. C. Becker, T. C. Beers, E. F. Bell, A. A. Berlind, M. Bernardi, M. R. Blanton, J. J. Bochanski, W. N. Boroski, J. Brinchmann, J. Brinkmann, R. J. Brunner, T. Budavári, S. Carliles, M. A. Carr, F. J. Castander, D. Cinabro, R. J. Cool, K. R. Covey, I. Csabai, C. E. Cunha, J. R. A. Davenport, B. Dilday, M. Doi, D. J. Eisenstein, M. L. Evans, X. Fan, D. P. Finkbeiner, S. D. Friedman, J. A. Frieman, M. Fukugita, B. T. Gänsicke, E. Gates, B. Gillespie, K. Glazebrook, J. Gray, E. K. Grebel, J. E. Gunn, V. K. Gurbani, P. B. Hall, P. Harding, M. Harvanek, S. L. Hawley, J. Hayes, T. M. Heckman, J. S. Hendry, R. B. Hindsley, C. M. Hirata, C. J. Hogan, D. W. Hogg, J. B. Hyde, S.-i. Ichikawa, Ž. Ivezić, S. Jester, J. A. Johnson, A. M. Jorgensen, M. Jurić, S. M. Kent, R. Kessler, S. J. Kleinman, G. R. Knapp, R. G. Kron, J. Krzesinski, N. Kuropatkin, D. Q. Lamb, H. Lampeitl, S. Lebedeva, Y. S. Lee, R. F.

Leger, S. Lépine, M. Lima, H. Lin, D. C. Long, C. P. Loomis, J. Loveday, R. H. Lupton, O. Malanushenko, V. Malanushenko, R. Mandelbaum, B. Margon, J. P. Marriner, D. Martínez-Delgado, T. Matsubara, P. M. McGehee, T. A. McKay, A. Meiksin, H. L. Morrison, J. A. Munn, R. Nakajima, E. H. Neilsen, Jr., H. J. Newberg, R. C. Nichol, T. Nicinski, M. Nieto-Santisteban, A. Nitta, S. Okamura, R. Owen, H. Oyaizu, N. Padmanabhan, K. Pan, C. Park, J. Peoples, Jr., J. R. Pier, A. C. Pope, N. Purger, M. J. Raddick, P. Re Fiorentin, G. T. Richards, M. W. Richmond, A. G. Riess, H.-W. Rix, C. M. Rockosi, M. Sako, D. J. Schlegel, D. P. Schneider, M. R. Schreiber, A. D. Schwope, U. Seljak, B. Sesar, E. Sheldon, K. Shimasaku, T. Sivarani, J. A. Smith, S. A. Snedden, M. Steinmetz, M. A. Strauss, M. SubbaRao, Y. Suto, A. S. Szalay, I. Szapudi, P. Szkody, M. Tegmark, A. R. Thakar, C. A. Tremonti, D. L. Tucker, A. Uomoto, D. E. Vanden Berk, J. Vandenberg, S. Vidrih, M. S. Vogeley, W. Voges, N. P. Vogt, Y. Wadadekar, D. H. Weinberg, A. A. West, S. D. M. White, B. C. Wilhite, B. Yanny, D. R. Yocum, D. G. York, I. Zehavi, and D. B. Zucker. The Sixth Data Release of the Sloan Digital Sky Survey. *ApJS*, 175:297–313, Apr. 2008. doi: 10.1086/524984.

C. P. Ahn, R. Alexandroff, C. Allende Prieto, S. F. Anderson, T. Anderton, B. H. Andrews, É. Aubourg, S. Bailey, E. Balbinot, R. Barnes, and et al. The Ninth Data Release of the Sloan Digital Sky Survey: First Spectroscopic Data from the SDSS-III Baryon Oscillation Spectroscopic Survey. *ApJS*, 203:21, Dec. 2012. doi: 10.1088/0067-0049/203/2/21.

S. W. Allen, D. A. Rapetti, R. W. Schmidt, H. Ebeling, R. G. Morris, and A. C. Fabian. Improved constraints on dark energy from Chandra X-ray observations of the largest relaxed galaxy clusters. *MNRAS*, 383:879–896, Jan. 2008. doi: 10.1111/j.1365-2966.2007.12610.x.

R. E. Angulo, V. Springel, S. D. M. White, A. Jenkins, C. M. Baugh, and C. S. Frenk. Scaling relations for galaxy clusters in the Millennium-XXL simulation. *MNRAS*, 426:2046–2062, Nov. 2012. doi: 10.1111/j.1365-2966.2012.21830.x.

J. Annis, S. Bridle, F. J. Castander, A. E. Evrard, P. Fosalba, J. A. Frieman, E. Gaztanaga, B. Jain, A. V. Kravtsov, O. Lahav, H. Lin, J. Mohr, A. Stebbins, T. P. Walker, R. H. Wechsler, D. H. Weinberg, and J. Weller. Constraining Dark Energy with the Dark Energy Survey: Theoretical Challenges. *ArXiv Astrophysics e-prints*, Oct. 2005.

M. Arnaud and A. E. Evrard. The L_X-T relation and intracluster gas fractions of X-ray clusters. *MNRAS*, 305:631–640, May 1999. doi: 10.1046/j.1365-8711.1999.02442.x.

D. W. Atlee, P. Martini, R. J. Assef, D. D. Kelson, and J. S. Mulchaey. A Multi-wavelength Study of Low-Redshift Clusters of Galaxies. I. Comparison of X-ray and Mid-infrared Selected Active Galactic Nuclei. *ApJ*, 729:22, Mar. 2011. doi: 10.1088/0004-637X/729/1/22.

J. M. Bardeen, P. J. Steinhardt, and M. S. Turner. Spontaneous creation of almost scale-free density perturbations in an inflationary universe. *Phys. Rev. D*, 28:679–693, Aug. 1983. doi: 10.1103/PhysRevD.28.679.

M. Bartelmann. Arcs from a universal dark-matter halo profile. *A&A*, 313:697–702, Sept. 1996.

J. G. Bartlett and J. Silk. The Sunyaev-Zel'dovich effect and cluster evolution. *ApJ*, 423: 12–18, Mar. 1994. doi: 10.1086/173785.

M. R. Becker, T. A. McKay, B. Koester, R. H. Wechsler, E. Rozo, A. Evrard, D. Johnston, E. Sheldon, J. Annis, E. Lau, R. Nichol, and C. Miller. The Mean and Scatter of the Velocity Dispersion-Optical Richness Relation for maxBCG Galaxy Clusters. *ApJ*, 669: 905–928, Nov. 2007. doi: 10.1086/521920.

S. Bhattacharya, S. Habib, K. Heitmann, and A. Vikhlinin. Dark Matter Halo Profiles of Massive Clusters: Theory versus Observations. *ApJ*, 766:32, Mar. 2013. doi: 10.1088/0004-637X/766/1/32.

A. Biviano, G. Murante, S. Borgani, A. Diaferio, K. Dolag, and M. Girardi. On the efficiency and reliability of cluster mass estimates based on member galaxies. *A&A*, 456: 23–36, Sept. 2006. doi: 10.1051/0004-6361:20064918.

G. R. Blumenthal, S. M. Faber, J. R. Primack, and M. J. Rees. Formation of galaxies and large-scale structure with cold dark matter. *Nature*, 311:517–525, Oct. 1984. doi: 10.1038/311517a0.

P. Bode, J. P. Ostriker, and A. Vikhlinin. Exploring the Energetics of Intracluster Gas with a Simple and Accurate Model. *ApJ*, 700:989–999, Aug. 2009. doi: 10.1088/0004-637X/700/2/989.

J. R. Bond and G. Efstathiou. Cosmic background radiation anisotropies in universes dominated by nonbaryonic dark matter. *ApJ*, 285:L45–L48, Oct. 1984. doi: 10.1086/184362.

R. G. Bower, P. Coles, C. S. Frenk, and S. D. M. White. Cooperative galaxy formation and large-scale structure. *ApJ*, 405:403–412, Mar. 1993. doi: 10.1086/172372.

M. J. I. Brown, Z. Zheng, M. White, A. Dey, B. T. Jannuzi, A. J. Benson, K. Brand, M. Brodwin, and D. J. Croton. Red Galaxy Growth and the Halo Occupation Distribution. *ApJ*, 682:937–963, Aug. 2008. doi: 10.1086/589538.

N. Cappelluti, P. Predehl, H. Böhringer, H. Brunner, M. Brusa, V. Burwitz, E. Churazov, K. Dennerl, A. Finoguenov, M. Freyberg, P. Friedrich, G. Hasinger, E. Kenziorra, I. Kreykenbohm, G. Lamer, N. Meidinger, M. Mühlegger, M. Pavlinsky, J. Robrade, A. Santangelo, J. Schmitt, A. Schwope, M. Steinmitz, L. Strüder, R. Sunyaev, and C. Tenzer. eROSITA on SRG. A X-ray all-sky survey mission. *Memorie della Societa Astronomica Italiana Supplementi*, 17:159, 2011.

J. E. Carlstrom, P. A. R. Ade, K. A. Aird, B. A. Benson, L. E. Bleem, S. Busetti, C. L. Chang, E. Chauvin, H.-M. Cho, T. M. Crawford, A. T. Crites, M. A. Dobbs, N. W. Halverson, S. Heimsath, W. L. Holzapfel, J. D. Hrubes, M. Joy, R. Keisler, T. M. Lanting, A. T. Lee, E. M. Leitch, J. Leong, W. Lu, M. Lueker, D. Luong-van, J. J. McMahon,

J. Mehl, S. S. Meyer, J. J. Mohr, T. E. Montroy, S. Padin, T. Plagge, C. Pryke, J. E. Ruhl, K. K. Schaffer, D. Schwan, E. Shirokoff, H. G. Spieler, Z. Staniszewski, A. A. Stark, C. Tucker, K. Vanderlinde, J. D. Vieira, and R. Williamson. The 10 Meter South Pole Telescope. *PASP*, 123:568–581, May 2011. doi: 10.1086/659879.

J. D. Cohn and M. White. Issues in joint SZ and optical cluster finding. *MNRAS*, 393: 393–405, Feb. 2009. doi: 10.1111/j.1365-2966.2008.14215.x.

J. D. Cohn, A. E. Evrard, M. White, D. Croton, and E. Ellingson. Red-sequence cluster finding in the Millennium Simulation. *MNRAS*, 382:1738–1750, Dec. 2007. doi: 10.1111/j.1365-2966.2007.12479.x.

G. D. Coleman, C.-C. Wu, and D. W. Weedman. Colors and magnitudes predicted for high redshift galaxies. *ApJS*, 43:393–416, July 1980. doi: 10.1086/190674.

A. Cooray and R. Sheth. Halo models of large scale structure. *Phys. Rep.*, 372:1–129, Dec. 2002. doi: 10.1016/S0370-1573(02)00276-4.

J. Coupon, M. Kilbinger, H. J. McCracken, O. Ilbert, S. Arnouts, Y. Mellier, U. Abbas, S. de la Torre, Y. Goranova, P. Hudelot, J.-P. Kneib, and O. Le Fèvre. Galaxy clustering in the CFHTLS-Wide: the changing relationship between galaxies and haloes since z ˜ 1.2⋆. *A&A*, 542:A5, June 2012. doi: 10.1051/0004-6361/201117625.

A. C. da Silva, D. Barbosa, A. R. Liddle, and P. A. Thomas. Hydrodynamical simulations of the Sunyaev-Zel'dovich effect. *MNRAS*, 317:37–44, Sept. 2000. doi: 10.1046/j.1365-8711.2000.03553.x.

X. Dai, J. N. Bregman, C. S. Kochanek, and E. Rasia. On the Baryon Fractions in Clusters and Groups of Galaxies. *ApJ*, 719:119–125, Aug. 2010. doi: 10.1088/0004-637X/719/1/119.

J. Dunkley, M. Bucher, P. G. Ferreira, K. Moodley, and C. Skordis. Fast and reliable Markov chain Monte Carlo technique for cosmological parameter estimation. *MNRAS*, 356:925–936, Jan. 2005. doi: 10.1111/j.1365-2966.2004.08464.x.

P. R. M. Eisenhardt, M. Brodwin, A. H. Gonzalez, S. A. Stanford, D. Stern, P. Barmby, M. J. I. Brown, K. Dawson, A. Dey, M. Doi, A. Galametz, B. T. Jannuzi, C. S. Kochanek, J. Meyers, T. Morokuma, and L. A. Moustakas. Clusters of Galaxies in the First Half of the Universe from the IRAC Shallow Survey. *ApJ*, 684:905–932, Sept. 2008. doi: 10.1086/590105.

D. J. Eisenstein and W. Hu. Power Spectra for Cold Dark Matter and Its Variants. *ApJ*, 511:5–15, Jan. 1999. doi: 10.1086/306640.

D. J. Eisenstein, I. Zehavi, D. W. Hogg, R. Scoccimarro, M. R. Blanton, R. C. Nichol, R. Scranton, H.-J. Seo, M. Tegmark, Z. Zheng, S. F. Anderson, J. Annis, N. Bahcall, J. Brinkmann, S. Burles, F. J. Castander, A. Connolly, I. Csabai, M. Doi, M. Fukugita, J. A. Frieman, K. Glazebrook, J. E. Gunn, J. S. Hendry, G. Hennessy, Z. Ivezić, S. Kent,

G. R. Knapp, H. Lin, Y.-S. Loh, R. H. Lupton, B. Margon, T. A. McKay, A. Meiksin, J. A. Munn, A. Pope, M. W. Richmond, D. Schlegel, D. P. Schneider, K. Shimasaku, C. Stoughton, M. A. Strauss, M. SubbaRao, A. S. Szalay, I. Szapudi, D. L. Tucker, B. Yanny, and D. G. York. Detection of the Baryon Acoustic Peak in the Large-Scale Correlation Function of SDSS Luminous Red Galaxies. *ApJ*, 633:560–574, Nov. 2005. doi: 10.1086/466512.

V. R. Eke, C. M. Baugh, S. Cole, C. S. Frenk, P. Norberg, J. A. Peacock, I. K. Baldry, J. Bland-Hawthorn, T. Bridges, R. Cannon, M. Colless, C. Collins, W. Couch, G. Dalton, R. de Propris, S. P. Driver, G. Efstathiou, R. S. Ellis, K. Glazebrook, C. Jackson, O. Lahav, I. Lewis, S. Lumsden, S. Maddox, D. Madgwick, B. A. Peterson, W. Sutherland, and K. Taylor. Galaxy groups in the 2dFGRS: the group-finding algorithm and the 2PIGG catalogue. *MNRAS*, 348:866–878, Mar. 2004. doi: 10.1111/j.1365-2966.2004.07408.x.

B. M. S. Erickson, C. E. Cunha, and A. E. Evrard. Influence of projection in cluster cosmology studies. *Phys. Rev. D*, 84(10):103506, Nov. 2011. doi: 10.1103/PhysRevD.84.103506.

A. E. Evrard, T. J. MacFarland, H. M. P. Couchman, J. M. Colberg, N. Yoshida, S. D. M. White, A. Jenkins, C. S. Frenk, F. R. Pearce, J. A. Peacock, and P. A. Thomas. Galaxy Clusters in Hubble Volume Simulations: Cosmological Constraints from Sky Survey Populations. *ApJ*, 573:7–36, July 2002. doi: 10.1086/340551.

A. E. Evrard, J. Bialek, M. Busha, M. White, S. Habib, K. Heitmann, M. Warren, E. Rasia, G. Tormen, L. Moscardini, C. Power, A. R. Jenkins, L. Gao, C. S. Frenk, V. Springel, S. D. M. White, and J. Diemand. Virial Scaling of Massive Dark Matter Halos: Why Clusters Prefer a High Normalization Cosmology. *ApJ*, 672:122–137, Jan. 2008. doi: 10.1086/521616.

A. Finoguenov, L. Guzzo, G. Hasinger, N. Z. Scoville, H. Aussel, H. Böhringer, M. Brusa, P. Capak, N. Cappelluti, A. Comastri, S. Giodini, R. E. Griffiths, C. Impey, A. M. Koekemoer, J.-P. Kneib, A. Leauthaud, O. Le Fèvre, S. Lilly, V. Mainieri, R. Massey, H. J. McCracken, B. Mobasher, T. Murayama, J. A. Peacock, I. Sakelliou, E. Schinnerer, J. D. Silverman, V. Smolčić, Y. Taniguchi, L. Tasca, J. E. Taylor, J. R. Trump, and G. Zamorani. The XMM-Newton Wide-Field Survey in the COSMOS Field: Statistical Properties of Clusters of Galaxies. *ApJS*, 172:182–195, Sept. 2007. doi: 10.1086/516577.

W. Forman, E. Kellogg, H. Gursky, H. Tananbaum, and R. Giacconi. Observations of the Extended X-Ray Sources in the Perseus and Coma Clusters from UHURU. *ApJ*, 178: 309–316, Dec. 1972. doi: 10.1086/151791.

C. S. Frenk, S. D. M. White, G. Efstathiou, and M. Davis. Galaxy clusters and the amplitude of primordial fluctuations. *ApJ*, 351:10–21, Mar. 1990. doi: 10.1086/168439.

S. Giodini, D. Pierini, A. Finoguenov, G. W. Pratt, H. Boehringer, A. Leauthaud, L. Guzzo, H. Aussel, M. Bolzonella, P. Capak, M. Elvis, G. Hasinger, O. Ilbert, J. S. Kartaltepe, A. M. Koekemoer, S. J. Lilly, R. Massey, H. J. McCracken, J. Rhodes, M. Salvato, D. B.

Sanders, N. Z. Scoville, S. Sasaki, V. Smolcic, Y. Taniguchi, D. Thompson, and COSMOS Collaboration. Stellar and Total Baryon Mass Fractions in Groups and Clusters Since Redshift 1. *ApJ*, 703:982–993, Sept. 2009. doi: 10.1088/0004-637X/703/1/982.

M. D. Gladders and H. K. C. Yee. The Red-Sequence Cluster Survey. I. The Survey and Cluster Catalogs for Patches RCS 0926+37 and RCS 1327+29. *ApJS*, 157:1–29, Mar. 2005. doi: 10.1086/427327.

H. Guo, I. Zehavi, Z. Zheng, D. H. Weinberg, A. A. Berlind, M. Blanton, Y. Chen, D. J. Eisenstein, S. Ho, E. Kazin, M. Manera, C. Maraston, C. K. McBride, S. E. Nuza, N. Padmanabhan, J. K. Parejko, W. J. Percival, A. J. Ross, N. P. Ross, L. Samushia, A. G. Sánchez, D. J. Schlegel, D. P. Schneider, R. A. Skibba, M. E. C. Swanson, J. L. Tinker, R. Tojeiro, D. A. Wake, M. White, N. A. Bahcall, D. Bizyaev, H. Brewington, K. Bundy, L. N. A. da Costa, G. Ebelke, E. Malanushenko, V. Malanushenko, D. Oravetz, G. Rossi, A. Simmons, S. Snedden, A. Streblyanska, and D. Thomas. The Clustering of Galaxies in the SDSS-III Baryon Oscillation Spectroscopic Survey: Luminosity and Color Dependence and Redshift Evolution. *ApJ*, 767:122, Apr. 2013. doi: 10.1088/0004-637X/767/2/122.

A. H. Guth. Inflationary universe: A possible solution to the horizon and flatness problems. *Phys. Rev. D*, 23:347–356, Jan. 1981. doi: 10.1103/PhysRevD.23.347.

A. H. Guth and S.-Y. Pi. Fluctuations in the new inflationary universe. *Physical Review Letters*, 49:1110–1113, Oct. 1982. doi: 10.1103/PhysRevLett.49.1110.

E. J. Hallman, B. W. O'Shea, J. O. Burns, M. L. Norman, R. Harkness, and R. Wagner. The Santa Fe Light Cone Simulation Project. I. Confusion and the Warm-Hot Intergalactic Medium in Upcoming Sunyaev-Zel'dovich Effect Surveys. *ApJ*, 671:27–39, Dec. 2007. doi: 10.1086/522912.

E. J. Hallman, B. W. O'Shea, B. D. Smith, J. O. Burns, and M. L. Norman. The Santa Fe Light Cone Simulation Project. II. The Prospects for Direct Detection of the Whim with SZE Surveys. *ApJ*, 698:1795–1802, June 2009. doi: 10.1088/0004-637X/698/2/1795.

J. Hao, B. P. Koester, T. A. Mckay, E. S. Rykoff, E. Rozo, A. Evrard, J. Annis, M. Becker, M. Busha, D. Gerdes, D. E. Johnston, E. Sheldon, and R. H. Wechsler. Precision Measurements of the Cluster Red Sequence Using an Error-Corrected Gaussian Mixture Model. *ApJ*, 702:745–758, Sept. 2009. doi: 10.1088/0004-637X/702/1/745.

J. Hao, T. A. McKay, B. P. Koester, E. S. Rykoff, E. Rozo, J. Annis, R. H. Wechsler, A. Evrard, S. R. Siegel, M. Becker, M. Busha, D. Gerdes, D. E. Johnston, and E. Sheldon. A GMBCG Galaxy Cluster Catalog of 55,424 Rich Clusters from SDSS DR7. *ApJS*, 191: 254–274, Dec. 2010. doi: 10.1088/0067-0049/191/2/254.

E. R. Harrison. Fluctuations at the Threshold of Classical Cosmology. *Phys. Rev. D*, 1: 2726–2730, May 1970. doi: 10.1103/PhysRevD.1.2726.

Q. N. Hart, J. T. Stocke, A. E. Evrard, E. E. Ellingson, and W. A. Barkhouse. The Evolution of Radio Galaxies and X-Ray Point Sources in Coma Cluster Progenitors since z ˜ 1.2. *ApJ*, 740:59, Oct. 2011. doi: 10.1088/0004-637X/740/2/59.

G. Hasinger, N. Cappelluti, H. Brunner, M. Brusa, A. Comastri, M. Elvis, A. Finoguenov, F. Fiore, A. Franceschini, R. Gilli, R. E. Griffiths, I. Lehmann, V. Mainieri, G. Matt, I. Matute, T. Miyaji, S. Molendi, S. Paltani, D. B. Sanders, N. Scoville, L. Tresse, C. M. Urry, P. Vettolani, and G. Zamorani. The XMM-Newton Wide-Field Survey in the COSMOS Field. I. Survey Description. *ApJS*, 172:29–37, Sept. 2007. doi: 10.1086/516576.

W. Hastings. Monte Carlo sampling methods using Markov chains and their applications. *Biometrika*, 57:97–109, 1970. doi: 10.1093/biomet/57.1.97.

S. W. Hawking. The development of irregularities in a single bubble inflationary universe. *Physics Letters B*, 115:295–297, Sept. 1982. doi: 10.1016/0370-2693(82)90373-2.

E. Hubble. A Relation between Distance and Radial Velocity among Extra-Galactic Nebulae. *Proceedings of the National Academy of Science*, 15:168–173, Mar. 1929. doi: 10.1073/pnas.15.3.168.

A. Jenkins, C. S. Frenk, S. D. M. White, J. M. Colberg, S. Cole, A. E. Evrard, H. M. P. Couchman, and N. Yoshida. The mass function of dark matter haloes. *MNRAS*, 321: 372–384, Feb. 2001. doi: 10.1046/j.1365-8711.2001.04029.x.

D. E. Johnston, E. S. Sheldon, R. H. Wechsler, E. Rozo, B. P. Koester, J. A. Frieman, T. A. McKay, A. E. Evrard, M. R. Becker, and J. Annis. Cross-correlation Weak Lensing of SDSS galaxy Clusters II: Cluster Density Profiles and the Mass–Richness Relation. *ArXiv e-prints*, Sept. 2007.

S. T. Kay, M. W. Peel, C. J. Short, P. A. Thomas, O. E. Young, R. A. Battye, A. R. Liddle, and F. R. Pearce. Sunyaev-Zel'dovich clusters in Millennium gas simulations. *MNRAS*, 422:1999–2023, May 2012. doi: 10.1111/j.1365-2966.2012.20623.x.

B. P. Koester, T. A. McKay, J. Annis, R. H. Wechsler, A. Evrard, L. Bleem, M. Becker, D. Johnston, E. Sheldon, R. Nichol, C. Miller, R. Scranton, N. Bahcall, J. Barentine, H. Brewington, J. Brinkmann, M. Harvanek, S. Kleinman, J. Krzesinski, D. Long, A. Nitta, D. P. Schneider, S. Sneddin, W. Voges, and D. York. A MaxBCG Catalog of 13,823 Galaxy Clusters from the Sloan Digital Sky Survey. *ApJ*, 660:239–255, May 2007a. doi: 10.1086/509599.

B. P. Koester, T. A. McKay, J. Annis, R. H. Wechsler, A. E. Evrard, E. Rozo, L. Bleem, E. S. Sheldon, and D. Johnston. MaxBCG: A Red-Sequence Galaxy Cluster Finder. *ApJ*, 660:221–238, May 2007b. doi: 10.1086/512092.

A. Leauthaud, R. Massey, J.-P. Kneib, J. Rhodes, D. E. Johnston, P. Capak, C. Heymans, R. S. Ellis, A. M. Koekemoer, O. Le Fèvre, Y. Mellier, A. Réfrégier, A. C. Robin, N. Scoville, L. Tasca, J. E. Taylor, and L. Van Waerbeke. Weak Gravitational Lensing with COSMOS: Galaxy Selection and Shape Measurements. *ApJS*, 172:219–238, Sept. 2007. doi: 10.1086/516598.

A. Leauthaud, A. Finoguenov, J.-P. Kneib, J. E. Taylor, R. Massey, J. Rhodes, O. Ilbert, K. Bundy, J. Tinker, M. R. George, P. Capak, A. M. Koekemoer, D. E. Johnston, Y.-Y. Zhang, N. Cappelluti, R. S. Ellis, M. Elvis, S. Giodini, C. Heymans, O. Le Fèvre, S. Lilly, H. J. McCracken, Y. Mellier, A. Réfrégier, M. Salvato, N. Scoville, G. Smoot, M. Tanaka, L. Van Waerbeke, and M. Wolk. A Weak Lensing Study of X-ray Groups in the Cosmos Survey: Form and Evolution of the Mass-Luminosity Relation. *ApJ*, 709: 97–114, Jan. 2010. doi: 10.1088/0004-637X/709/1/97.

Y.-T. Lin and J. J. Mohr. K-band Properties of Galaxy Clusters and Groups: Brightest Cluster Galaxies and Intracluster Light. *ApJ*, 617:879–895, Dec. 2004. doi: 10.1086/425412.

Y.-S. Loh, E. Ellingson, H. K. C. Yee, D. G. Gilbank, M. D. Gladders, and L. F. Barrientos. The Color Bimodality in Galaxy Clusters since z ˜ 0.9. *ApJ*, 680:214–223, June 2008. doi: 10.1086/587830.

C.-J. Ma, B. R. McNamara, and P. E. J. Nulsen. Radio AGN in galaxy clusters: heating hot atmospheres and driving supermassive black hole growth over cosmic time. *ArXiv e-prints*, June 2012.

A. Mahdavi, H. Hoekstra, A. Babul, C. Bildfell, T. Jeltema, and J. P. Henry. Joint Analysis of Cluster Observations. II. Chandra/XMM-Newton X-Ray and Weak Lensing Scaling Relations for a Sample of 50 Rich Clusters of Galaxies. *ApJ*, 767:116, Apr. 2013. doi: 10.1088/0004-637X/767/2/116.

A. Mantz, S. W. Allen, H. Ebeling, D. Rapetti, and A. Drlica-Wagner. The observed growth of massive galaxy clusters - II. X-ray scaling relations. *MNRAS*, 406:1773–1795, Aug. 2010. doi: 10.1111/j.1365-2966.2010.16993.x.

P. Martini, G. R. Sivakoff, and J. S. Mulchaey. The Evolution of Active Galactic Nuclei in Clusters of Galaxies to Redshift 1.3. *ApJ*, 701:66–85, Aug. 2009. doi: 10.1088/0004-637X/701/1/66.

N. Mehrtens, A. K. Romer, M. Hilton, E. J. Lloyd-Davies, C. J. Miller, S. A. Stanford, M. Hosmer, B. Hoyle, C. A. Collins, A. R. Liddle, P. T. P. Viana, R. C. Nichol, J. P. Stott, E. N. Dubois, S. T. Kay, M. Sahlén, O. Young, C. J. Short, L. Christodoulou, W. A. Watson, M. Davidson, C. D. Harrison, L. Baruah, M. Smith, C. Burke, J. A. Mayers, P.-J. Deadman, P. J. Rooney, E. M. Edmondson, M. West, H. C. Campbell, A. C. Edge, R. G. Mann, K. Sabirli, D. Wake, C. Benoist, L. da Costa, M. A. G. Maia, and R. Ogando. The XMM Cluster Survey: optical analysis methodology and the first data release. *MNRAS*, 423:1024–1052, June 2012. doi: 10.1111/j.1365-2966.2012.20931.x.

M. Meneghetti, E. Rasia, J. Merten, F. Bellagamba, S. Ettori, P. Mazzotta, K. Dolag, and S. Marri. Weighing simulated galaxy clusters using lensing and X-ray. *A&A*, 514:A93, May 2010. doi: 10.1051/0004-6361/200913222.

N. Metropolis, A. W. Rosenbluth, M. N. Rosenbluth, A. H. Teller, and E. Teller. Equation of State Calculations by Fast Computing Machines. *J. Chem. Phys.*, 21:1087–1092, June 1953. doi: 10.1063/1.1699114.

D. M. Neumann and M. Arnaud. Regularity in the X-ray surface brightness profiles of galaxy clusters and the M-T relation. *A&A*, 348:711–727, Aug. 1999.

Y. Noh and J. D. Cohn. The geometry of the filamentary environment of galaxy clusters. *MNRAS*, 413:301–312, May 2011. doi: 10.1111/j.1365-2966.2010.18137.x.

Y. Noh and J. D. Cohn. Disentangling correlated scatter in cluster mass measurements. *MNRAS*, 426:1829–1844, Nov. 2012. doi: 10.1111/j.1365-2966.2012.21810.x.

H. Oyaizu, M. Lima, C. E. Cunha, H. Lin, J. Frieman, and E. S. Sheldon. A Galaxy Photometric Redshift Catalog for the Sloan Digital Sky Survey Data Release 6. *ApJ*, 674:768–783, Feb. 2008. doi: 10.1086/523666.

N. D. Padilla and D. G. Lambas. Anisotropies in the redshift-space correlations of galaxy groups and clusters - I. Simulated catalogues. *MNRAS*, 342:519–531, June 2003. doi: 10.1046/j.1365-8711.2003.06569.x.

P. J. E. Peebles and J. T. Yu. Primeval Adiabatic Perturbation in an Expanding Universe. *ApJ*, 162:815, Dec. 1970. doi: 10.1086/150713.

A. A. Penzias and R. W. Wilson. A Measurement of Excess Antenna Temperature at 4080 Mc/s. *ApJ*, 142:419–421, July 1965. doi: 10.1086/148307.

S. Perlmutter, G. Aldering, G. Goldhaber, R. A. Knop, P. Nugent, P. G. Castro, S. Deustua, S. Fabbro, A. Goobar, D. E. Groom, I. M. Hook, A. G. Kim, M. Y. Kim, J. C. Lee, N. J. Nunes, R. Pain, C. R. Pennypacker, R. Quimby, C. Lidman, R. S. Ellis, M. Irwin, R. G. McMahon, P. Ruiz-Lapuente, N. Walton, B. Schaefer, B. J. Boyle, A. V. Filippenko, T. Matheson, A. S. Fruchter, N. Panagia, H. J. M. Newberg, W. J. Couch, and Supernova Cosmology Project. Measurements of Omega and Lambda from 42 High-Redshift Supernovae. *ApJ*, 517:565–586, June 1999. doi: 10.1086/307221.

A. Pillepich, C. Porciani, and T. H. Reiprich. The X-ray cluster survey with eRosita: forecasts for cosmology, cluster physics and primordial non-Gaussianity. *MNRAS*, 422: 44–69, May 2012. doi: 10.1111/j.1365-2966.2012.20443.x.

Planck Collaboration, P. A. R. Ade, N. Aghanim, M. Arnaud, M. Ashdown, J. Aumont, C. Baccigalupi, M. Baker, A. Balbi, A. J. Banday, and et al. Planck early results. I. The Planck mission. *A&A*, 536:A1, Dec. 2011a. doi: 10.1051/0004-6361/201116464.

Planck Collaboration, P. A. R. Ade, N. Aghanim, M. Arnaud, M. Ashdown, J. Aumont, C. Baccigalupi, A. Balbi, A. J. Banday, R. B. Barreiro, and et al. Planck early results. VIII. The all-sky early Sunyaev-Zeldovich cluster sample. *A&A*, 536:A8, Dec. 2011b. doi: 10.1051/0004-6361/201116459.

Planck Collaboration, N. Aghanim, M. Arnaud, M. Ashdown, J. Aumont, C. Baccigalupi, A. Balbi, A. J. Banday, R. B. Barreiro, M. Bartelmann, J. G. Bartlett, E. Battaner, K. Benabed, A. Benoît, J.-P. Bernard, M. Bersanelli, R. Bhatia, J. J. Bock, A. Bonaldi, J. R. Bond, J. Borrill, F. R. Bouchet, M. L. Brown, M. Bucher, C. Burigana, P. Cabella, J.-F. Cardoso, A. Catalano, L. Cayón, A. Challinor, A. Chamballu, R.-R. Chary, L.-Y. Chiang, C. Chiang, G. Chon, P. R. Christensen, E. Churazov, D. L. Clements, S. Colafrancesco, S. Colombi, F. Couchot, A. Coulais, B. P. Crill, F. Cuttaia, A. da Silva, H. Dahle, L. Danese, P. de Bernardis, G. de Gasperis, A. de Rosa, G. de Zotti, J. Delabrouille, J.-M. Delouis, F.-X. Désert, J. M. Diego, K. Dolag, S. Donzelli, O. Doré, U. Dörl, M. Douspis, X. Dupac, G. Efstathiou, T. A. Enßlin, F. Finelli, I. Flores-Cacho, O. Forni, M. Frailis, E. Franceschi, S. Fromenteau, S. Galeotta, K. Ganga, R. T. Génova-Santos, M. Giard, G. Giardino, Y. Giraud-Héraud, J. González-Nuevo, K. M. Górski, S. Gratton, A. Gregorio, A. Gruppuso, D. Harrison, S. Henrot-Versillé, C. Hernández-Monteagudo, D. Herranz, S. R. Hildebrandt, E. Hivon, M. Hobson, W. A. Holmes, W. Hovest, R. J. Hoyland, K. M. Huffenberger, A. H. Jaffe, W. C. Jones, M. Juvela, E. Keihänen, R. Keskitalo, T. S. Kisner, R. Kneissl, L. Knox, H. Kurki-Suonio, G. Lagache, J.-M. Lamarre, A. Lasenby, R. J. Laureijs, C. R. Lawrence, S. Leach, R. Leonardi, M. Linden-Vørnle, M. López-Caniego, P. M. Lubin, J. F. Macías-Pérez, C. J. MacTavish, B. Maffei, D. Maino, N. Mandolesi, R. Mann, M. Maris, F. Marleau, E. Martínez-González, S. Masi, S. Matarrese, F. Matthai, P. Mazzotta, A. Melchiorri, J.-B. Melin, L. Mendes, A. Mennella, S. Mitra, M.-A. Miville-Deschênes, A. Moneti, L. Montier, G. Morgante, D. Mortlock, D. Munshi, A. Murphy, P. Naselsky, P. Natoli, C. B. Netterfield, H. U. Nørgaard-Nielsen, F. Noviello, D. Novikov, I. Novikov, S. Osborne, F. Pajot, F. Pasian, G. Patanchon, O. Perdereau, L. Perotto, F. Perrotta, F. Piacentini, M. Piat, E. Pierpaoli, R. Piffaretti, S. Plaszczynski, E. Pointecouteau, G. Polenta, N. Ponthieu, T. Poutanen, G. W. Pratt, G. Prézeau, S. Prunet, J.-L. Puget, R. Rebolo, M. Reinecke, C. Renault, S. Ricciardi, T. Riller, I. Ristorcelli, G. Rocha, C. Rosset, J. A. Rubiño-Martín, B. Rusholme, M. Sandri, D. Santos, B. M. Schaefer, D. Scott, M. D. Seiffert, G. F. Smoot, J.-L. Starck, F. Stivoli, V. Stolyarov, R. Sunyaev, J.-F. Sygnet, J. A. Tauber, L. Terenzi, L. Toffolatti, M. Tomasi, M. Tristram, J. Tuovinen, L. Valenziano, L. Vibert, P. Vielva, F. Villa, N. Vittorio, B. D. Wandelt, S. D. M. White, M. White, D. Yvon, A. Zacchei, and A. Zonca. Planck early results. X. Statistical analysis of Sunyaev-Zeldovich scaling relations for X-ray galaxy clusters. *A&A*, 536:A10, Dec. 2011c. doi: 10.1051/0004-6361/201116457.

Planck Collaboration, N. Aghanim, M. Arnaud, M. Ashdown, J. Aumont, C. Baccigalupi, A. Balbi, A. J. Banday, R. B. Barreiro, M. Bartelmann, and et al. Planck early results. XII. Cluster Sunyaev-Zeldovich optical scaling relations. *A&A*, 536:A12, Dec. 2011d. doi: 10.1051/0004-6361/201116489.

Planck Collaboration, N. Aghanim, M. Arnaud, M. Ashdown, F. Atrio-Barandela, J. Aumont, C. Baccigalupi, A. Balbi, A. J. Banday, R. B. Barreiro, J. G. Bartlett, E. Battaner, K. Benabed, J.-P. Bernard, M. Bersanelli, H. Böhringer, A. Bonaldi, J. R. Bond, J. Borrill, F. R. Bouchet, H. Bourdin, M. L. Brown, C. Burigana, R. C. Butler, P. Cabella, J.-F. Cardoso, P. Carvalho, A. Catalano, L. Cayón, A. Chamballu, R.-R. Chary, L.-Y.

Chiang, G. Chon, P. R. Christensen, D. L. Clements, S. Colafrancesco, S. Colombi, A. Coulais, B. P. Crill, F. Cuttaia, A. Da Silva, H. Dahle, R. J. Davis, P. de Bernardis, G. de Gasperis, G. de Zotti, J. Delabrouille, J. Démoclès, F.-X. Désert, J. M. Diego, K. Dolag, H. Dole, S. Donzelli, O. Doré, M. Douspis, X. Dupac, T. A. Enßlin, H. K. Eriksen, F. Finelli, I. Flores-Cacho, O. Forni, P. Fosalba, M. Frailis, S. Fromenteau, S. Galeotta, K. Ganga, R. T. Génova-Santos, M. Giard, J. González-Nuevo, R. González-Riestra, K. M. Górski, A. Gregorio, A. Gruppuso, F. K. Hansen, D. Harrison, A. Hempel, C. Hernández-Monteagudo, D. Herranz, S. R. Hildebrandt, A. Hornstrup, K. M. Huffenberger, G. Hurier, T. Jagemann, J. Jasche, M. Juvela, E. Keihänen, R. Keskitalo, T. S. Kisner, R. Kneissl, J. Knoche, L. Knox, H. Kurki-Suonio, G. Lagache, A. Lähteenmäki, J.-M. Lamarre, A. Lasenby, C. R. Lawrence, S. Leach, R. Leonardi, A. Liddle, P. B. Lilje, M. López-Caniego, G. Luzzi, J. F. Macías-Pérez, D. Maino, N. Mandolesi, R. Mann, F. Marleau, D. J. Marshall, E. Martínez-González, S. Masi, M. Massardi, S. Matarrese, F. Matthai, P. Mazzotta, P. R. Meinhold, A. Melchiorri, J.-B. Melin, L. Mendes, A. Mennella, M.-A. Miville-Deschênes, A. Moneti, L. Montier, G. Morgante, D. Mortlock, D. Munshi, P. Naselsky, P. Natoli, H. U. Nørgaard-Nielsen, F. Noviello, S. Osborne, F. Pasian, G. Patanchon, O. Perdereau, F. Perrotta, F. Piacentini, E. Pierpaoli, S. Plaszczynski, P. Platania, E. Pointecouteau, G. Polenta, N. Ponthieu, L. Popa, T. Poutanen, G. W. Pratt, J.-L. Puget, J. P. Rachen, R. Rebolo, M. Reinecke, M. Remazeilles, C. Renault, S. Ricciardi, T. Riller, I. Ristorcelli, G. Rocha, C. Rosset, M. Rossetti, J. A. Rubiño-Martín, B. Rusholme, M. Sandri, G. Savini, B. M. Schaefer, D. Scott, G. F. Smoot, J.-L. Starck, F. Stivoli, R. Sunyaev, D. Sutton, J.-F. Sygnet, J. A. Tauber, L. Terenzi, L. Toffolatti, M. Tomasi, M. Tristram, L. Valenziano, B. Van Tent, P. Vielva, F. Villa, N. Vittorio, B. D. Wandelt, J. Weller, S. D. M. White, D. Yvon, A. Zacchei, and A. Zonca. Planck intermediate results. I. Further validation of new Planck clusters with XMM-Newton. *A&A*, 543:A102, July 2012. doi: 10.1051/0004-6361/201118731.

W. H. Press and P. Schechter. Formation of Galaxies and Clusters of Galaxies by Self-Similar Gravitational Condensation. *ApJ*, 187:425–438, Feb. 1974. doi: 10.1086/152650.

A. G. Riess, A. V. Filippenko, P. Challis, A. Clocchiatti, A. Diercks, P. M. Garnavich, R. L. Gilliland, C. J. Hogan, S. Jha, R. P. Kirshner, B. Leibundgut, M. M. Phillips, D. Reiss, B. P. Schmidt, R. A. Schommer, R. C. Smith, J. Spyromilio, C. Stubbs, N. B. Suntzeff, and J. Tonry. Observational Evidence from Supernovae for an Accelerating Universe and a Cosmological Constant. *AJ*, 116:1009–1038, Sept. 1998. doi: 10.1086/300499.

E. Rozo, E. S. Rykoff, A. Evrard, M. Becker, T. McKay, R. H. Wechsler, B. P. Koester, J. Hao, S. Hansen, E. Sheldon, D. Johnston, J. Annis, and J. Frieman. Constraining the Scatter in the Mass-richness Relation of maxBCG Clusters with Weak Lensing and X-ray Data. *ApJ*, 699:768–781, July 2009. doi: 10.1088/0004-637X/699/1/768.

E. Rozo, A. E. Evrard, E. S. Rykoff, and J. G. Bartlett. A Comparative Study of Local Galaxy Clusters: II: X-ray and SZ Scaling Relations. *ArXiv e-prints*, Apr. 2012.

E. S. Rykoff, A. E. Evrard, T. A. McKay, M. R. Becker, D. E. Johnston, B. P. Koester, B. Nord, E. Rozo, E. S. Sheldon, R. Stanek, and R. H. Wechsler. The L_X-M relation of

clusters of galaxies. *MNRAS*, 387:L28–L32, June 2008. doi: 10.1111/j.1745-3933.2008.00476.x.

E. S. Rykoff, E. Rozo, M. T. Busha, C. E. Cunha, A. Finoguenov, A. Evrard, J. Hao, B. P. Koester, A. Leauthaud, B. Nord, M. Pierre, R. Reddick, T. Sadibekova, E. S. Sheldon, and R. H. Wechsler. redMaPPer I: Algorithm and SDSS DR8 Catalog. *ArXiv e-prints*, Mar. 2013.

R. K. Saito, M. Hempel, D. Minniti, P. W. Lucas, M. Rejkuba, I. Toledo, O. A. Gonzalez, J. Alonso-García, M. J. Irwin, E. Gonzalez-Solares, S. T. Hodgkin, J. R. Lewis, N. Cross, V. D. Ivanov, E. Kerins, J. P. Emerson, M. Soto, E. B. Amôres, S. Gurovich, I. Dékány, R. Angeloni, J. C. Beamin, M. Catelan, N. Padilla, M. Zoccali, P. Pietrukowicz, C. Moni Bidin, F. Mauro, D. Geisler, S. L. Folkes, S. E. Sale, J. Borissova, R. Kurtev, A. V. Ahumada, M. V. Alonso, A. Adamson, J. I. Arias, R. M. Bandyopadhyay, R. H. Barbá, B. Barbuy, G. L. Baume, L. R. Bedin, A. Bellini, R. Benjamin, E. Bica, C. Bonatto, L. Bronfman, G. Carraro, A. N. Chenè, J. J. Clariá, J. R. A. Clarke, C. Contreras, A. Corvillón, R. de Grijs, B. Dias, J. E. Drew, C. Fariña, C. Feinstein, E. Fernández-Lajús, R. C. Gamen, W. Gieren, B. Goldman, C. González-Fernández, R. J. J. Grand, G. Gunthardt, N. C. Hambly, M. M. Hanson, K. G. Hełminiak, M. G. Hoare, L. Huckvale, A. Jordán, K. Kinemuchi, A. Longmore, M. López-Corredoira, T. Maccarone, D. Majaess, E. L. Martín, N. Masetti, R. E. Mennickent, I. F. Mirabel, L. Monaco, L. Morelli, V. Motta, T. Palma, M. C. Parisi, Q. Parker, F. Peñaloza, G. Pietrzyński, G. Pignata, B. Popescu, M. A. Read, A. Rojas, A. Roman-Lopes, M. T. Ruiz, I. Saviane, M. R. Schreiber, A. C. Schröder, S. Sharma, M. D. Smith, L. Sodré, J. Stead, A. W. Stephens, M. Tamura, C. Tappert, M. A. Thompson, E. Valenti, L. Vanzi, N. A. Walton, W. Weidmann, and A. Zijlstra. VVV DR1: The first data release of the Milky Way bulge and southern plane from the near-infrared ESO public survey VISTA variables in the Vía Láctea. *A&A*, 537:A107, Jan. 2012. doi: 10.1051/0004-6361/201118407.

N. Sehgal, P. Bode, S. Das, C. Hernandez-Monteagudo, K. Huffenberger, Y.-T. Lin, J. P. Ostriker, and H. Trac. Simulations of the Microwave Sky. *ApJ*, 709:920–936, Feb. 2010. doi: 10.1088/0004-637X/709/2/920.

R. K. Sheth and G. Tormen. Large-scale bias and the peak background split. *MNRAS*, 308: 119–126, Sept. 1999. doi: 10.1046/j.1365-8711.1999.02692.x.

D. N. Spergel, L. Verde, H. V. Peiris, E. Komatsu, M. R. Nolta, C. L. Bennett, M. Halpern, G. Hinshaw, N. Jarosik, A. Kogut, M. Limon, S. S. Meyer, L. Page, G. S. Tucker, J. L. Weiland, E. Wollack, and E. L. Wright. First-Year Wilkinson Microwave Anisotropy Probe (WMAP) Observations: Determination of Cosmological Parameters. *ApJS*, 148: 175–194, Sept. 2003. doi: 10.1086/377226.

V. Springel, S. D. M. White, A. Jenkins, C. S. Frenk, N. Yoshida, L. Gao, J. Navarro, R. Thacker, D. Croton, J. Helly, J. A. Peacock, S. Cole, P. Thomas, H. Couchman, A. Evrard, J. Colberg, and F. Pearce. Simulations of the formation, evolution and clustering of galaxies and quasars. *Nature*, 435:629–636, June 2005. doi: 10.1038/nature03597.

R. Stanek, E. Rasia, A. E. Evrard, F. Pearce, and L. Gazzola. Massive Halos in Millennium Gas Simulations: Multivariate Scaling Relations. *ApJ*, 715:1508–1523, June 2010. doi: 10.1088/0004-637X/715/2/1508.

A. A. Starobinsky. Dynamics of phase transition in the new inflationary universe scenario and generation of perturbations. *Physics Letters B*, 117:175–178, Nov. 1982. doi: 10.1016/0370-2693(82)90541-X.

C. Stoughton, R. H. Lupton, M. Bernardi, M. R. Blanton, S. Burles, F. J. Castander, A. J. Connolly, D. J. Eisenstein, J. A. Frieman, G. S. Hennessy, R. B. Hindsley, Ž. Ivezić, S. Kent, P. Z. Kunszt, B. C. Lee, A. Meiksin, J. A. Munn, H. J. Newberg, R. C. Nichol, T. Nicinski, J. R. Pier, G. T. Richards, M. W. Richmond, D. J. Schlegel, J. A. Smith, M. A. Strauss, M. SubbaRao, A. S. Szalay, A. R. Thakar, D. L. Tucker, D. E. Vanden Berk, B. Yanny, J. K. Adelman, J. E. Anderson, Jr., S. F. Anderson, J. Annis, N. A. Bahcall, J. A. Bakken, M. Bartelmann, S. Bastian, A. Bauer, E. Berman, H. Böhringer, W. N. Boroski, S. Bracker, C. Briegel, J. W. Briggs, J. Brinkmann, R. Brunner, L. Carey, M. A. Carr, B. Chen, D. Christian, P. L. Colestock, J. H. Crocker, I. Csabai, P. C. Czarapata, J. Dalcanton, A. F. Davidsen, J. E. Davis, W. Dehnen, S. Dodelson, M. Doi, T. Dombeck, M. Donahue, N. Ellman, B. R. Elms, M. L. Evans, L. Eyer, X. Fan, G. R. Federwitz, S. Friedman, M. Fukugita, R. Gal, B. Gillespie, K. Glazebrook, J. Gray, E. K. Grebel, B. Greenawalt, G. Greene, J. E. Gunn, E. de Haas, Z. Haiman, M. Haldeman, P. B. Hall, M. Hamabe, B. Hansen, F. H. Harris, H. Harris, M. Harvanek, S. L. Hawley, J. J. E. Hayes, T. M. Heckman, A. Helmi, A. Henden, C. J. Hogan, D. W. Hogg, D. J. Holmgren, J. Holtzman, C.-H. Huang, C. Hull, S.-I. Ichikawa, T. Ichikawa, D. E. Johnston, G. Kauffmann, R. S. J. Kim, T. Kimball, E. Kinney, M. Klaene, S. J. Kleinman, A. Klypin, G. R. Knapp, J. Korienek, J. Krolik, R. G. Kron, J. Krzesiński, D. Q. Lamb, R. F. Leger, S. Limmongkol, C. Lindenmeyer, D. C. Long, C. Loomis, J. Loveday, B. MacKinnon, E. J. Mannery, P. M. Mantsch, B. Margon, P. McGehee, T. A. McKay, B. McLean, K. Menou, A. Merelli, H. J. Mo, D. G. Monet, O. Nakamura, V. K. Narayanan, T. Nash, E. H. Neilsen, Jr., P. R. Newman, A. Nitta, M. Odenkirchen, N. Okada, S. Okamura, J. P. Ostriker, R. Owen, A. G. Pauls, J. Peoples, R. S. Peterson, D. Petravick, A. Pope, R. Pordes, M. Postman, A. Prosapio, T. R. Quinn, R. Rechenmacher, C. H. Rivetta, H.-W. Rix, C. M. Rockosi, R. Rosner, K. Ruthmansdorfer, D. Sandford, D. P. Schneider, R. Scranton, M. Sekiguchi, G. Sergey, R. Sheth, K. Shimasaku, S. Smee, S. A. Snedden, A. Stebbins, C. Stubbs, I. Szapudi, P. Szkody, G. P. Szokoly, S. Tabachnik, Z. Tsvetanov, A. Uomoto, M. S. Vogeley, W. Voges, P. Waddell, R. Walterbos, S.-i. Wang, M. Watanabe, D. H. Weinberg, R. L. White, S. D. M. White, B. Wilhite, D. Wolfe, N. Yasuda, D. G. York, I. Zehavi, and W. Zheng. Sloan Digital Sky Survey: Early Data Release. *AJ*, 123:485–548, Jan. 2002. doi: 10.1086/324741.

R. A. Sunyaev and Y. B. Zeldovich. The Observations of Relic Radiation as a Test of the Nature of X-Ray Radiation from the Clusters of Galaxies. *Comments on Astrophysics and Space Physics*, 4:173, Nov. 1972.

The Dark Energy Survey Collaboration. The Dark Energy Survey. *ArXiv Astrophysics e-prints*, Oct. 2005.

J. Tinker, A. V. Kravtsov, A. Klypin, K. Abazajian, M. Warren, G. Yepes, S. Gottlöber, and D. E. Holz. Toward a Halo Mass Function for Precision Cosmology: The Limits of Universality. *ApJ*, 688:709–728, Dec. 2008. doi: 10.1086/591439.

J. L. Tinker, E. S. Sheldon, R. H. Wechsler, M. R. Becker, E. Rozo, Y. Zu, D. H. Weinberg, I. Zehavi, M. R. Blanton, M. T. Busha, and B. P. Koester. Cosmological Constraints from Galaxy Clustering and the Mass-to-number Ratio of Galaxy Clusters. *ApJ*, 745:16, Jan. 2012. doi: 10.1088/0004-637X/745/1/16.

C. Vale and M. White. Finding clusters in SZ surveys. *NewA*, 11:207–217, Jan. 2006. doi: 10.1016/j.newast.2005.07.005.

M. P. van Haarlem, C. S. Frenk, and S. D. M. White. Projection effects in cluster catalogues. *MNRAS*, 287:817–832, June 1997.

G. M. Voit, A. E. Evrard, and G. L. Bryan. Confusion of Diffuse Objects in the X-Ray Sky. *ApJ*, 548:L123–L126, Feb. 2001. doi: 10.1086/319102.

M. S. Warren, K. Abazajian, D. E. Holz, and L. Teodoro. Precision Determination of the Mass Function of Dark Matter Halos. *ApJ*, 646:881–885, Aug. 2006. doi: 10.1086/504962.

M. White, L. Hernquist, and V. Springel. Simulating the Sunyaev-Zeldovich Effect(s): Including Radiative Cooling and Energy Injection by Galactic Winds. *ApJ*, 579:16–22, Nov. 2002. doi: 10.1086/342756.

S. D. M. White and M. J. Rees. Core condensation in heavy halos - A two-stage theory for galaxy formation and clustering. *MNRAS*, 183:341–358, May 1978.

G. Wilson, A. Muzzin, H. K. C. Yee, M. Lacy, J. Surace, D. Gilbank, K. Blindert, H. Hoekstra, S. Majumdar, R. Demarco, J. P. Gardner, M. D. Gladders, and C. Lonsdale. Spectroscopic Confirmation of a Massive Red-Sequence-Selected Galaxy Cluster at z = 1.34 in the SpARCS-South Cluster Survey. *ApJ*, 698:1943–1950, June 2009. doi: 10.1088/0004-637X/698/2/1943.

R. Wojtak, E. L. Łokas, G. A. Mamon, S. Gottlöber, F. Prada, and M. Moles. Interloper treatment in dynamical modelling of galaxy clusters. *A&A*, 466:437–449, May 2007. doi: 10.1051/0004-6361:20066813.

R. Yan, M. White, and A. L. Coil. Mock Catalogs for the DEEP2 Redshift Survey. *ApJ*, 607:739–750, June 2004. doi: 10.1086/383588.

I. Zehavi, Z. Zheng, D. H. Weinberg, M. R. Blanton, N. A. Bahcall, A. A. Berlind, J. Brinkmann, J. A. Frieman, J. E. Gunn, R. H. Lupton, R. C. Nichol, W. J. Percival, D. P. Schneider, R. A. Skibba, M. A. Strauss, M. Tegmark, and D. G. York. Galaxy Clustering in the Completed SDSS Redshift Survey: The Dependence on Color and Luminosity. *ApJ*, 736:59, July 2011. doi: 10.1088/0004-637X/736/1/59.

Y. B. Zeldovich. A hypothesis, unifying the structure and the entropy of the Universe. *MNRAS*, 160:1P, 1972.

Z. Zheng, A. A. Berlind, D. H. Weinberg, A. J. Benson, C. M. Baugh, S. Cole, R. Davé, C. S. Frenk, N. Katz, and C. G. Lacey. Theoretical Models of the Halo Occupation Distribution: Separating Central and Satellite Galaxies. *ApJ*, 633:791–809, Nov. 2005. doi: 10.1086/466510.

Z. Zheng, A. L. Coil, and I. Zehavi. Galaxy Evolution from Halo Occupation Distribution Modeling of DEEP2 and SDSS Galaxy Clustering. *ApJ*, 667:760–779, Oct. 2007. doi: 10.1086/521074.

Z. Zheng, I. Zehavi, D. J. Eisenstein, D. H. Weinberg, and Y. P. Jing. Halo Occupation Distribution Modeling of Clustering of Luminous Red Galaxies. *ApJ*, 707:554–572, Dec. 2009. doi: 10.1088/0004-637X/707/1/554.

F. Zwicky. On the Masses of Nebulae and of Clusters of Nebulae. *ApJ*, 86:217, Oct. 1937. doi: 10.1086/143864.

F. Zwicky, E. Herzog, P. Wild, M. Karpowicz, and C. T. Kowal. *Catalogue of galaxies and of clusters of galaxies, Vol. I.* 1961.